POLISH ACADEMY OF SCIENCES
INSTITUTE OF PHYSICS

Established in 1920 by
the Polish Physical Society

ACTA PHYSICA POLONICA

- General Physics
- Atomic and Molecular Physics
- Condensed Matter
- Optics and Quantum Optics
- Quantum Information
- Biophysics
- Applied Physics

Proceedings of the Zakopane School of Physics 2023 International Symposium, Zakopane, Poland, May 23–27, 2023

RECOGNIZED BY THE EUROPEAN PHYSICAL SOCIETY

Volume 145 — Number 2, Warsaw, February 2024

PL ISSN 0587-4246 ATPLB6 145 (2) 81–154 (2024)

Address of the Publisher:
Instytut Fizyki PAN
al. Lotników 32/46
02-668 Warszawa, Poland
e-mail: appol@ifpan.edu.pl

Printed in Poland:
Drukarnia HAJSTRA Sp. z o.o.
M. Langiewicza 28
05-825 Grodzisk Mazowiecki
drukarnia-hajstra.com
e-mail: hajstra.biuro@gmail.com

POLISH ACADEMY OF SCIENCES
INSTITUTE OF PHYSICS

Established in 1920 by
the Polish Physical Society

ACTA PHYSICA POLONICA

- General Physics
- Atomic and Molecular Physics
- Condensed Matter
- Optics and Quantum Optics
- Quantum Information
- Biophysics
- Applied Physics

Proceedings of the Zakopane School of Physics 2023 International Symposium, Zakopane, Poland, May 23–27, 2023

RECOGNIZED BY THE EUROPEAN PHYSICAL SOCIETY

Volume 145 — Number 2, Warsaw, February 2024

PL ISSN 0587-4246 ATPLB6 145 (2) 81–154 (2024)

Proceedings of the Zakopane School of Physics 2023
International Symposium
Breaking Frontiers: Submicron Structures in Physics and Biology

Zakopane, Poland, May 23–27, 2023

Editors of the Proceedings:

Marta Wolny-Marszałek

Żaneta Świątkowska-Warkocka

Wojciech M. Kwiatek

WARSAW

POLISH ACADEMY OF SCIENCES
INSTITUTE OF PHYSICS

Organized by:

The Henryk Niewodniczański Institute of Nuclear Physics Polish Academy of Sciences (PAN)

International Advisory Board

Wojciech M. Kwiatek	*Institute of Nuclear Physics PAN*
Marta Wolny-Marszałek	*Institute of Nuclear Physics PAN*
Jacinto Sá	*Uppsala Universitet*
Wojciech Gawełda	*Universidad Autónoma de Madrid*
Eugenio Coronado	*Universidad de Valencia*
Ryszard Sobierajski	*Institute of Physics PAN*
Erik Cizmar	*Pavol Jozef Šafárik University in Košice*
Neven Barišić	*Institute of Solid State Physics, TU Wien*
Henryk Fiedorowicz	*Military University of Technology, Warsaw*

Local Committee

Magdalena Fitta *(chair)*	Monika Synowska-Kałuża *(secretary)*
Paweł Sobieszczyk	Żaneta Świątkowska-Warkocka
Marzena Mitura Nowak	Jędrzej Kobylarczyk
Rafał Fanselow	Wojciech Błachucki
Juliusz Chojenka	Gabriela Imbir

Partners

Preface

The Zakopane School of Physics "Breaking Frontiers: Submicron Structures in Physics and Biology" was held in Zakopane, Poland, from 23 to 27 of May 2023. This conference is a recurrent event of an international range, organized since the mid-1960s and encompassing a wide scope of scientific problems related not only to novel measurement techniques, but also to the application of nuclear physics methods in the study of biomedical materials and condensed phase.

The School is directed to early career scientists: students, Ph.D. students, and adjuncts at the threshold of the scientific career, who can present the results of their work or consult experienced mentors in a pleasant atmosphere. Among the 80 participants, 19 leading specialists in material science, physics, and biology enriched the event with their insightful lectures. The subject matter of this year's meeting included: the applications of novel X-ray techniques, multifunctional materials, magnetic nanostructures, molecular magnets, and the applications of physics in biology and medicine. Two special sessions were organized as part of the event: the first one devoted to measurement possibilities with the use of the X-ray laser in Hamburg (European XFEL), and the second one to the ELI (Extreme Light Infrastructure) research infrastructure.

In addition to the formal scientific program, the School allocated time for informal meetings and discussions, fostering collaboration and the birth of new ideas and friendships. As in previous meetings, valuable conversations and exchanges of opinions took place during scientific sessions, excursions, and shared meals and coffee breaks.

The success of the School was a collective effort. Special acknowledgment goes to the International Advisory Board for its significant input and constructive feedback. The Local Organizing Committee played a crucial role in preparing the conference, and I would like to thank you for your determination, commitment, and patience. Sincere thanks are also extended to all speakers and chairpersons for maintaining session schedules while encouraging lively debates. Gratitude is also expressed to the guest editors, authors, and referees for their dedicated efforts in ensuring that the proceedings accurately reflect the presented content. Special appreciation is reserved for Professor Jan Mostowski for his understanding, assistance, and support in preparing these proceedings.

The ongoing success of this symposia series fills me with optimism and eager anticipation for the forthcoming event in 2025. I hope that the Zakopane School of Physics 2023 has made a meaningful contribution to fostering relationships within the community engaged in interdisciplinary research, transcending the traditional boundaries of physics and biology.

Magdalena Fitta
Chair of the Conference

List of invited speakers

Siham Benhabib (Gif-sur-Yvette)	"Photo-induced phenomena in quantum materials"
Claudio Cirelli (Villigen)	"Ultrafast X-ray science at SwissFEL Alvra"
Péter Dombi (Budapest)	"Ultrasensitive optical probing of plasmonic hot electrons"
Alicia Forment-Aliaga (Valencia)	"Spin-crossover effect meets 2D materials and chirality"
Jakub Jurczyk (Zaragoza)	"3D nanolithography methods for novel spintronic devices"
Katarzyna Majzner (Kraków)	"Spectrophenotyping of leukemia cells — from Raman imaging to diagnosis"
Denys Makarov (Dresden)	"Curvilinear magnetism — from fundamentals to applications"
Ioanna Mantouvalou (Berlin)	"Transient NEXAFS spectroscopy using a laser-produced plasma soft X-ray source"
Mark W. Meisel (Gainesville)	"Materials in metastable forms — molecules to metals"
Christopher Milne (Schenefeld)	"Probing ultrafast structural and electronic dynamics in chemistry, biology and materials research using X-ray free electron lasers"
Michael Meyer (Schenefeld)	"Multi-photon processes and molecular dynamics in the soft X-ray regime: The small quantum systems (SQS) instrument at the European XFEL"
Beata Nowicka (Kraków)	"Thin films and nanocomposites of switchable coordination polymers"
Bohdan Padlyak (Zielona Góra)	"EPR spectroscopy of the radiation-induced centres in borate glasses"
Przemysław Piekarz (Kraków)	"Theoretical study of the demagnetization process in magnetic multilayers under ultrafast X-ray irradiation"
Dawid Pinkowicz (Kraków)	"Bringing molecular photomagnets to light — photochemical approach to molecular photomagnets"
Alessandro Surrente (Wrocław)	"Magnetically brightened dark excitons in two-dimensional metal halide perovskite nanoplatelets"
Cristian Svetina (Madrid)	"Extension of four wave-mixing methods at short wavelengths"
Jakub Szlachetko (Kraków)	"SOLARIS National Synchrotron Radiation Centre: The infrastructure for research and industry"
Wojciech Tabiś (Kraków)	"Exploring high magnetic field facilities: Advancements, challenges, and applications"

Proceedings of the Zakopane School of Physics 2023 International Symposium, Zakopane, Poland, May 23–27, 2023

Compact NEXAFS System Based on Laser–Plasma Soft X-ray Light Source for the Analysis of Barium Edges in a B+BaF_2 Optical Filter

T. Fok*, P. Wachulak, M. Wardzińska, A. Bartnik, P. Nyga, M.P. Nowak and H. Fiedorowicz

Institute of Optoelectronics, Military University of Technology, S. Kaliskiego 2, 00-908 Warsaw 49, Poland

Doi: 10.12693/APhysPolA.145.89 *e-mail: tomasz.fok@wat.edu.pl

In this work, we present the results of the analysis performed with near edge absorption fine structure spectroscopy of barium edges in a B+BaF_2 optical filter. The radiation was generated by a laser–plasma soft X-ray source based on a double-stream gas puff target. The use of a flat-field spectrometer based on a diffraction grating allowed us to collect the absorption spectra of the radiation transmitted by the analyzed optical filter. The results demonstrate the appearance of clear M-edges of barium (M4 and M5).

topics: near edge X-ray absorption fine structure (NEXAFS), soft X-rays, spectroscopy, barium

1. Introduction

The NEXAFS (near edge X-ray absorption fine structure) method was introduced more than 40 years ago by J. Stöhr [1] for the study of low-Z molecules absorbed by surfaces. Since then, this method has been widely used in many fields of science, for example in surface analysis in nanoscale samples [2, 3], thin organic films and liquids [4], and crystalline and amorphous inorganic materials [5].

Due to the high applicability of this measurement technique in the scientific world and the fact that it is mainly available on synchrotrons, a variety of compact solutions have been developed in the last few years, with a smaller number and range of photon energies [6–9] but still with a high and proven measurement potential.

In this paper, we present one of the potential applications of compact NEXAFS, i.e., the ability to detect barium (Ba) absorption edges (M-edges) using broadband plasma radiation from xenon and krypton. The analyzed material was a boron + barium fluoride (B+BaF_2) filter. The elements made of BaF_2 are widely used, for example, as optical windows, prisms, and lenses transmitting from ultraviolet to infrared [10], as scintillators to convert gamma radiation into detectable light [11, 12], to determine radiation quality in biology [13], and in microwave devices, especially at cryogenic temperatures due to its small losses at microwave frequencies [14]. Boron was used because it has a transmission window near ~ 6.6 nm, which was essential due to the filter's designated application. In this paper, barium M-edges are detected using a compact NEXAFS system.

2. Experimental setup

The measurements were performed on a setup previously presented in [15]. A significant modification was the change of the electromagnets, which resulted in different valve opening characteristics than in previous papers. As a result of this upgrade, the optimum gas pressures were reduced. The system shown in Fig. 1a had three sections: source section, sample section, and soft X-ray (SXR) spectrometer. The source section consisted of a laser–plasma source generating soft X-ray radiation (LPXS). The LPXS was driven by an Nd:YAG laser (model NL 303 HT, EKSPLA, Lithuania) with an energy of 0.6 J, pulse duration time of 3 ns, and a repetition rate of 10 Hz. The radiation was focused by a lens (diameter of 12.7 mm, a focal length f = 25 mm) to a spot of ~ 100 μm in diameter. A plasma was generated by the interaction of focused laser radiation with a double-stream Xe/He or Kr/He gas puff target [16, 17], which was formed by a collinear set of two nozzles driven by two electromagnetic valves. The inner nozzle is 0.8 mm in diameter and was pressurized by a high-Z gas, i.e., xenon and

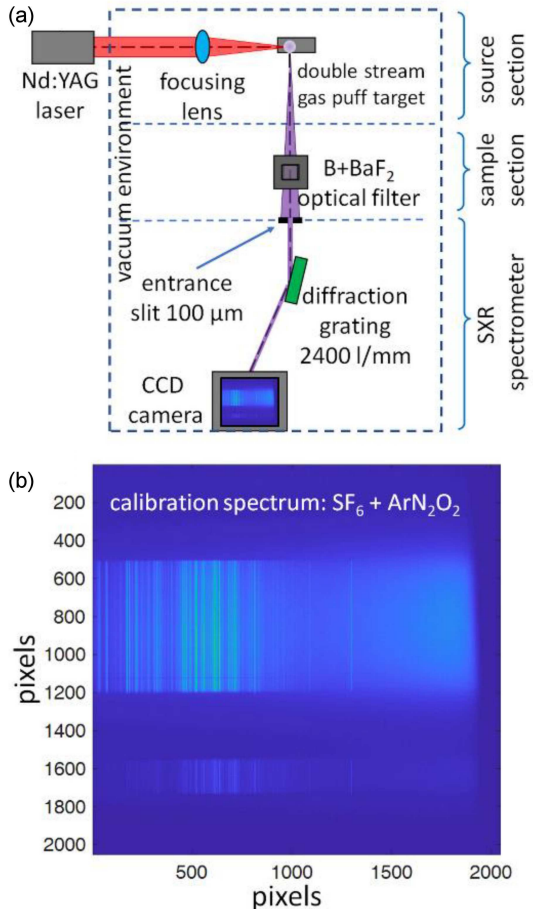

Fig. 1. (a) The NEXAFS experimental setup on which the spectrum of the radiation transmitted by the B+BaF_2 optical filter was measured and (b) the spectrum registered by the CDD camera — at the top is the reference spectrum, at the bottom is the sample spectrum.

krypton, to the optimal pressure of 8 bars, depending on the performed measurement. The outer nozzle was pressurized by a low-Z gas, i.e., helium, to 6.5 bars.

Further, the radiation was directed to the sample section, and after the interaction with the sample, part of the radiation was directed to the SXR spectrometer. The other part is later used as the reference signal. The SXR spectrometer with a similar configuration to the one described in [18] was used to produce and collect an absorption spectrum. The configuration was based on an entrance slit of 100 μm, a grazing incidence diffraction grating with a spatial frequency of 2400 l/mm (Hitachi), and a back-illuminated charge-coupled device (CCD) camera (GE 2048 2048 BI, greateyes, Germany). The camera had a chip with 2048×2048 pixels, with a pixel size of 13.5×13.5 μm^2. During the measurements, the chip was cooled to -20°C. A spectrometer with a comparable arrangement and a resolving power of $E/\Delta E =\sim 940$ was developed at the Institute of Optoelectronics [19].

The sample that was measured is an optical filter made of a 200 nm thick layer of boron and a 200 nm thick layer of barium fluoride deposited on top of the Si_3N_4 membrane with a thickness of 30 nm. Thin layers of barium fluoride and boron were deposited using an EB-PVD process (electron beam physical vapor deposition). This filter will be later used as a part of a source for photolithographic metrology near ~ 6.7 nm wavelength.

Before obtaining the optical density spectra, a proper spectrometer calibration was necessary. The calibration spectra captured for Ar:N_2:O_2 gas mixture and SF_6 injected into the laser–target interaction region, depicted in Fig. 1b, allowed us to perform the procedure of SXR spectrometer calibration by constructing the calibration curve to match the camera's pixels with the photon energy [20]. To construct the calibration curve, we used positions of the fluorine line $\lambda = 1.6807$ nm from F^{8+} ion, oxygen line $\lambda = 2.1602$ nm from O^{6+} ion, two very intensive SXR nitrogen lines $\lambda = 2.489$ nm and $\lambda = 2.878$ nm from N^{5+} ions, and argon lines $\lambda = 4.873$ nm and $\lambda = 4.918$ nm from Ar^{8+} ions.

3. Results

During the measurements, two series of data were acquired: the first series for gas puff target made of xenon and helium, and the second series using krypton and helium gas puff target. To verify whether the lines detected by the spectrometer were from the measured filter, two additional data series were performed using the Si_3N_4 membrane alone without deposited layers.

For each series of data consisting of 16 CCD images, the background signal was measured, and calibration spectra were captured. During the data post-processing, the background signal was subtracted from each image. In every series of data, values from 16 images were integrated in order to increase the signal-to-noise ratio (SNR). Further, data from 150 CCD lines were integrated both in the reference spectrum and sample spectrum, which can be seen in Fig. 2a for Xe and Fig. 2b for Kr gas, which additionally increased SNR. The final optical density spectrum OD(E) is computed with the use of

$$\mathrm{OD}(E) = -\ln\left[\frac{S_{\mathrm{sam}}(E)}{S_{\mathrm{ref}}(E)}\right], \tag{1}$$

where $S_{\mathrm{sam}}(E)$ and $S_{\mathrm{ref}}(E)$ are sample spectra and reference spectra, respectively. For a better visualization of the absorption edges, the obtained optical density spectrum is smoothed with a Golay–Savitzky (GS) filter (window = 3, frame length = 11) [21].

The spectra presented in Fig. 3a demonstrate two, M4 and M5, edges from barium obtained from measurement with Xe/He gas target. The edges look like peaks, due to the non-flat nature of the optical broad-band spectrum and the quite weak

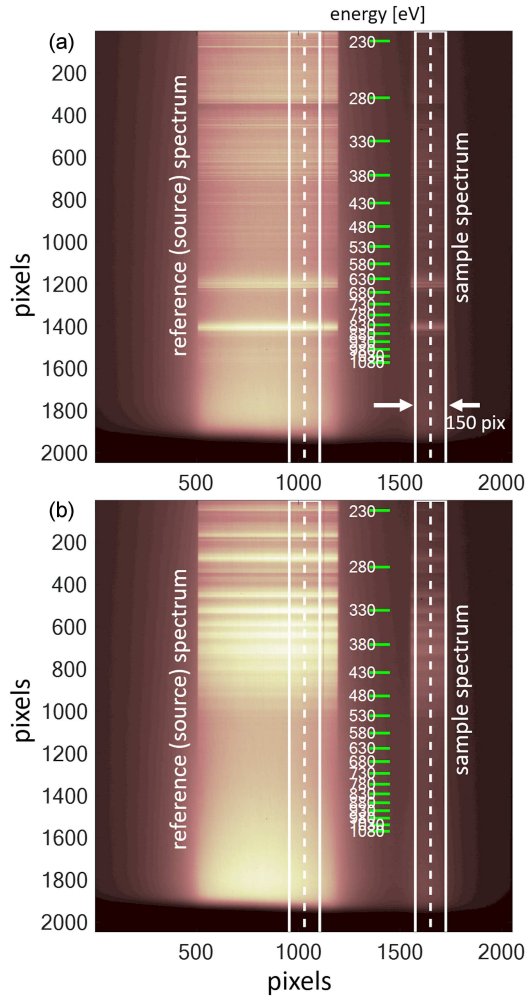

Fig. 2. Visualization of processing of images from the CCD camera taken for (a) xenon and (b) krypton as a working gas. Data from 150 CCD lines was integrated both for the reference and measured signals.

signal (the difference in OD signal of only 0.15 peak to valley). The M5 absorption edge occurs theoretically [22] at 780.5 eV, while the M4 edge can be found at 795.7 eV, while the measurements indicate slight energy offset, namely the M5 edge at 780.4 eV and M4 at 796.3 eV. The same edges are also visible for measurements performed with the Kr/He target (Fig. 3b), with a slight change in M5 edge energy equal to 780.5 eV — exactly as the database [22] predicts. The described values are compatible with the data from the Hephaestus database [22]. A group from Japan used mass spectrometry and X-ray absorption spectroscopy to study absorption edges in barium–oxide clusters. In their paper, they report M-edges from barium [23]. The other group confirmed the appearance of barium M-edges in $Ba_2Ca(BO_3)_2$ using X-ray excited optical luminescence (XEOL) spectroscopy [24]. These edges were also presented by a group from Switzerland [25]. They used X-ray

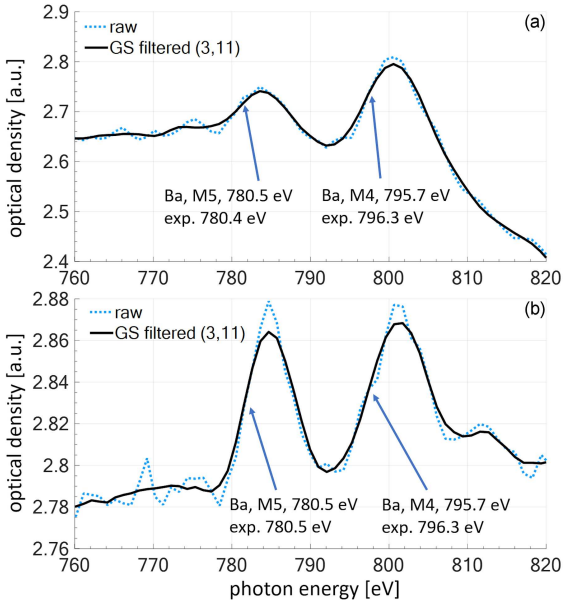

Fig. 3. Absorption spectra obtained from measurement with (a) Xe/He and (b) Kr/He target. The dotted blue lines illustrate the raw data from the SXR spectrometer. The black lines present data smoothed using the Golay–Savitzky algorithm based on [21] (window = 3 and frame length = 11).

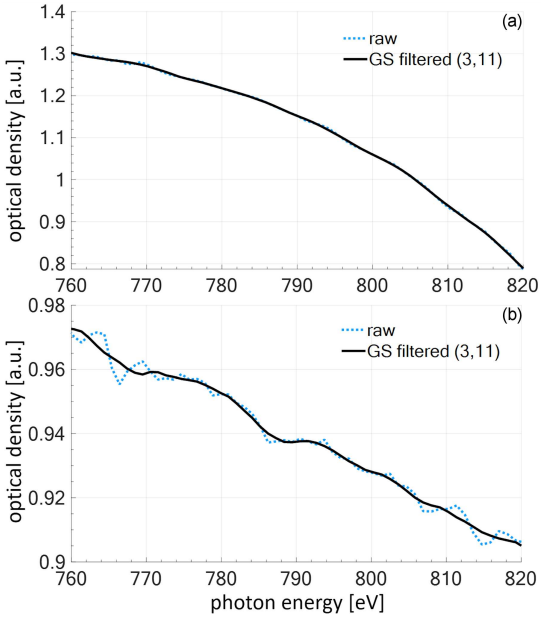

Fig. 4. Absorption spectrum obtained from measurement using the Si_3N_4 membrane without sputtered B+BaF_2 layers with (a) Xe/He and (b) Kr/He gas puff target.

absorption spectroscopy performed using the synchrotron radiation to investigate the spectra of $Ba_{1-x}Sr_xCo_{1-y}Fe_yO_{3-\delta}$ (x,y = 0.2–0.8) powders. According to our knowledge, we are the first group that used a compact NEXAFS system to detect barium M-edges in BaF_2.

We investigated whether detected edges are not just artifacts and whether they also occur for measurements done with pure Si_3N_4 membrane (without B and BaF_2 layers). We found no Ba edges, as depicted in Fig. 4a and b for the Xe and Kr illumination source spectrum, respectively.

4. Conclusions

In conclusion, the compact NEXAFS system was used to detect and measure the barium M-edges in the B+BaF_2 optical filter. The results indicate the M5 Ba absorption edge occurring at 780.5 eV, while the M4 edge is found at 796.3 eV for the Xe/He gas puff target and the Ba M5 edge at 780.4 eV for the Kr/He gas puff target. These edges were not visible for pure silicon nitride membranes. We expected to find fluorine K-edge as well, however, due to the nature of fluorine in the BaF_2 compound and the presence of the F–K edge in a spectral region with strong source spectral fluctuation, the signal was insufficient to clearly identify the fluorine K-edge. As for boron, its K-edge was out of the measuring range of the spectrometer.

Acknowledgments

The research was supported by the European Union's Horizon 2020 Programme (LASERLAB-EUROPE) Grant Agreement No. 871124, the National Science Center project No. 2020/39/I/ST7/03194, and the university grants UGB No. 18/IOE/2022 and UGB No. 23/IOE/2022.

References

[1] J. Stöhr, *NEXAFS spectroscopy*, Vol. 25, Springer, Berlin 2013.

[2] T. Hemraj-Benny, S. Banerjee, S. Sambasivan et al., *Small* **2**, 35 (2006).

[3] P. Guttmann, C. Bittencourt, S. Rehbein, P. Umek, X. Ke, G. Van Tendeloo, C.P. Ewels, G. Schneider, *Nat. Photon.* **6**, 25 (2012).

[4] G. Haehner, *ChemInform* **38** (2007).

[5] D. Li, G.M. Bancroft, M.E. Fleet, *J. Electron Spectrosc. Relat. Phenom.* **79**, 71 (1996).

[6] S.L. Cousin, F. Silva, S. Teichmann, M. Hemmer, B. Buades, J. Biegert, *Opt. Lett.* **39**, 5383 (2014).

[7] A. Jonas, K. Dammer, H. Stiel, B. Kangniesser, R. Sánchez-de-Armas, I. Mantouvalou, *Anal. Chem.* **92**, 15611 (2020).

[8] W. Błachucki, J. Czapla-Masztafiak, J. Sá, J. Szlachetko, *J. Anal. Atom. Spectrom.* **34**, 1409 (2019).

[9] J. Holburg, M. Müller, K. Mann, P. Wild, K. Eusterhues, J. Thieme, *Anal. Chem.* **94**, 3510 (2022).

[10] D. Hahn, *Opt. Photon.* **9**, 45 (2014).

[11] L. Moliner, G. Konstantinou, J. Maria Benlloch, P. Lecoq, in: *2021 IEEE Nuclear Science Symposium and Medical Imaging Conference (NSS/MIC), Piscataway (NJ)*, 2021, p. 1.

[12] M. Laval, *Nucl. Instrum. Methods Phys. Res.* **206**, 169 (1983).

[13] R.L. Dixon, F.C. Watts, *Phys. Med. Biol.* **17**, 81 (1972).

[14] M.V. Jacob, J.G. Hartnett, J. Mazierska, J. Krupka, M.E. Tobar, *Cryogenics* **46**, 730 (2006).

[15] T. Fok, P. Wachulak, K. Janulewicz, M. Duda, Ł. Węgrzyński, A. Bartnik, R. Jarocki, H. Fiedorowicz, *Acta Phys. Pol. A* **137**, 51 (2020).

[16] H. Fiedorowicz, A. Bartnik, R. Rakowski et al., *J. Phys. IV France* **11**, Pr2-409 (2001).

[17] A. Bartnik, H. Fiedorowicz, R. Jarocki, J. Kostecki, M. Szczurek, P.W. Wachulak, *Nucl. Instrum. Methods Phys. Res. A* **647**, 125 (2011).

[18] P. Wachulak, T. Fok, Ł. Węgrzyński, A. Bartnik, P. Nyga, K. Janulewicz, H. Fiedorowicz, *Opt. Express* **29**, 20514 (2021).

[19] P. Wachulak, M. Duda, A. Bartnik, A. Sarzyński, Ł. Węgrzyński, M. Nowak, A. Jancarek, H. Fiedorowicz, *Opt. Express* **26**, 8260 (2018).

[20] T. Fok, P. Wachulak, Ł. Węgrzyński et al., *Materials* **14**, 7337 (2021).

[21] J. Sedlmair, S.-C. Gleber, C. Peth, K. Mann, J. Niemeyer, J. Thieme, *J. Soils Sediments* **12**, 24 (2012).

[22] B. Ravel, M. Newville, *J. Synchrotron Rad.* **12**, 537 (2005).

[23] T. Hayakawa, M. Arakawa, K. Ando, Y. Kiyomura, T. Kawano, A. Terasaki, *J. Phys. Condens. Matter* **31**, 134003 (2019).

[24] J.Y.P. Ko, Y.-M. Yiu, H. Liang, T.K. Sham, *J. Chem. Phys.* **132**, 234701 (2010).

[25] A.S. Harvey, Z. Yang, A. Infortuna, D. Beckel, J.A. Purton, L.J. Gauckler, *J. Phys. Condens. Matter* **21**, 015801 (2008).

Proceedings of the Zakopane School of Physics 2023 International Symposium, Zakopane, Poland, May 23–27, 2023

Lattice Dynamics of Altermagnetic Ruthenium Oxide RuO_2

S. Basak* and A. Ptok

Institute of Nuclear Physics, Polish Academy of Sciences, W.E. Radzikowskiego 152, PL-31342 Kraków, Poland

Doi: 10.12693/APhysPolA.145.93 *e-mail: surajit.basak@ifj.edu.pl

Altermagnetic ruthenium oxide RuO_2 crystallizes with $P4_2/mnm$ symmetry. Here, we discuss the lattice dynamics of this structure. We show and discuss the phonon dispersion and density of states. The phonon dispersion curves contain several Dirac nodal lines and highly degenerate Dirac points. We present the characteristic frequencies and their irreducible representations at the Γ point. Theoretically obtained frequencies of the Raman active modes nicely reproduce the ones reported experimentally.

topics: lattice dynamics, altermagnetism, RuO_2, DFT

1. Introduction

The altermagnetic phase is a new elementary phase of magnetically ordered systems [1, 2]. This phase is characterized by the combined features of ferromagnetic (FM) and antiferromagnetic (AFM) phases, leading to novel effects. The altermagnetic phase breaks time-reversal symmetry similar to the FM phase and possesses compensated magnetization like the AFM phase. Unlike ferromagnets, however, the altermagnetic spin splitting in the non-relativistic bands is accompanied by a symmetry-protected zero net magnetization [3]. The spin-split part of the band structure is accompanied by spin degeneracies along certain surfaces in the Brillouin zone.

Presently, several compounds realizing the altermagnetic order are known (for more details, see [4]). In our paper, we discuss the dynamical properties of RuO_2 [5], crystallized with the rutile structure (see Fig. 1). The electronic band structure exhibits spin splitting in the range of 0.5 eV [6]. Such spin band splitting should be reflected in the spin-polarized angle-resolved photoelectron spectroscopy (ARPES) measurement [7]. The time- reversal symmetry breaking [8] and the anomalous Hall effect [9] were observed experimentally. Both phenomena are related to the topological properties associated with the nonzero Berry phase [10]. Finally, a thin film of RuO_2 exhibits superconducting properties [11].

Altermagnetic RuO_2 also has several properties, interesting from an application point of view, e.g., high activation barrier [12]. This compound is a prime catalyst for the oxygen evolution reaction in water splitting [13]. In the context of thermoelectric properties [14], the dynamical properties of RuO_2 can be interesting. Here, we present and discuss the dynamical properties of the altermagnetic RuO_2.

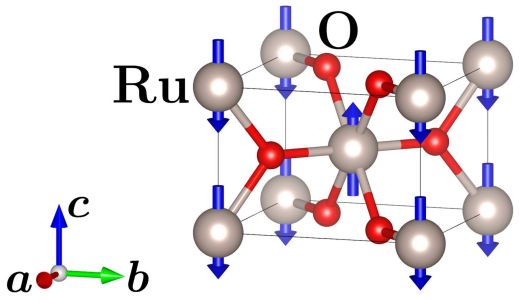

Fig. 1. The crystal structure of altermagnetic ruthenium oxide RuO_2.

The paper is organized as follows. The computational details are presented in Sect. 2. Next, in Sect. 3, we present and discuss our numerical results. Finally, a summary is provided in Sect. 4.

2. Computational details

The first-principles density functional theory (DFT) calculations were performed using the projector augmented-wave (PAW) potentials [15] implemented in the Vienna Ab initio Simulation Package (VASP) code [16–18]. For the exchange–correlation energy, the generalized gradient approximation (GGA) in the Perdew, Burke, and Ernzerhof (PBE) parametrization was used [19].

Similar to the previous study [7], we apply the correlation effects on Ru d-orbitals within the DFT+U approach introduced by Dudarev et al. [20]. The energy cutoff for the plane-wave expansion was set to 600 eV. Optimization of the structural parameters (in the presence of the spin–orbit coupling) was performed using a $10 \times 10 \times 15$ k-point grid using the Monkhorst–Pack scheme [21]. As a convergence condition of the optimization loop, we took the energy change below 10^{-6} eV and 10^{-8} eV for ionic and electronic degrees of freedom, respectively.

The dynamical properties were calculated using the direct Parlinski–Li–Kawazoe method [22] implemented in Phonopy [23]. The interatomic force constants were determined from the force acting on the atoms displaced from the equilibrium position. In these calculations, we used the supercell containing $2\times2\times3$ primitive unit cells, and reduced $4 \times 4 \times 4$ k-grid.

3. Results and discussion

3.1. Crystal structure

RuO_2 crystallizes with the rutile structure ($P4_2/mnm$, space group No. 136) presented in Fig. 1. It has one Ru atom sitting at each corner of a unit cell, as well as one Ru atom at the center. Each Ru atom is surrounded by six O atoms that form a distorted octahedron. In this case, the Ru and O atoms are located at Wyckoff positions 2b $(0,0,0)$ and 4g $(x_O, y_O, 0)$, respectively. Here, x_O and y_O are two free parameters describing the position of O atoms in the crystal structure. Theoretically, the obtained crystal parameters weakly depend on the assumed U [7], and in practice, U affects only the magnetic moment of Ru atoms. Similar to the previous study [24], we assume $U = 2$ eV for Ru d-orbitals. In this case, the magnetic moment of Ru is equal to 1.152 μ_B. After optimization, we find $a = 4.533$ Å, $c = 3.11$ Å, while the obtained free parameters are $x_O = 0.8037$ and $y_O = 0.1963$. The lattice constants are close to the experimentally observed ones, i.e., $a = 4.49$ Å, and $c = 3.11$ Å [25].

3.2. Phonon dispersion and density of states

The phonon dispersion curves are presented in Fig. 2 and are similar to the ones reported earlier [26]. The corresponding phonon density of states (DOS) is presented in Fig. 3. The vibrations in the low-frequency range (smaller than 7.5 THz) are mostly related to the Ru atoms. Similarly, higher frequency vibrations (above 14 THz) are mostly associated with vibrations of the lighter atoms, i.e., oxygen.Interestingly, vibration modes of oxygen

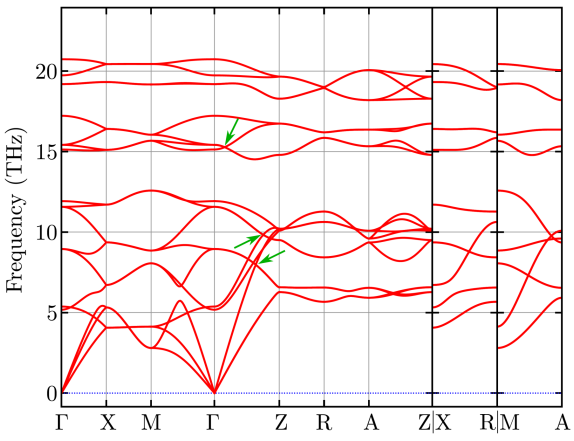

Fig. 2. The phonon dispersion curves of altermagnetic ruthenium oxide RuO_2. Green arrows mark the fourfold Dirac points along Γ–Z.

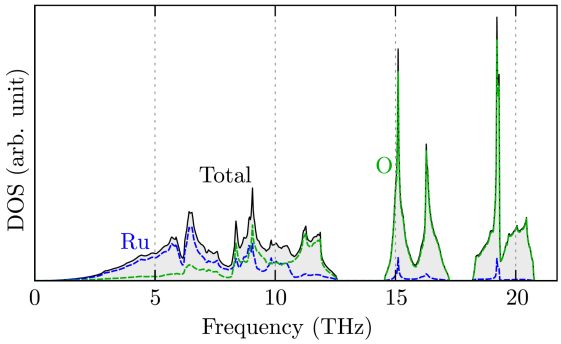

Fig. 3. The phonon density of states of altermagnetic ruthenium oxide RuO_2.

atoms at higher energies are separated from the rest of the modes by a gap. This frequency gap is well visible in the phonon band structure (Fig. 2).

In the phonon band structure, we can find several interesting features, well-known from the electronic band structure of RuO_2 [27] or non-magnetic IrO_2 with the same structure [28]. The doubly degenerate Dirac nodal lines (DNL) along the M–X path originate from the mirror symmetry along the (110) and $(\bar{1}10)$ planes. Similarly, mirror symmetry along the (001) plane leads to double degeneracy of bands for the R–A path. Additionally, nonsymmorphic symmetry, including a fourfold screw rotation around the z-axis C_{4z} and a glide mirror reflection along the (100) and (010) planes, also allows the realization of doubly degenerate DNL along Γ–Z and M–A.

The degeneracy of bands along Γ–Z is the same as their degeneracy at Γ point (see also Sect. 3.3). Along M–A, all the phonon bands are doubly degenerate. Additionally, along Γ–Z, highly degenerate Dirac points can be realized, coming from the crossing of single- or doubly degenerate bands. This leads to triple and fourfold degenerate Dirac points (a few fourfold degenerate Dirac points are indicated by green arrows in Fig. 2).

3.3. IR and Raman active modes

The phonon modes at the Γ point can be decomposed into irreducible representations of the space group $P4_2/mnm$ as follows

$$\Gamma_{\text{acoustic}} = A_{2\text{u}} + E_{\text{u}}, \tag{1}$$

$$\Gamma_{\text{optic}} = A_{1\text{g}} + A_{2\text{g}} + A_{2\text{u}} + B_{1\text{g}} + 2B_{1\text{u}} + B_{2\text{u}} + 3E_{\text{u}} + E_{\text{g}}. \tag{2}$$

In total, there are 18 vibrational modes, eight non-degenerate ($A_{1\text{g}}, A_{2\text{g}}, 2A_{2\text{u}}, B_{1\text{g}}, B_{2\text{g}}$, and $2B_{1\text{u}}$), and ten doubly degenerate (E_{g} and $4E_{\text{u}}$). Among these, $A_{2\text{u}}$ and E_{u} are infrared (IR) active, while $A_{1\text{g}}$, $B_{1\text{g}}$, $B_{2\text{g}}$, and E_{g} are Raman active. Raman active modes are related only to the oxygen atoms displacement. Contrary to this, IR active modes are related to the displacement of both Ru and O atoms.

Selection rules for Raman-active modes. The non-resonant Raman scattering intensity depends, in general, on the directions of the incident and scattered light relative to the principal axes of the crystal. It is expressed by Raman tensor R, relevant for a given crystal symmetry, as [29]

$$I \propto |\boldsymbol{e}_i \cdot R \cdot \boldsymbol{e}_s|^2, \tag{3}$$

where $\boldsymbol{e}_i$ and $\boldsymbol{e}_s$ are the polarization vectors of the incident and scattered light, respectively. According to group theory, the Raman tensor for the $P4_2/mnm$ space group takes the following forms for the Raman active modes

$$R(A_{1\text{g}}) = \begin{pmatrix} a & 0 & 0 \\ 0 & a & 0 \\ 0 & 0 & b \end{pmatrix},$$

$$R(B_{1\text{g}}) = \begin{pmatrix} c & 0 & 0 \\ 0 & -c & 0 \\ 0 & 0 & 0 \end{pmatrix}, \quad R(B_{2\text{g}}) = \begin{pmatrix} 0 & d & 0 \\ d & 0 & 0 \\ 0 & 0 & 0 \end{pmatrix},$$

$$R(E_{\text{g}}^{\text{I}}) = \begin{pmatrix} 0 & 0 & 0 \\ 0 & 0 & e \\ 0 & e & 0 \end{pmatrix}, \quad R(E_{\text{g}}^{\text{II}}) = \begin{pmatrix} 0 & 0 & -e \\ 0 & 0 & 0 \\ -e & 0 & 0 \end{pmatrix}. \tag{4}$$

Using relation (3) and the Raman tensors (4), we can determine the selection rules and Raman intensities for various scattering geometries. Table I summarizes the Raman response in the backscattering geometry for four polarization configurations. As we can see, it is possible to distinguish the Raman active modes using the different backscattering configurations. In this context, the observed Raman modes possess different insensitivity, as shown in Table I. Indeed, this technique was successfully experimentally used to recognize the Raman active modes [30, 31].

Theoretically obtained characteristic frequencies of the modes at Γ point and their irreducible representations for RuO_2 are collected in Table II. The frequencies of the Raman active modes at higher frequencies are underestimated with respect to the experimentally report ones [30]. Moreover, the "bulk" Raman active modes have the same frequencies as the ones reported for RuO_2 nanowires [31]. Finally, we should note that the observed frequencies can strongly depend on the experimental setup, e.g., "strain" [26, 30].

TABLE I

Selection rules for Raman-active modes.

Configuration	$A_{1\text{g}}$	$B_{1\text{g}}$	$B_{2\text{g}}$	E_{g}
e_x in e_x out (linear k)	$\lvert a\rvert^2$	$\lvert c\rvert^2$	0	0
e_x in e_y out (linear $\perp$)	0	0	$\lvert d\rvert^2$	0
e_x in e_z out (linear $\perp$)	0	0	0	$\lvert e\rvert^2$

TABLE II

Symmetries of irreducible representations and their characteristic frequencies at Γ point for RuO_2. The experimental frequencies of the Raman active modes correspond to the single-crystal measurements presented in [30].

Symm.	Freq. [THz]	Freq. [cm^{-1}]	Exp.[a] [cm^{-1}]
$B_{1\text{g}}$	5.180	172.79	–
$B_{1\text{u}}$	5.375	179.29	–
Eu	8.951	298.57	–
Eu	11.569	385.90	–
$A_{2\text{g}}$	11.924	397.74	–
$A_{2\text{u}}$	15.131	504.72	–
E_{g}	15.420	514.36	526
$B_{1\text{u}}$	17.225	574.57	–
Eu	19.193	640.22	–
$A_{1\text{g}}$	19.735	658.29	644
$B_{2\text{g}}$	20.736	691.68	714

[a] Frequencies only for Raman active modes

4. Conclusions

In this paper, we discussed the lattice dynamic of altermagnetic ruthenium oxide RuO_2. We show that the bulk system is stable with $P4_2/mnm$ symmetry. The phonon dispersion curves are well defined, i.e., all phonon branches possess real frequencies. The vibrations at the low-frequency range are related to the Ru modes, while the branches at the high-frequency range are mostly associated with the vibration of O atoms. We also discussed the characteristic frequencies of the modes at Γ point and the selective rules of Raman active modes. The Raman active mode is distinguished within backscattering geometry measurements. Theoretically obtained frequencies of the Raman active modes nicely reproduce the experimentally reported data.

Acknowledgments

Some figures in this work were rendered using Vesta [32]. We kindly acknowledge support from the National Science Centre (NCN, Poland) under Project No. 2021/43/B/ST3/02166.

References

[1] L. Smejkal, J. Sinova, T. Jungwirth, *Phys. Rev. X* **12**, 031042 (2022).

[2] L. Smejkal, J. Sinova, T. Jungwirth, *Phys. Rev. X* **12**, 040501 (2022).

[3] V. Gopalan, D.B. Litvin, *Nat. Mater.* **10**, 376 (2011).

[4] Y. Guo, H. Liu, O. Janson, I.C. Fulga, J. van den Brink, J.I. Facio, *Mater. Today Phys.* **32**, 100991 (2023).

[5] L. Šmejkal, R. González-Hernández, T. Jungwirth, J. Sinova, *Sci. Adv.* **6**, eaaz8809 (2020).

[6] J. Zhan, J. Li, W. Shi, X.-Q. Chen, Y. Sun, *Phys. Rev. B* **107**, 224402 (2023).

[7] A. Ptok, arXiv:2309.02421, 2023.

[8] O. Fedchenko, J. Minar, A. Akashdeep et al., arXiv:2306.02170, 2023.

[9] Z. Feng, X. Zhou, L. Šmejkal et al., *Nat. Electron.* **5**, 735 (2022).

[10] L. Šmejkal, A.H. MacDonald, J. Sinova, S. Nakatsuji, T. Jungwirth, *Nat. Rev. Mater.* **7**, 482 (2022).

[11] J.P. Ruf, H. Paik, N.J. Schreiber et al., *Nat. Commun.* **12**, 59 (2021).

[12] E. Torun, C.M. Fang, G.A. de Wijs, R.A. de Groot, *J. Phys. Chem. C* **117**, 6353 (2013).

[13] Q. Liang, A. Bieberle-Hütter, G. Brocks, *J. Phys. Chem. C* **126**, 1337 (2022).

[14] D. Music, O. Kremer, G. Pernot, J.M. Schneider, *Appl. Phys. Lett.* **106**, 063906 (2015).

[15] P.E. Blöchl, *Phys. Rev. B* **50**, 17953 (1994).

[16] G. Kresse, J. Hafner, *Phys. Rev. B* **49**, 14251 (1994).

[17] G. Kresse, J. Furthmüller, *Phys. Rev. B* **54**, 11169 (1996).

[18] G. Kresse, D. Joubert, *Phys. Rev. B* **59**, 1758 (1999).

[19] J.P. Perdew, K. Burke, M. Ernzerhof, *Phys. Rev. Lett.* **77**, 3865 (1996).

[20] S.L. Dudarev, G.A. Botton, S.Y. Savrasov, C.J. Humphreys, A.P. Sutton, *Phys. Rev. B* **57**, 1505 (1998).

[21] H.J. Monkhorst, J.D. Pack, *Phys. Rev. B* **13**, 5188 (1976).

[22] K. Parlinski, Z.Q. Li, Y. Kawazoe, *Phys. Rev. Lett.* **78**, 4063 (1997).

[23] A. Togo, I. Tanaka, *Scr. Mater.* **108**, 1 (2015).

[24] K.-H. Ahn, A. Hariki, K.-W. Lee, J. Kuneš, *Phys. Rev. B* **99**, 184432 (2019).

[25] Z.H. Zhu, J. Strempfer, R.R. Rao et al., *Phys. Rev. Lett.* **122**, 017202 (2019).

[26] M. Uchida, T. Nomoto, M. Musashi, R. Arita, M. Kawasaki, *Phys. Rev. Lett.* **125**, 147001 (2020).

[27] V. Jovic, R.J. Koch, S.K. Panda et al., *Phys. Rev. B* **98**, 241101(R) (2018).

[28] X. Xu, J. Jiang, W.J. Shi et al., *Phys. Rev. B* **99**, 195106 (2019).

[29] R. Loudon, *Adv. Phys.* **50**, 813 (2001).

[30] Y.M. Chen, A. Korotcov, H.P. Hsu, Y.S. Huang, D.S. Tsai, *New J. Phys.* **9**, 130 (2007).

[31] M.H. Kim, J.M. Baik, S.J. Lee, H.-Y. Shin, J. Lee, S. Yoon, G.D. Stucky, M. Moskovits, A.M. Wodtke, *Appl. Phys. Lett.* **96**, 213108 (2010).

[32] K. Momma, F. Izumi, *J. Appl. Crystallogr.* **44**, 1272 (2011).

Proceedings of the Zakopane School of Physics 2023 International Symposium, Zakopane, Poland, May 23–27, 2023

Consideration of the Potential of High Energy Resolution X-ray Absorption and X-ray Emission Experiments to Track Changes in Oxidation States on Nanoparticle Materials

A. Wach[a], G. Imbir[b], R. Fanselow[a], W. Błachucki[b] and J. Szlachetko[a]

[a] *SOLARIS National Synchrotron Radiation Centre, Jagiellonian University, Kraków, Poland*
[b] *Institute of Nuclear Physics, Polish Academy of Sciences, Kraków, Poland*

Doi: 10.12693/APhysPolA.145.97 *e-mail: jakub.szlachetko@uj.edu.pl

Precise control and characterization of nanomaterials at working conditions are essential for further rational applications in many areas important for modern society. Penetrating properties of X-ray radiation in combination with advanced spectroscopy schemes are an ideal tool to investigate modifications of nanomaterials with extraordinary precision. Here, we present preliminary results on the controlled oxidation of copper nanoparticles and exploration of X-ray absorption spectroscopy to follow electronic and structural changes. The described pilot experiment raises questions on the applicability of high energy resolution X-ray detection schemes in potential future investigations aimed at following reversible reduction/oxidation processes at nanoparticle surfaces.

topics: copper nanoparticles, X-ray absorption spectroscopy, X-ray emission spectroscopy, core–shell structures

1. Introduction

Nanomaterials prepared from earth-abundant and inexpensive metals have attracted considerable attention because of their potential as viable alternatives to rare and expensive noble metals. In this context, copper nanoparticles (NPs) have been studied extensively due to the broad range of potential applications in, e.g., sensing, solar cells, catalysis, photocatalysis, biomedicine, optics, and electronics [1]. Copper has a range of oxidation states (0, I, II, and III) due to the presence of unpaired electrons in their *d*-orbitals, making it very reactive and prone to undergo a variety of reactions. In particular, copper metal nanoparticles exhibit intense light absorption and scattering in the region of the solar spectrum due to the excitation of collective electronic excited states (plasmons) [2]. At visible wavelengths, the interaction of the incident light with conduction band electrons of nanoparticles resonantly excites coherent oscillations of the electron density of states. This phenomenon is called localized surface plasmon resonance (LSPR) and allows the generation of hot electron clouds that can be used as triggers for light-induced energy conversion and storage processes. The plasmonic properties, such as the resonant wavelength and the intensity of LSPR, are governed by the nature, size, and shape of plasmonic metals [3]. Obviously, the bottleneck for Cu NPs application is their stability, as they are prone to rapid oxidation, particularly at the relevant nanoparticle sizes (< 50 nm). From thermodynamic perspectives, both oxygen molecules and water are able to easily oxidize the surface of copper NPs under ambient conditions. According to recent studies, the oxidation mechanism in nanosized materials is not trivial and involves the formation of a core–shell structure (metal core and oxide shell) and internal voids attributed to the nano Kirkendall effect (NKE) [4]. It was shown that the oxidation process is governed by fast outward diffusion of Cu^+ ions through the oxide layer, which strongly depends on the degree of metal-to-oxide conversion. Many approaches have been tested to increase the stability and prevent the oxidation of copper NPs. Among them, surface modification via additional post-treatment (e.g., with capping ligands, photoreduction, chemical etching) has prevailed as the dominant strategy [5, 6]. Employed as an encapsulation material, a transparent matrix prevents oxidation processes, but changes the optical and electronic structure properties of nanoparticles, which excludes any systematic studies of the material with respect to potential applications.

Despite extensive studies on Cu NPs materials and their properties, a number of unanswered questions remain. In particular, there is a significant knowledge gap concerning the fundamental aspects, e.g., the effect of NPs surface oxide on the localized surface plasmon resonance strength and coupling of

the surface oxide with charge-accepting units, such as semiconductors and molecular linkers. Since the material's electronic structure links the optical absorption, electronic, and chemical properties of the material, the quantitative determination of the density of electronic states of NPs is necessary to correlate the high-efficiency light-absorption yield of NPs with the low efficiency of charge transfer processes.

In the present manuscript, we address materials methodology for plasmon-enhanced solar-driven chemistry, aiming to investigate the influence of copper surface states on the nanoparticles–molecular linker assembly capabilities. In the discussed proposal, we evaluate the exploration of X-ray penetrating capability and elemental sensitivity of the X-ray absorption spectroscopy (XAS) and X-ray emission spectroscopy (XES), further supported with high-energy experimental schemes. The combined approach exhibits the potential to map *in situ* the electronic structure around the Fermi level under controlled oxidation/reduction conditions in aqueous solution [5]. This provides the basis to determine Cu–oxide/Cu–metal compositions in the obtained CuOx@Cu core–shell type structures and deconvolute the contributions of bulk and surface states.

2. Experiment

The pilot experiments were performed at the PETRA III synchrotron P65 beamline. In short, X-rays delivered by 11 periods undulator were monochromatized with Si(111) monochromator crystals and sized down to 1000×500 μm. As a sample, the liquid Cu NPs (25 nm in diameter, purchased from Sigma-Aldrich) solution in distilled water with 1 mM concentration of Cu atoms was used. For the measurements, 30 mL of the sample solution was placed in the flat flow cell with Kapton windows, providing a 1 mm-thick liquid sheet at the X-ray beam spot. The flow was induced by a peristaltic pump connected to the cell through flow tubes. The total fluorescence XAS spectra were recorded by scanning the X-ray energy around the Cu K-edge, and the X-ray fluorescence spectra were recorded with a silicon drift detector (SDD). In order to mimic the surface/bulk oxidation change of NPs, a water solution of hydrogen peroxide (H_2O_2) was added in two steps into the liquid sample: first 5 mL of 1 mM, then 0.3 mL of 9.8 M (as-purchased concentration, Sigma Aldrich). Measurements of reference materials, i.e., Cu foil and CuO pellet (1 wt% in cellulose), were conducted in the transmission mode.

The X-ray absorption spectra are sensitive to the local atomic and electronic structures around the absorbing atom and thus can be used to verify the nature of copper species. The normalized copper K-edge spectra collected for Cu NPs and reference compounds are presented in Fig. 1. The reference Cu metal foil, CuO reference, bare Cu NPs, and oxidized Cu NPs are marked by black, blue, red, and green lines, respectively. The measured Cu foil and CuO spectra are equivalent to the spectra reported in the literature [7]. The spectral shape of Cu is dominated by the $1s$ to $4p$ excitation feature at the absorption edge (due to dipole-allowed transitions) and the following resonant structures resulting from the scattering of photoelectrons on surrounding atoms. The reference CuO spectrum is shifted toward higher energies and shows a very weak pre-edge structure at 8977 eV due to the $1s$ to $3d$ excitation and at-edge feature related to an unoccupied $4p$ orbital. The spectrum collected for bare Cu NPs already shows differences with respect to the one for Cu metallic foil. This effect may be explained by a partial oxidation of the NPs surface, as the apparent shift of the XAS data towards higher energy confirms a partial change in the oxidation state. As previously mentioned, the copper nanoparticles quickly oxidize to polycrystalline cuprous oxide (Cu_2O) under ambient conditions. After a controlled addition of an oxidant agent (H_2O_2), a clear change of the spectral features is observed, indicating the change of Cu NPs into the more oxidized form consisting of Cu(I) and Cu(II) species. This result is confirmed when comparing the *in situ* oxidized NPs with reference CuO powder. In order to determine the ratio of surface/bulk oxidation and form of the formed structures, future experiments are needed that will cover different concentrations of oxidants and sizes of metallic NPs. An important element of the research will be to address the possibility of reducing the so-oxidized samples and exploring the controlled *in situ* formation of Cu NPs in a fully metallic state. At this point, the mentioned experiments are beyond the scope of the present manuscript.

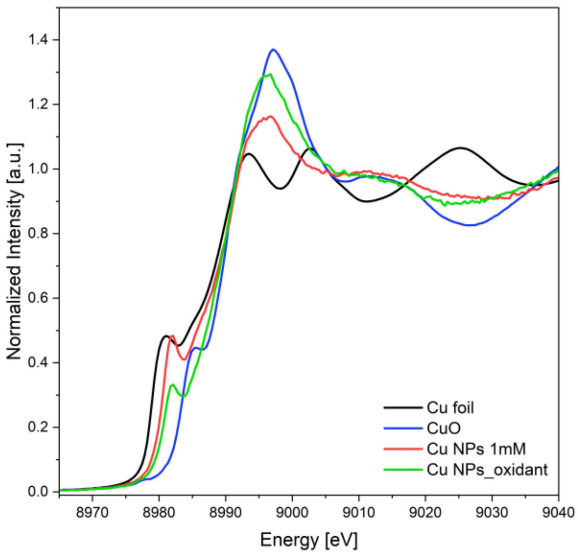

Fig. 1. Normalized copper K-edge XAS spectra for Cu foil, bare Cu NPs, Cu NPs after oxidation, and CuO reference.

3. Discussion

The obtained result provides very important information on the eventual feasibility of using X-ray absorption spectroscopy to monitor *in situ* changes in surface oxidation and reduction processes in a controlled manner. First of all, the detected spectral changes are significant and therefore allow for a very precise determination of the surface oxide-to-bulk metal ratio. From the obtained signal differences, we estimated that the detection of oxide-to-bulk contribution can be determined down to a 1% level. However, in order to address and evaluate structural changes caused by oxidization and reduction mechanisms, different NPs sizes should be subjected to future experiments.

An important aspect of *in situ* and *operando* experiments is the consideration of high-resolution Cu K-edge XAS experiments in the fluorescence mode instead of typical XAS measurements. The natural lifetime broadening at the K-edge of Cu amounts to 1.4 eV and is larger than the Darwin width broadening induced by monochromator crystals, which equals 1.26 eV. Therefore, the application of high energy resolution detection schemes, such as the use of von Hamos or Johann crystal spectrometers, will deliver significant improvement to the experimental resolution. This is of importance, especially for direct $1s$ to $3d$ excitation in CuO that is visible in XAS spectra as a weak pre-edge structure and is mostly hindered by natural lifetime broadening of the core–hole. For this reason, the detailed analysis of this spectral feature is challenging and often involves dedicated fitting procedures. We should emphasize that the improvement in spectral resolution does not only relate directly to the width values of lifetime broadening and experimental broadening, but also refers to the type of spectral function describing the discussed contributions. This effect is rarely discussed in the literature, but is worth mentioning because the lifetime broadening is determined by the Lorentz distribution, while the experimental contribution is given by the Gaussian function. Due to the fact that the Lorentz function decays as 1/energy and the Gaussian contribution as $1/\text{energy}^2$, the latter is vanishing much faster, making the broadening of spectra features less extended in the energy. As a consequence, even if both widths of broadening are equal, the quality of experimental data convolved with the Gaussian distribution exhibits better resolution than for the Lorentz one. This observation has been confirmed in a range of experiments where the introduction of high energy resolution schemes for detection delivered higher spectral quality even for small differences between core–hole and instrumental contributions [8, 9]. At this point, the discussed effect still should be validated experimentally. However, it should be emphasized that a systematic study of such properties is not possible because the values of natural lifetime or experimental broadening cannot be set in a controlled manner and are delivered as discrete values during experiments.

Another important aspect of considering high energy resolution schemes in XAS experiments is the possibility of simultaneous detection of XES spectra when recording XAS data. This is an important aspect as XES is complementary to XAS and supplements the absorption data with information on the occupied electronic state of the studied material. Two scenarios should be considered when executing high-resolution experiments. First, we should focus on the detection of core-to-core decay channels, such as K_α X-ray emission, that are characterized by a relatively high probability of decay and, consequently, high X-ray yields. Detection of core-to-core emission is also important when experimental data are to be supplemented with theoretical calculations. For core-to-core transitions, the initial and final states are easily described in a multielectron picture and therefore are easy to implement in many computing codes. In the second alternative, the XES detection can focus on K_β or even valence-to-core X-ray emission. These signals are very rich in information regarding the chemical and spin state of the studied system. However, the measured intensities are much weaker compared to core-to-core transitions, and the eventual implementation of theoretical models may require sophisticated optimization methods. We can definitively state that the high-resolution detection schemes are necessary for two reasons, namely, the determination of the valence electronic orbitals from the valence-to-core XES data and the precise determination of conduction electronic states from high-resolution XAS data. As mentioned, the latter is especially important for Cu-oxide since a weak pre-edge feature is smeared out in conventional XAS spectra due to the relatively large natural broadening of the $1s$ core state.

4. Conclusions

To conclude, the surface of Cu NPs can be altered through the use of different oxidizing agents, and X-ray spectroscopy represents a perfect tool to study the near-Fermi-level electronic states, which are most sensitive to the chemical environment and local structure of the material. The studied density of states (holes and electrons) will give a clear indication of the strength of the dephasing process at the NP surface–charge acceptor interface and thus enable quantitative analysis of a range of phenomena, such as the localized surface plasmon cooling mechanisms in metal NPs. The high energy resolution experiments will help to develop rational design schemes of plasmonic nanostructures for plasmon-enhanced solar-driven chemistry.

Acknowledgments

The work was partially funded by the National Science Centre in Poland under grant number 2020/37/B/ST3/00555. PETRA III at DESY Hamburg provided the beamtime under proposal I-20220429 EC (W. Stańczyk). The publication was partially developed under the provision of the Polish Ministry of Science and Higher Education project "Support for research and development with the use of infrastructure of the National Synchrotron Radiation Centre SOLARIS" under contract No. 1/SOL/2021/2.

References

[1] M.B. Gawande, A. Goswami, F.-X. Felpin, T. Asefa, X. Huang, R. Silva, X. Zou, R. Zboril, R.S. Varma, *Chem. Rev.* **116**, 3722 (2016).

[2] M.L. Brongersma, N.J. Halas, P. Nordlander, *Nat. Nanotechnol.* **10**, 25 (2015).

[3] Y. Xin, K. Yu, L. Zhang, Y. Yang, H. Yuan, H. Li, L. Wang, J. Zeng, *Adv. Mater.* **33**, 2008145 (2021).

[4] M.D. Susman, Y. Feldman, T.A. Bendikov, A. Vaskevich, I. Rubinstein, *Nanoscale* **9**, 12573 (2017).

[5] G.D.M.R. Dabera, M. Walker, A.M. Sanchez, H.J. Pereira, R. Beanland, R.A. Hatton, *Nat. Commun.* **8**, 1894 (2017).

[6] A. Marimuthu, J. Zhang, S. Linic, *Science* **339**, 1590 (2013).

[7] A. Gaur, D Shrivastava, S.K. Joshi, *J. Phys. Conf. Ser.* **190**, 012084 (2009).

[8] J. Szlachetko, D. Ferri, V. Marchionni, A. Kambolis, O.V. Safonova, Ch.J. Milne, O. Kröcher, M. Nachtegaal, J. Sá, *J. Am. Chem. Soc.* **135**, 19071 (2013).

[9] W. Błachucki, J. Hoszowska, J.-C. Dousse, Y. Kayser, R. Stachura, K. Tyrała, K. Wojtaszek, J. Sá, J. Szlachetko, *Spectrochim. Acta B At. Spectrosc.* **136**, 23 (2017).

Proceedings of the Zakopane School of Physics 2023 International Symposium, Zakopane, Poland, May 23–27, 2023

X-ray Photoelectron Spectroscopy in the Analysis of Titanium and Palladium Nanolayers

G. Wesołowski[a,*], A. Kubala-Kukuś[a], D. Banaś[a], K. Szary[a], I. Stabrawa[a], A. Foks[a], Ł. Jabłoński[a], P. Jagodziński[a], M. Pajek[a], R. Stachura[a], D. Sobota[a], M. Borysiewicz[b] and O. Sadowski[b]

[a] *Institute of Physics, Jan Kochanowski University, Uniwersytecka 7, 25-406 Kielce, Poland*
[b] *Łukasiewicz Research Network — Institute of Microelectronics and Photonics, al. Lotników 32/46, PL-02668 Warszawa, Poland*

Doi: 10.12693/APhysPolA.145.101 *e-mail: s131403@student.ujk.edu.pl

In the presented study, X-ray photoelectron spectroscopy and total reflection X-ray photoelectron spectroscopy methods were applied to analyze the Ti (75 nm) and Pd (100 nm) nanolayers deposited on the Si substrate using magnetron sputtering. The aim of the research was to determine the elemental composition and surface homogeneity of the analyzed nanolayers before their irradiation with highly charged xenon ions and to estimate the detection limit of the X-ray photoelectron spectroscopy technique for various glancing angles. The measurements were conducted using the SPECS mono-XPS system in the Institute of Physics at the Jan Kochanowski University (Kielce, Poland). The experimental setup and measurement conditions for the studied Ti and Pd layers are described. The X-ray photoelectron spectroscopy spectra were registered both for the non-total (35° and 10° angles) and total reflection (2.2° for the Pd nanolayer and 1.5° for the Ti nanolayer) regimes. The position of the C 1*s* photoelectron peak was applied (C–C component, binding energy 284.8 eV) to calibrate energy. First, the homogeneity of the nanolayers was investigated. The analysis of spectra concentrated on investigating the photoelectron peaks and, consequently, on determining the following: the binding energy of electrons, the intensity and full width at half maximum of photoelectron peaks, the background level, and the elemental composition of the nanolayer surface. In this study, the detection limit of the X-ray photoelectron spectroscopy measurements for different photoelectron peaks was calculated in relation to the excitation angle. An improvement of the X-ray photoelectron spectroscopy detection limit by a factor of 3–6, depending on the type of photoelectron peak, was observed for the angles below the critical angle of the X-ray total reflection phenomenon.

topics: Ti and Pd nanolayers, X-ray photoelectron spectroscopy (XPS), total reflection XPS

1. Introduction

X-ray photoelectron spectroscopy (XPS) is a surface analysis technique in which a low-energy X-ray beam is directed toward the studied sample, which leads to emitting electrons from the surface. Analyzing the registered energy spectra of the electrons provides information about such properties of the surface as qualitative and quantitative elemental composition, surface homogeneity, and the chemical environment of elements [1, 2]. The sensitivity of the X-ray photoelectron spectroscopy technique can be improved by applying the phenomenon of total reflection of X-ray radiation when the excitation beam is directed at the analyzed sample at an angle smaller than the critical angle [3]. This type of the modified technique is known as the total reflection X-ray photoelectron spectroscopy (TRXPS) [4–8]. Under the total reflection geometrical condition, primary X-rays cannot penetrate deeply into the analyzed sample. The intensity of X-rays in the evanescent range can be as much as four times stronger compared to the intensity of the primary X-ray beam. This is caused by forming a standing wave on the surface [4]. Consequently, the photoelectron signal is increased with simultaneous background reduction, which is also caused by a lower inelastic scattering of electrons [4]. Specific aspects of measurement geometry in the regime of total external reflection of X-ray is physical basis of low-angle X-ray spectroscopy, diffraction, and reflectometry techniques such as total reflection X-ray fluorescence (TXRF) [3], grazing incidence X-ray fluorescence (GIXRF) [3], grazing emission X-ray fluorescence (GEXRF) [3, 9, 10], grazing incidence X-Ray diffraction (GIXRD) [11], and the X-ray reflectometry [12]. These techniques are often used to analyze nanolayers, which facilitates determining various properties of sample surfaces, e.g., elemental and chemical composition, morphology, density,

thickness, roughness, and depth profile, also by our atomic physics and nanophysics group, in different applications [3, 13–15].

The research conducted by our group focuses on studying the processes of forming surface nanostructures in the interaction of highly charged xenon ions with nanolayers using the Kielce EBIS facility of the Jan Kochanowski University (Kielce, Poland) [16]. Research centers on metallic (Au, Ti) nanolayers [15, 17] as well as the dependence of nanostructure sizes on the kinetic and potential energy of the Xe ions. In order to continue the study for other metallic nanolayers (with different thickness values) and to interpret the results correctly, it is necessary to know the properties of the nanolayers obtained by applying X-ray photoelectron spectroscopy with the best possible detection limit.

In the presented studies, the XPS technique was applied to analyze titanium (Ti) and palladium (Pd) nanolayers deposited on the silicon (Si) substrate. In the case of titanium, the nanolayer thickness was 75 nm, whereas for palladium, it was 100 nm. The analysis was conducted both in the non-total and total X-ray reflection conditions. In the presented studies, titanium and palladium were selected for the research of nanolayer surface modifications in interaction with highly charged Xe ions, but in general, Ti and Pd materials are commonly used in various applications [18–21].

The paper begins with a description of the experimental setup, the measurement conditions, and the analyzed samples. Calculating the critical angle of the total X-ray reflection is also discussed. Next, the results and discussion section is presented. At the beginning of the section, the XPS survey spectra are presented for different regions of the nanolayer surface. Analyzing the spectra concentrates on interpreting photoelectron and Auger peaks as well as on determining the nanolayer surface elemental composition. Furthermore, surface homogeneity is discussed. Comparing the spectra registered for different glancing angles (both for the Ti and Pd nanolayers) is an important aspect of the study. In this case, analyzing the spectra focuses on determining the binding energy of electrons, the intensity and the full width at half maximum (FWHM) of photoelectron peaks, the background level, and the elemental composition of the nanolayer surface. This, in turn, enables the specification of the XPS/TRXPS detection limit for various photoelectron peaks.

2. Experiment

2.1. Samples description

The research included analyzing titanium (Ti) and palladium (Pd) layers (75 nm and 100 nm in thickness, respectively). The layers were deposited on a silicon (Si wafers, standard $\langle 111 \rangle$ orientation) substrate. The samples were prepared at the Łukasiewicz Research Network Institute of Microelectronics and Photonics in Warsaw, Poland, using magnetron sputtering in the thin film deposition system (TFDS) from VST Ltd. The preparation process was performed in the conditions of high vacuum ($4–5 \times 10^{-7}$ Pa). 4N purity materials were used as the targets. In this process, the deposition rate was 2 nm per second. The size of the prepared samples was 10 mm, 5 mm, and 1 mm in length, width, and thickness, respectively. The layer thickness was verified using a surface profilometer, Dektak 150 (Veeco Instruments Inc.).

2.2. Experimental setup and measurement conditions

The X-ray photoelectron spectroscopy and the total reflection X-ray photoelectron spectroscopy measurements were performed with the SPECS mono-XPS system using monochromatized Al K_α radiation with an energy of 1486.7 eV emitted from an XR-50 M high-intensity twin anode (Al, Ag) X-ray source optimized for XPS experiments. The X-ray tube (300 W) was operated with a voltage $U = 15$ kV and current $I = 20$ mA. The X-ray beam monochromatization was performed with a quartz single-crystal mirror monochromator with a 500 mm Rowland circle and a rocking curve width of approximately 160 meV.

The XPS and TRXPS spectra were obtained utilizing a PHOIBOS 100 electron energy analyzer equipped with a one-dimensional delayline detector (1D-DLD). The vacuum chamber pressure was about 10^{-9} mbar. The pass energy of 30 eV was selected to analyze the nanolayers under both non-total and total X-ray reflection conditions. Spectrometer calibration was checked using the Ag reference foil (Goodfellow), applied for analyzing two photoelectron peaks: Ag $3d_{3/2}$ and Ag $3d_{5/2}$. The position of the Ag $3d_{3/2}$ peak was 374.3 eV, whilst for Ag $3d_{5/2}$, it was 368.4 eV, matching the reference values [22]. The FWHM of Ag $3d$ peaks was 1 eV. The Pd and Ti nanolayer samples studied with the TRXPS measurements were automatically tilted with a manipulator, standard LN2 1.5, a device offering three-axes (x, y, z) and two-angular (polar, azimuth) movements. The polar rotation precision equaled 0.05°. The measurements also involved charge compensation, achieved with the assistance of a flood gun FG-500. The following values were applied for the Pd nanolayer: electron energy of 0.4 eV, emission current of 4 μA. In the case of the Ti nanolayer, these values were 0.7 eV for electron energy and 15 μA for the emission current.

2.3. Critical angle of total X-ray reflection

TRXPS measurements require selecting the measurement angle (i.e., the glancing angle), which has to be below the critical angle, which is characteristic

for a given X-ray beam energy and the type of the reflecting surface (nanolayers). The critical angle can be calculated from the following equation

$$\theta_c = C\sqrt{\frac{Z\,\rho}{A}}\frac{1}{E}, \tag{1}$$

where Z, A, and ρ [g/cm^3] are the atomic number, the mass number, and the surface material density, respectively; E [keV] is the X-ray energy, and C is a constant equal to 1.65 for the assumed units of the discussed physical quantities. Taking into account the energy of Al K_α X-ray (1486.7 eV), used as the excitation radiation in XPS/TRXPS measurements, the critical angle for Ti is 1.60° and for Pd is 2.37° [23]. A relatively high value of the critical angles, compared to the values applied in the low-angle spectroscopy, is a consequence of the low energy of the X-ray beam. In the presented studies, the XPS measurements were performed for the following angles: 35° and 10° (Pd and Ti nanolayers), 2.2° (Pd nanolayers, X-ray total reflection condition) and 1.5° (Ti nanolayers, X-ray total reflection condition).

3. Result and discussion

3.1. Survey spectra. Surface homogeneity

The homogeneity of the nanolayer surface was established by measuring the XPS survey spectra at an angle of 35°for five areas on the sample (i.e., the center and four corners of the sample). Figure 1

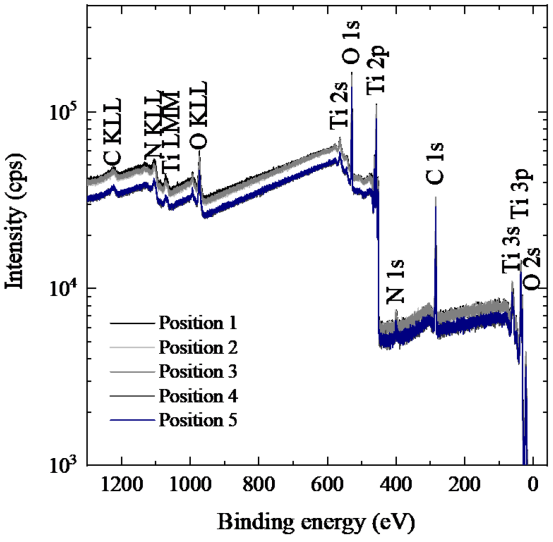

Fig. 1. XPS survey spectra of Ti 75 nm nanolayer deposited on the silicon (Si) substrate for five areas on the sample measured at a glancing angle of 35°. The sample was irradiated by the monochromatized Al K_α photons. In the spectra, both photoelectron (Ti 2s, O 1s, Ti 2p, N 1s, C 1s, Ti 3s, Ti 3p, O 2s) and Auger peaks (C-KLL, N-KLL, Ti-LMM, O-KLL) were identified.

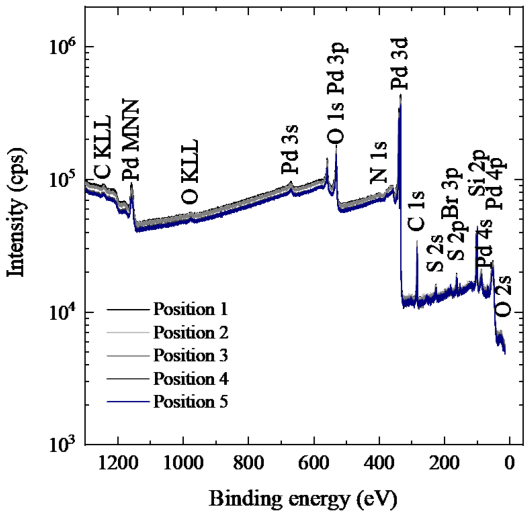

Fig. 2. XPS survey spectra of Pd 100 nm nanolayer deposited on the silicon (Si) substrate for five areas on the sample measured at a glancing angle of 35°. The sample was irradiated by the monochromatized Al K_α photons. In the spectra, both photoelectron (Pd 3s, Pd 3p, O 1s, N 1s, Pd 3d, C 1s, S 2s, Br 3p, S 2p, Si 2p, Pd 4s, Pd 4p, O 2s) and Auger peaks (C-KLL, Pd-MNN, O-KLL) were identified.

presents the XPS survey spectra registered for the Ti nanolayer (75 nm) deposited on the silicon. The survey spectra were measured in the electron binding energy range from 0 to 1300 eV. The energy step was 0.1 eV, and the dwell time was 0.1 s. For energy calibration, the position of the C 1s photoelectron peak was applied (C–C component, binding energy 284.8 eV). In the spectra, both photoelectron (O 1s, Ti 2s, Ti 2p, N 1s, C 1s, Ti 3s, Ti 3p, O 2s) and Auger peaks (C-KLL, N-KLL, Ti-LMM, O-KLL) were identified. In the spectrum, the photoelectron Ti 2p peak was registered as Ti 2$p_{1/2}$ and Ti 2$p_{3/2}$ splitting. A detectable quantity of adventitious carbon contamination was observed in the sample due to its exposition to the atmosphere. Similarly, the presence of adventitious nitrogen from air exposure could be observed in the spectra, however, the observed amount was considerably smaller.

In the case of oxygen, this element is present on the samples due to the exposition to the atmosphere, either due to adventitious contamination, oxidation, or water.

Figure 2 presents the XPS survey spectra of the Pd nanolayer (100 nm) deposited on the silicon measured at the angle of 35° for five areas on the sample. The survey spectra were measured in the electron binding energy range from 0 to 1300 eV. The measured energy step was 0.1 eV, and the dwell time was 0.1 s. In the spectra, both the photoelectron (Pd 3s, Pd 3p, O 1s, N 1s, Pd 3d, C 1s, S 2s, Br 3p, S 2p, Si 2p, Pd 4s, Pd 4p, O 2s) and Auger peaks (C-KLL, Pd-MNN, O-KLL) were identified. Moreover, the following splitting was

TABLE I

Element concentrations [at.%] on Pd and Ti surface nanolayers for five various regions of the nanolayer surface measured at an angle of 35°. The table presents element concentration mean values, standard deviations, and the coefficients of variation.

Elements	Concentration [at.%]					Mean value [at.%]	Standard deviation [at.%]	Variation coefficient [%]
	Position 1	Position 2	Position 3	Position 4	Position 5			
100 nm palladium nanolayer								
Palladium	41.2	41.6	41.6	29.6	31.3	37.1	5.4	14.7
Silicon	23.3	22.2	15.5	36.6	36.7	26.8	8.4	31.3
Carbon	18.4	20.8	24.3	18.3	17.4	19.8	2.5	12.7
Oxygen	9.7	8.4	10.8	8.9	8.6	9.3	0.9	9.5
Sulfur	4.0	3.4	3.8	3.1	3.2	3.5	0.3	9.7
Nitrogen	3.1	2.9	3.4	2.9	2.2	2.9	0.4	13.4
Bromine	0.4	0.8	0.6	0.7	0.7	0.6	0.1	20.7
75 nm titanium nanolayer								
Oxygen	46.9	45.7	45.3	45.5	45.5	45.8	0.6	1.3
Carbon	25.8	28.5	28.5	28.7	28.3	28.0	1.1	3.9
Titanium	25.7	24.7	24.9	23.9	24.8	24.8	0.6	2.3
Nitrogen	1.6	1.2	1.3	1.9	1.4	1.5	0.2	16.8

noticed: Pd $3p_{1/2}$ and Pd $3p_{3/2}$, Pd $3d_{3/2}$ and Pd $3p_{5/2}$, Pd $4p_{1/2}$ and Pd $4p_{3/2}$. Additionally, the overlapping of the Pd $3p_{3/2}$ and the O $1s$ photoelectron peaks was observed as well.

Similarly to the survey spectrum of titanium, elements originating from the atmosphere are visible (C, N, O). Furthermore, elements such as bromine (Br), sulfur (S), and silicon (Si) can be observed as well. The presence of the silicon photoelectron peak (from the silicon substrate) in the recorded XPS spectra is evidence that the Pd layer is not uniform.

The registered survey spectra were used to identify the elemental composition of the studied nanolayers. The quantitative analysis of elemental composition was performed with the CasaXPS software. Table I presents element concentrations [at.%] on the Pd and Ti surface nanolayers for various positions and the calculated mean values, standard deviations, and coefficients of variation [%]. For the Pd nanolayer surface, the following mean element concentrations were obtained: palladium (37.1 at.%), silicon (26.8 at.%), carbon (19.8 at.%), oxygen (9.3 at.%), sulfur (3.5 at.%), nitrogen (2.9 at.%), and bromine (0.6 at.%). Standard deviations were in the range from 0.1 at.% (Br) to 8.4 at.% (Si), resulting in a variation coefficient at the level of 10–30%. The most significant concentration variation was noticed for silicon (31%), while the Pd concentration changed by about 15%.

For the Ti nanolayer surface, the following mean composition was obtained: oxygen (45.8 at.%), carbon (28.0 at.%), titanium (24.8 at.%), and nitrogen (1.5 at.%). Standard deviations were in the range from 0.2 at.% (N) to 1.1 at.% (C), resulting in a variation coefficient at a level of 1–17%. The largest variation in concentration was observed for nitrogen (16.8%), while the Ti concentration changed within 2%.

Comparing the results for the Ti and Pd nanolayers, it can be seen that the coefficient of variation is particularly greater when evaluating elemental concentrations within the sample of palladium nanolayers. This suggests that the Pd nanolayer sample shows a certain degree of surface heterogeneity, which is probably influenced by the sputtering parameters.

3.2. Comparison of spectra for different glancing angles

In the presented study, the X-ray photoelectron spectroscopy was applied both in non-total and total reflection of primary X-ray beam conditions in order to compare between XPS and TRXPS techniques signal-to-noise ratio determining the detection limit. Applying the TRXPS method should improve the value of the element detection limit.

In order to investigate the relationship between the detection limit and the incidence angle, spectra for three angles were collected, namely the typical XPS glancing angle (35°) and the intermediate value of angle (10°) for both samples, and an angle value below the critical angle (2.2° for Pd and 1.5° for Ti), for the center area on the samples.

Figures 3 and 4 present the XPS and TRXPS survey spectra of the Ti nanolayer (75 nm) and Pd nanolayer (100 nm), respectively, deposited on the silicon (Si), for different glancing angles. The decrease in the intensities of the TRXPS spectra compared to those at intermediate angles is related to the change in the primary beam area on the sample surface for different angles.

Table II presents element concentrations [at.%] on the Pd and Ti surface nanolayers obtained from survey spectra registered for the following angle values: 35°, 10°, 2.2°(Pd), and 1.5°(Ti). In addition, Table II also provides element concentration mean

TABLE II

Element concentrations [at.%] on the Pd and Ti surface nanolayers obtained from survey spectra registered for angle values of 35°, 10°, 2.2°(Pd), and 1.5°(Ti). The table shows element concentration mean values, standard deviations, and the coefficients of variation.

Elements	Concentration [at.%]				Mean	Standard	Variation
	angle 35°	angle 10°	angle 2.2°	angle 1.5°	value [at.%]	deviation [at.%]	coefficient[%]
100 nm palladium nanolayer							
Palladium	40.1	37.5	35.6	–	37.7	2.3	6.0
Silicon	20.5	22.7	24.7	–	22.6	2.1	9.2
Carbon	25.3	26.4	27.4	–	26.4	1.1	4.1
Oxygen	6.2	5.3	4.9	–	5.5	0.7	12.1
Sulfur	4.2	4.2	3.9	–	4.1	0.2	4.7
Nitrogen	3.5	3.7	3.3	–	3.5	0.2	5.7
Bromine	0.28	0.20	0.26	–	0.25	0.04	16.9
75 nm titanium nanolayer							
Oxygen	45.4	45.3	–	43.7	44.8	0.95	2.1
Carbon	26.5	29.1	–	32.4	29.3	3.0	10.2
Titanium	27.1	24.5	–	22.4	24.7	2.4	9.3
Nitrogen	1.1	1.2	–	1.4	1.2	0.15	12.5

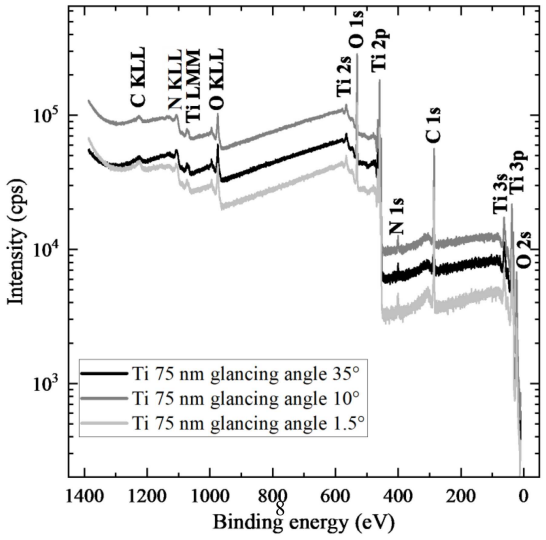

Fig. 3. XPS survey spectra of Ti 75 nm nanolayer deposited on the silicon (Si) substrate for different glancing angles: 35°, 10°, and 1.5° (below the critical angle for Ti (1.60°)). The sample was irradiated by the monochromatized Al K_α photons. In the spectra, both photoelectron (O 1s, Ti 2s, Ti 2p, N 1s, C 1s, Ti 3s, Ti 3p, O 2s) and Auger peaks (C-KLL, N-KLL, Ti-LMM, O-KLL) were identified.

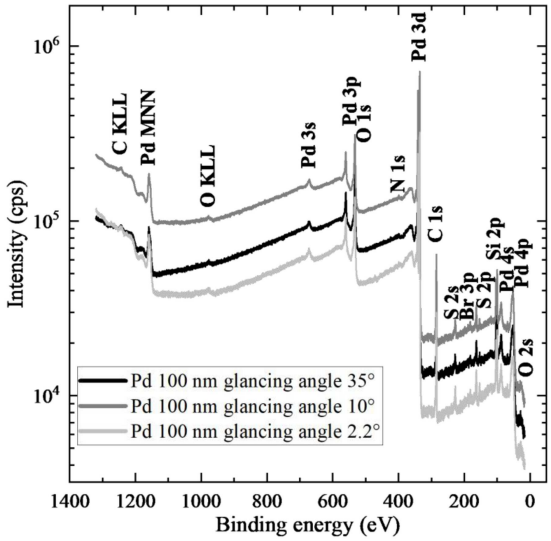

Fig. 4. XPS survey spectra of Pd 100 nm nanolayer for different glancing angles: 35°, 10°, and 2.2° (below the critical angle for Pd (2.37°)). The sample was irradiated by the monochromatized Al K_α photons. In the spectra, both photoelectron (Pd 3s, Pd 3p, O 1s, N 1s, Pd 3d, C 1s, S 2s, Br 3p, S 2p, Si 2p, Pd 4s, Pd 4p, O 2s) and Auger peaks (C-KLL, Pd-MNN, O-KLL) were identified.

values, standard deviations, and the coefficients of variation. For the Pd nanolayer surface, the following mean element concentrations were achieved: palladium (37.7 at.%), silicon (22.6 at.%), carbon (26.4 at.%), oxygen (5.5 at.%), sulfur (4.1 at.%), nitrogen (3.5 at.%), and bromine (0.25 at.%). Standard deviations were in the range from 0.04 at.% (Br) to 2.3 at.% (Pd), resulting in a variation coefficient at the level of 5–17%. The largest variation in concentration was observed for bromine (17%), probably due to low concentration, while the Pd concentration changed within about 6%.

For the Ti nanolayer surface, the following mean composition was obtained: oxygen (44.8 at.%), carbon (29.3 at.%), titanium (24.7 at.%), and nitrogen (1.2 at.%). Standard deviations were in the range

TABLE III

The detection limit for the XPS/TRXPS techniques obtained for photoelectron peaks identified at the surface of the Ti nanolayer (75 nm), based on the survey spectra registered for various glancing angles.

Photoelectron peak	Binding energy [eV]	FWHM [eV]	Limit of detection [at.%]		
			angle 35°	angle 10°	angle 1.5°
O 2s	21.5	2.79	1.229 ± 0.066	0.557 ± 0.020	0.298 ± 0.009
Ti 3p	36.7	2.67	0.452 ± 0.048	0.188 ± 0.020	0.084 ± 0.009
Ti 3s	61.6	4.44	1.396 ± 0.153	0.556 ± 0.060	0.276 ± 0.031
C 1s	284.8	1.53	0.275 ± 0.034	0.108 ± 0.012	0.048 ± 0.005
N 1s	399.3	1.25	0.120 ± 0.020	0.067 ± 0.010	0.036 ± 0.004
Ti 2p (Ti 2$p_{3/2}$)	458.3	1.57	0.126 ± 0.012	0.047 ± 0.005	0.022 ± 0.002
O 1s	529.8	1.48	0.246 ± 0.006	0.103 ± 0.002	0.053 ± 0.001
Ti 2s	564.3	4.81	1.459 ± 0.145	0.611 ± 0.063	0.291 ± 0.032

from 0.15 at.% (N) to 3.0 at.% (C), which resulted in the variation coefficient at the level of 2–13%. The most significant variation in concentration was observed for nitrogen (13%), while the Ti concentration changed within about 9%.

3.3. XPS/TRXPS detection limit

The analysis of the XPS/TRXPS spectra, which focused on the photoelectron peaks intensity and the level of background, enabled estimating the detection limit (DL) of these techniques, which can be calculated using the following formula

$$\mathrm{DL} = \frac{3\,C}{I_n}\sqrt{\frac{I_b}{t}}, \tag{2}$$

where C is the element concentration in the studied nanolayer probed by the XPS/TRXPS technique, I_n is the net intensity of the analyzed photoelectron peak, I_b is the background level under this peak, and t is the measurement dwell time.

Table III presents the detection limit achieved for element photoelectron peaks identified at the surface of the Ti nanolayer (75 nm) deposited on a silicon substrate, based on the survey spectra registered for 35°, 10°, and 1.5° (total reflection regime) angles. In the case of the Ti 2p photoelectron peak, the Ti 2$p_{3/2}$ component was analyzed.

Table III also presents the binding energy and FWHM of the photoelectron peaks, calculated as the average of values from measurements performed for the discussed angles. The standard deviation for the mean value of the binding energy is at the level of 0.1 eV, while the standard deviation for the average value of the FWHM is about 0.4 eV. Element concentration needed for calculating DL was assumed as a mean value achieved from the survey spectra registered for angles 35°, 10°, and 1.5° (Table II).

In calculating the detection limits, the change in the surface area of the primary beam associated with the change in the glancing angle was taken into account. The ratio of the primary X-ray beam area at 1.5° to the beam area at 35° reached approximately 22, while the ratio of the beam area at 2.2° to the beam area at 35° was approximately 15, and, finally, at 10° it was 3.3.

The obtained values of DL depend on the glancing angle and vary in range from 0.120 to 1.459 at.% for 35°, from 0.047 to 0.611 at.% for 10°, and, finally, from 0.022 to 0.298 at.% for 1.5°. It can be observed that the application of the primary X-ray beam total reflection reduces DL by a factor of about 3-6 compared to the classical XPS conditions.

Moreover, for the given element, e.g., Ti or O, the detection limit value depends on the type of the analyzed photoelectron peak and is the lowest for the strongest peak. In the case of titanium, it is the Ti 2p photoelectron peak, while for oxygen, it is O 1s.

The DL uncertainty was determined using the total differential method, taking as the uncertainty of the element concentration the standard deviation determined from the measurements of the survey spectra for different angles (Table II). The square root of the intensity was taken as the uncertainty of the intensity.

As can be seen in Table III, the relative uncertainty of the detection limit reaches 3–17%, with an average of 10%. Finally, the lowest value of detection limit, for the 75 nm Ti nanolayer, was achieved for the Ti 2p peak, for angle 1.5°, being equal to $0.022 \pm 0.002 at.\%$.

Table IV presents the detection limits for element photoelectron peaks identified at the Pd nanolayer (100 nm) surface deposited on the silicon substrate, based on the survey spectra registered for 35°, 10°, and 2.2° (total reflection regime) angles. In the case of Pd 3p, the Pd 3$p_{3/2}$ was analyzed. For Pd 3d, it was Pd 3$p_{5/2}$, and for Pd 4p, it was Pd 4$p_{3/2}$. Table IV also contains the values of the binding energy and the FWHM of photoelectron peaks, which were calculated as an average of values from the measurements performed for the discussed angles. The standard deviation for the mean value of the

TABLE IV

The detection limit for the XPS/TRXPS techniques obtained for photoelectron peaks identified at the surface of the 100 nm Pd nanolayer, based on the survey spectra registered for various glancing angles.

Photoelectron peak	Binding energy [eV]	FWHM [eV]	Limit of detection [at.%]		
			angle 35°	angle 10°	angle 2.2°
O 2s	23.0	0.40	1.354 ± 0.203	0.761 ± 0.115	0.340 ± 0.053
Pd 4p	51.5	8.16	0.847 ± 0.060	0.381 ± 0.026	0.228 ± 0.016
Br 3d	68.6	0.77	0.044 ± 0.007	0.021 ± 0.004	0.010 ± 0.002
Pd 4s	87.6	4.00	2.602 ± 0.193	1.188 ± 0.082	0.556 ± 0.039
Si 2p	99.8	0.99	0.526 ± 0.060	0.230 ± 0.022	0.153 ± 0.014
Br 3p	163.3	2.31	0.054 ± 0.009	0.022 ± 0.004	0.012 ± 0.002
S 2p	181.8	0.95	0.300 ± 0.020	0.118 ± 0.007	0.063 ± 0.004
S 2s	227.6	2.08	0.327 ± 0.022	0.176 ± 0.010	0.077 ± 0.004
C 1s	284.8	1.57	0.361 ± 0.020	0.143 ± 0.007	0.084 ± 0.004
Pd 3d	335.5	1.41	0.055 ± 0.003	0.022 ± 0.001	0.013 ± 0.001
N 1s	399.1	0.88	0.591 ± 0.043	0.282 ± 0.017	0.156 ± 0.010
Pd 3p	532.6	3.14	0.303 ± 0.019	0.123 ± 0.008	0.072 ± 0.005
Pd 3s	672.1	5.71	3.641 ± 0.251	1.297 ± 0.086	0.765 ± 0.052

binding energy was at the level of 0.3 eV, and the standard deviation for the mean value of the FWHM was also about 0.3 eV. Element concentration necessary for calculating DL was assumed as a mean value from the survey spectra registered for the following angles: 35°, 10°, and 2.2° (Table II).

As for the Ti nanolayer, the obtained values of DL depended on the glancing angle and varied from 0.044 to 3.641 at.% for angle 35°, from 0.021 to 1.297 at.% for 10°, and, finally, from 0.010 to 0.765 at.% for 2.2°. It can be observed that applying the primary X-ray beam total reflection reduced the DL by a factor of about 3–5 compared to the classical XPS conditions.

For Pd, the value of the detection limit depends on the type of analyzed photoelectron peak and is the lowest for the strongest peak Pd 3d (i.e., Pd $3p_{5/2}$).

As can be seen in Table IV, the relative uncertainty of the detection limit was at 5–18%, with an average of about 10%. Finally, the lowest value of detection limit, for the 100 nm Pd nanolayer, was achieved for an angle of 1.5° ($0.010 \pm 0.002 at.\%$).

4. Conclusions

In the presented study, the X-ray photoelectron spectroscopy in the non-total and total reflection conditions was applied to analyze the Ti (75 nm) and Pd (100 nm) nanolayers deposited on Si substrate with magnetron sputtering. The survey spectra were registered for different glancing angles, i.e., 35°, 10°, and 2.2° for the Pd nanolayer and 1.5° for the Ti nanolayer. The analysis of the spectra concentrated on examining the binding energy, the FWHM, the intensity, and the background level for the registered photoelectron peaks. The nanolayer surface homogeneity, defined by the variation coefficient of element concentration, was obtained as 2.3% for Ti and 14.7% for the Pd sample. The obtained detection limit for XPS/TRXPS was in the range from 0.010 to 3.6 at.%, depending on the glancing angle, nanolayer, and photoelectron peak of the detected element. In general, the application of total reflection X-ray photoelectron spectroscopy geometry improves the detection limit of the X-ray photoelectron spectroscopy technique by a factor of 3–6, depending on the analyzed nanolayer and the type of photoelectron peak.

Knowledge of the properties of the Ti and Pd nanolayer surfaces will be applied to interpret the results of the studies conducted at the Institute of Physics of Jan Kochanowski University, related to the formation of the nanostructures in the interaction of the highly charged xenon ions with nanolayers. The XPS/TRXPS analysis of other metallic nanolayers will serve as the continuation of the presented studies.

Acknowledgments

The equipment was purchased thanks to the financial support of the European Regional Development Fund in the framework of the Polish Innovative Economy Operational Program (contract No. WNPPOIG.02.02.00-26-023/08) and the Development of Eastern Poland Program (contract No. POPW.01.01.00-26-013/09-04). The functioning of the facility is supported by the Polish Ministry of Education and Science (project 28/489259/SPUB/SP/2021).

This article is based upon work from COST Action CA18130 ENFORCE TXRF, supported by COST (European Cooperation in Science and Technology, www.cost.eu).

References

[1] P. van der Heide, *X-ray Photoelectron Spectroscopy: An Introduction to Principles and Practices*, John Wiley & Sons, Hoboken (NJ) 2011.

[2] D. Baer, M. Engelhard, *J. Electron. Spectrosc. Relat. Phenom.* **178–179**, 415 (2010).

[3] R. Klockenkämper, A. Von Bohlen, *Anal. Bioanal. Chem.* **408**, 667 (2016).

[4] J. Kawai, *J. Electron. Spectrosc. Relat. Phenom.* **178–179**, 268 (2010).

[5] J. Kawai, M. Takami, M. Fujinami, Y. Hashiguchi, S. Hayakawa, Y. Gohshi, *Spectrochim. Acta B* **47**, 983 (1992).

[6] J. Kawai, H. Amano, K. Hayashi, T. Horiuchi, K. Matsushige, Y. Kitajima, *Spectrochim. Acta B* **52**, 873 (1997).

[7] A. Alshehabi, N. Sasaki, J. Kawai, *Spectrochim. Acta B* **114**, 34 (2015).

[8] A. Kubala-Kukuś, D. Banaś, I. Stabrawa, K. Szary, D. Sobota, U. Majewska, J. Wudarczyk-Moćko, J. Braziewicz, M. Pajek, *Spectrochim. Acta B* **145**, 43 (2018).

[9] H.P. Urbach, P.K. de Bokx, *Phys. Rev. B* **53**, 3752 (1996).

[10] J. Baumann, Y. Kayser, B. Kanngießer, *Phys. Status Solidi B* **258**, 2000471 (2021).

[11] P. Dutta, *Curr. Sci.* **78**, 478 (2000).

[12] K. N. Stoev, K. Sakurai, *Spectrochim. Acta B* **54**, 41 (1999).

[13] A. Kubala-Kukuś, D. Banaś, M. Pajek et al., *Acta Phys. Pol. A* **139**, 247 (2021).

[14] I. Stabrawa, A. Kubala-Kukuś, D. Banaś, G. Pepponi, J. Braziewicz, M. Pajek, M. Teodorczyk, *Thin Solid Films* **671**, 103 (2019).

[15] R. Stachura, D. Banaś, A. Kubala-Kukuś et al., *Nucl. Instrum. Method B* **536**, 126 (2023).

[16] D. Banaś, Ł. Jabłoński, P. Jagodziński, A. Kubala-Kukuś, D. Sobota, M. Pajek, *Nucl. Instrum. Method B* **354**, 125 (2015).

[17] I. Stabrawa, D. Banaś, A. Kubala-Kukuś et al., *Vacuum* **210**, 111860 (2023).

[18] X. Liu, P. Chu, C. Ding, *Mater. Sci. Eng. R* **47**, 49 (2004).

[19] S. Cao, D. Li, A.A. Uliana et al., Y. Jiang, J. Zhu, Y. Zhang, B. Van der Bruggen, *Appl. Catal. B* **323**, 22175 (2023).

[20] M. Polívková, M. Valová, J. Siegel, S. Rimpelová, T. Hubáček, O. Lyutakova, V. Švorčika, *RSC Adv.* **5**, 73767 (2015).

[21] N. Kim, H.H. Cho, Y. Kim et al., *Int. J. Hydrog. Energy* **48**, 1234 (2023).

[22] A. Naumkin, A. Kraut-Vass, S. Gaarenstroom, C. Powell, NIST Standard Reference Database 20, Ve4. 4.1, 2012.

[23] Center for X-Ray Optics, X-Ray Properties of the Elements.

Proceedings of the Zakopane School of Physics 2023 International Symposium, Zakopane, Poland, May 23–27, 2023

Magnetic Properties of the Thin Films of Prussian Blue Analogues Obtained by Ion-Exchange Synthesis

W. Sas[a,b], A. Pacanowska[a] and M. Fitta[a,*]

[a] *Institute of Nuclear Physics Polish Academy of Sciences, Radzikowskiego 152, 31-342 Kraków, Poland*
[b] *Institute of Physics, Bijenička 46, 10000 Zagreb, Croatia*

Doi: 10.12693/APhysPolA.145.109 *e-mail: magdalena.fitta@ifj.edu.pl

The Prussian blue analogues attract great attention due to their interesting properties and tunability. The cyanido bridging ligands allow for effective magnetic coupling. Due to the highly symmetrical structure of the Prussian blue analogue, its properties can be tuned by changing the metal centres involved in the cyano-bridging. Herein, a study of a new dimensionally-reduced system based on nickel hexacyanoferrate/chromate is presented. Thin films were obtained by ion-exchange synthesis. The primary aim of this work was to tune the physical properties of Prussian blue analogues by adapting the strategy of incorporating the three types of metal ions. A comprehensive analysis of the magnetic properties of the resulting compound and a detailed investigation of the evolution of the material's microstructure induced by the change in its chemical composition is presented.

topics: molecular magnetism, thin films, Prussian blue analogues

1. Introduction

The Prussian blue analogues (PBAs) $A_j M'_k[M(CN)_6]_l \cdot n\,H_2O$, where M' and M are $3d$ transition metal ions and A is an interstitial cation, attract great attention due to their rich palette of properties such as room-temperature ferromagnetism [1, 2], photomagnetism [3, [4], magnetic sensitivity to external pressure [5, 6], and the negative thermal expansion [7]. Thin films of PBAs are therefore considered as interesting materials for power supply and storage [8–11], ion-sieving membranes [12], or future molecule-based spintronic devices [13, 14]. One of the most important advantages of PBAs is their highly symmetrical structure. Depending on the stoichiometry and the charge of the cation, these systems reveal different structural motifs based on the highly symmetric, regular, and three-dimensional coordination network. Due to the cubic structure, the properties of PBAs can be tuned by changing the metal centres involved in the cyano-bridging.

One of the first examples of Prussian blue analogues composed of three types of metal ions was the mixed ferromagnet–ferrimagnet $(Ni^{II}xMn^{II}_{1-x})_{1.5}[Cr^{III}(CN)_6]\cdot 7.5\,H_2O$, which accommodated both ferromagnetic (J>0) and antiferromagnetic (J<0) exchange interactions [15]. For that series of compounds, obtained as a microcrystalline powder, a monotonous increase in Weiss temperature with the increase in nickel content was observed. Variation in structural and magnetic properties with composition was also reported for the $(Co_xNi_{1-x})_{1.5}[Fe(CN)_6] \cdot zH_2O$ series [16]. Next, the tunability of physical properties by controlling the compositional factor x was also achieved for thin films of $(Fe^{II}_x Cr^{II}_{1-x})_{1.5}[Cr^{III}(CN)_6] \cdot zH_2O$ [17] and $(V^{II/III}_x Cr^{II}_{1-x})_{1.5}[Cr^{III}(CN)_6]_y$ [18] synthesized by electrochemical deposition. Depending on the x value, the change in colour, critical temperature, and coercive field of the films were noted. The influence of metal components on the spectroscopic and magnetic properties was also demonstrated for cobalt hexacyanoferrate/chromate metal coordination nanopolymers [19].

The objective of the present work was to design and optimize a feasible and reproducible process for the synthesis of thin films from the PBAs family with tuned magnetic properties. The stoichiometry of the systems studied changes from $Ni_3[Cr(CN)_6]_2$ to $Ni_3[Fe(CN)_6]_2$ depending on the $[Cr(CN)_6]^{3-}$:$[Fe(CN)_6]^{3-}$ ratio, but the $Ni_3[M(CN)_6]_2$ core is maintained. The structure of the system reveals the face-center-cubic packing, thus allowing the formation of cyano linkages between Ni^{2+} cations and hexacyanometallate. In our previous paper [20], we have already reported on the synthesis and magneto-optical properties of $Ni_{1.5}[Fe(CN)_6]_x[Cr(CN)_6]_{1-x} \cdot nH_2O$ (x=0, 0.55,

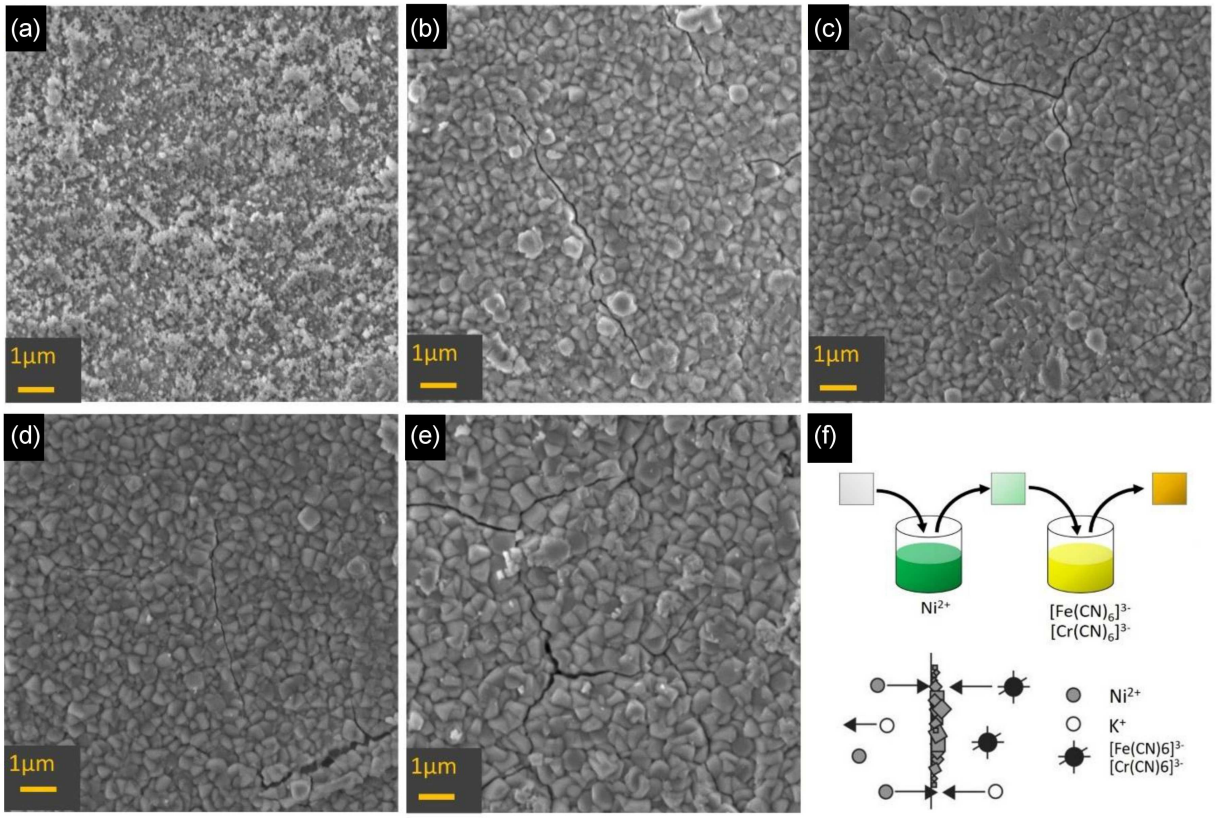

Fig. 1. SEM images of the films with various values of the compositional x factor (a) $x = 0$, (b) $x = 0.31$, (c) $x = 0.57$, (d) $x = 81$, and (e) $x = 1$. (f) The scheme of ion exchange deposition of PBA thin film.

and 1) thin films grown on silicon (100) and mica substrates. Now, we present thin film samples of the same family with the assumed x values as $x_{ass} = 0$, 0.25, 0.5, 0.75, and 1, deposited onto the Nafion®117 membrane. The effectiveness and composition accuracy of the film preparation technique were checked by scanning electron microscope (SEM), energy-dispersive X-ray spectroscopy (EDS), and magnetic measurements.

2. Materials and methods

2.1. Sample preparation

All reagents used in this study were purchased from commercial sources (Sigma-Aldrich) and used without further purification. In the first step of the film preparation by ion-exchange synthesis, a Nafion®117 membrane (1×2 cm^2) was immersed in an aqueous solution of $NiCl_2$ (200 mM) for 24 h. Then, it was rinsed with deionized (DI) water and placed in an aqueous solution of $K_3[Fe(CN)_6]$ and/or $K_3[Cr(CN)_6]$. The compositional factor x, $x = n_{Cr}/(n_{Cr}+n_{Fe})$, was varied from 0 to 1, keeping the total potassium hexacyanometalate concentration of 20 mmol. After completion of the synthesis, all membranes were washed again with deionized water and allowed to dry in ambient air.

2.2. Characterization methods

Microstructure and composition analysis of films was performed using a TESCAN VEGA3 scanning electron microscope equipped with an X-ray energy dispersive spectrometer EDAX Bruker.

Magnetic properties were measured using a Quantum Design MPMS-XL magnetometer. For magnetic measurements, the samples deposited on Nafion®117 were cut into pieces ca. 3×4 mm^2 in size, and subsequently, they were introduced into the sample holder oriented parallel to the applied magnetic field. For reference, the magnetic properties of the Nafion®117 substrate were measured independently under the same conditions and then subtracted from the raw data.

3. Results and discussion

3.1. SEM

The chemical composition of the thin films was determined by means of SEM and EDS. No fewer than three scans were recorded on different parts of each film and then averaged to give relative atomic percentages for the metallic elements. The calculated transition metal ratios are presented in Table I. Results of the elemental analysis showed

TABLE I

The chemical composition of $Ni_{1.5}[Fe(CN)_6]_x[Cr(CN)_6]_{1-x} \cdot nH_2O$ films deposited on Nafion®117.

x_{ass}	x	Ni [%]	Fe [%]	Cr [%]
0	0	33.5 ± 1.1	–	60.19 ± 0.88
0.25	0.31	30.7 ± 2.0	21.5 ± 1.0	47.8 ± 1.2
0.5	0.57	30.78 ± 0.74	39.32 ± 0.30	29.90 ± 0.80
0.75	0.81	31.3 ± 1.2	55.48 ± 0.88	13.27 ± 0.44
1	1	24.9 ± 2.8	75.1 ± 2.8	–

that the experimentally obtained x values are close to the x_{ass} assumed in the synthesis protocol, e.g., $x = 0.31$ ($x_{ass} = 0.25$), $x = 0.57$ ($x_{ass} = 0.50$), and 0.81 ($x_{ass} = 0.75$).

The surface morphology was examined by SEM. Figure 1 shows the microphotographs obtained for exemplary films. The morphology of the films consists of a collection of crystallites formed on the surface. The smallest crystallites were obtained for the NiCr sample, and their sizes do not exceed 100 nm. The grains are much larger (with diameters in the range of 600 to 800 nm) for samples with the highest Fe content. A reverse relationship has already been observed for PBA films obtained by "layer by layer" deposition, where films based on nickel hexacyanoferrate contain slightly smaller granules than hexacyanochromate films [21]. Another characteristic feature of PBA films observed in the SEM images are cracks seen on the surface.

3.2. Magnetic properties

It has also been demonstrated that the magnetic properties of the thin films depend on the metal elemental composition. Figure 2a shows the temperature dependence of the real component of the AC susceptibility measured for the films oriented parallel to the direction of an external magnetic field. For all compounds, sharp peaks are observed, revealing the presence of a long-range magnetic ordering below the respective critical temperatures. The critical temperatures T_c, determined as a minimum of χ' derivative, are equal to 26.6 K, 30.8 K, 40.4 K, 52.7 K, and 64 K for $x = 1$, 0.81, 0.57, 0.31, and 0, respectively. This means that the ordering temperature is shifted to the higher values with the decrease in Fe content in the samples.

Figure 2b shows the results of field-cooled (FC) magnetization measurements recorded for samples with the external magnetic field (100 Oe) applied parallel to the surface of the films. For all compounds, during cooling, the magnetic susceptibility increases slowly, then the signal goes up abruptly when passing the critical temperature, and finally, it saturates at low temperatures.

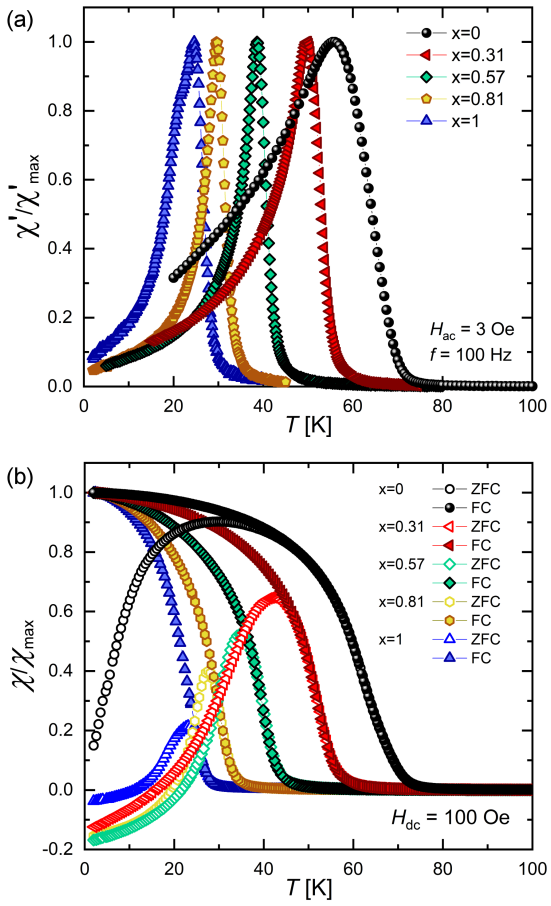

Fig. 2. (a) Temperature dependence of real component of AC susceptibility measured for films obtained with various values of the compositional x factor, oriented parallel to the direction of H_{dc}. (b) ZFC–FC magnetization vs temperature plots measured at an applied field of 100 Oe for films aligned parallel to the external field direction.

For all films with $x > 0$, the negative values of magnetization in the low-temperature range in the zero-field-cooling (ZFC) curve are observed. Typically, the occurrence of a negative magnetization value in $M(T)$ curves is associated with the compensation point, where the algebraic sum of sublattice magnetizations equals zero. The compensation temperature is anticipated to be independent of the external field magnitude. The presence of this compensation temperature has been observed in various PBA samples, both in bulk and thin films. In our case, all analyzed compounds are anticipated to exhibit ferromagnetic behaviour, then the negative magnetization may possibly be related to the presence of some negative remnant field of the superconducting magnet. A similar effect was previously observed for PBA thin films obtained by layer-by-layer deposition. Therefore, these deviations should be treated as measurement artifacts and not as an additional physical effect originating from the samples.

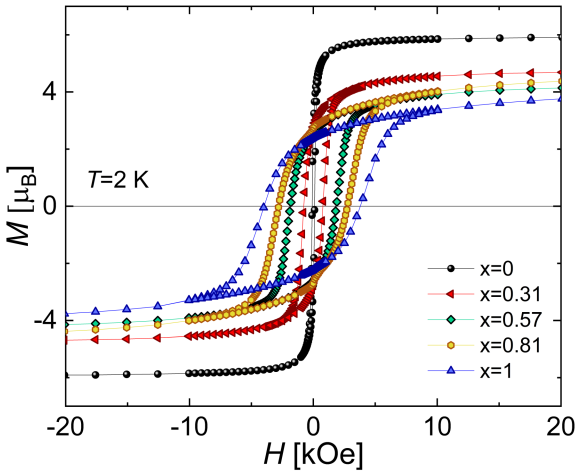

Fig. 3. Magnetization vs field measured at 2 K for $Ni_{1.5}[Fe(CN)_6]_x[Cr(CN)_6]_{1-x} \cdot nH_2O$ films.

TABLE II

Magnetic data for the $Ni_{1.5}[Fe(CN)_6]_x[Cr(CN)_6]_{1-x} \cdot n\,H_2O$ thin film samples.

x	T_c [K]	H_c [Oe]	M_S [μ_B]	θ [K]	C [emu K/mol]
0	64	100	5.9	81.56	4.19
0.31	52.7	770	4.78	67.86	3.46
0.57	40.4	1850	4.31	56.69	2.99
0.81	30.8	2780	4.66	46.64	3.03
1	26.6	3890	4.15	23.67	3.16

Additionally, the static magnetic susceptibility was measured for all of the films in the presence of the field of 500 Oe. Fitting the Curie–Weiss law to the experimental data in the form of $1/\chi(T)$ vs T in the temperature range 100–300 K gives the Curie constants and Weiss temperatures listed in Table II. The values of C as well as θ_{CW} increase monotonically with the increase in Cr content. Positive values of Weiss temperature determined for all films confirm the presence of ferromagnetic interaction between metal ions.

Figure 3 presents the dependence of the coercive field and critical temperature on the value of x. It is clearly seen that H_c, as well as T_c, changes monotonically with the change of parameter x. An increase in Fe content leads to an increase in the coercive field, whereas the critical temperature decreases. Taking into account the spin values $s_{Ni} = 1$, $s_{Fe} = 1/2$, $s_{Cr} = 3/2$, and $g = 2$, the theoretical saturation of magnetization of the $Ni_{1.5}[Fe(CN)_6]_x[Cr(CN)_6]_{1-x} \cdot n\,H_2O$ series should change from 6 μ_B ($x = 0$) to 4 μ_B ($x = 1$). The experimentally obtained values of M_s are close to those predicted theoretically. It means that the control of the Fe/Cr ratio allows for tuning the desired magnetic properties of the obtained compounds. The magnetic properties of deposited films are comparable to their bulk counterparts; in fact, small discrepancies between values of T_c, H_c, and M_s may be related to slightly different sample stoichiometry.

4. Conclusions

The development of modern science and technology requires novel and tunable magnetic materials. In this work, we have succeeded in designing a series of magnetic thin films composed of new types of PBAs incorporating three types of metal ions. The proper film formation and composition have been confirmed with the use of the EDS technique. The physical properties of the obtained films can be controlled by changing the compositional x factor. It has been demonstrated that the coercive field H_c, as well as the critical temperature T_c, changes monotonically with the change of the x parameter. An increase in the Fe content leads to a decrease in the critical temperature, whereas the coercive field increases. Moreover, our results show that the films' magnetic properties are compatible with their bulk counterpart.

References

[1] S. Ferlay, T. Mallah, R. Ouahčs, P. Veillet, M. Verdaguer, *Nature* **378**, 701 (1995).

[2] J.M. Manriquez, G.T. Yee, R.S. McLean, A.J. Epstein, J.S. Miller, *Science* **252**, 1415 (1991).

[3] T. Yamamoto, Y. Umemura, O. Sato, Y. Einaga, *Chem. Lett.* **33**, 500 (2004).

[4] H. Tokoro, T. Matsuda, T. Nuida, Y. Moritomo, K. Ohoyama, E.D.L. Dangui, K. Boukheddaden, S. Ohkoshi, *Chem. Mater.* **20**, 423 (2008).

[5] E. Coronado, M.C. Giménez-López, G. Levchenko, F.M. Romero, V. García-Baonza, A. Milner, M. Paz-Pasternak, *J. Am. Chem. Soc.* **127**, 4580 (2005).

[6] M. Zentková, Z. Arnold, J. Kamarád, V. Kavečanský, M. Lukáčová, S. Matáš, M. Mihalik, Z. Mitróová, A. Zentko, *J. Phys. Condens. Matter* **19**, 266217 (2007).

[7] K.W. Chapman, P.J. Chupas, C.J. Kepert, *J. Am. Chem. Soc.* **128**, 7009 (2006).

[8] L. Zhang, T. Meng, B. Mao, D. Guo, J. Qin, M. Cao, *RSC Adv.* **7**, 50812 (2017).

[9] Q. Wang, N. Wang, S. He, J. Zhao, J. Fang, W. Shen, *Dalt. Trans.* **44**, 12878 (2015).

[10] Z. Pan, Z. He, J. Hou, L. Kong, *Small* **19**, 2302788 (2023).

[11] Y. Moritomo, M. Sarukura, H. Iwaizumi, I. Nagai, *Batteries* **9**, 393 (2023).

[12] M. Pyrasch, A. Toutianoush, W. Jin, J. Schnepf, B. Tieke, *Chem. Mater.* **15**, 245 (2003).

[13] E. Coronado, *Nat. Rev. Mater.* **5**, 87 (2020).

[14] Y. Huang, S. Ren, *Appl. Mater. Today* **22**, 100886 (2021).

[15] S. Ohkoshi, T. Iyoda, A. Fujishima, K. Hashimoto, *Phys. Rev. B* **56**, 11642 (1997).

[16] A. Kumar, S.M. Yusuf, L. Keller, J.V. Yakhmi, J.K. Srivastava, P.L. Paulose, *Phys. Rev. B* **75**, 224419 (2007).

[17] S. Ohkoshi, A. Fujishima, K. Hashimoto, *J. Am. Chem. Soc.* **120**, 5349 (1998).

[18] M. Mizuno, S.I. Ohkoshi, K. Hashimoto, *Adv. Mater.* **12**, 1955 (2000).

[19] M. Yamada, M. Arai, M. Kurihara, M. Sakamoto, M. Miyake, *J. Am. Chem. Soc.* **126**, 9482 (2004).

[20] M. Fitta, H. Prima-Garcia, P. Czaja, T. Korzeniak, M. Krupiński, M. Wojtyniak, M. Bałanda, *RSC Adv.* **7**, 1382 (2017).

[21] D.M. Pajerowski, J.E. Gardner, D.R. Talham, M.W. Meisel, *New J. Chem.* **35**, 1320 (2011).

Proceedings of the Zakopane School of Physics 2023 International Symposium, Zakopane, Poland, May 23–27, 2023

Plasma Treatment as an Unconventional Molecular Magnet Engineering Method

D. Czernia[a,*], P. Konieczny[a], M. Perzanowski[a], and D. Pinkowicz[b]

[a] *Institute of Nuclear Physics Polish Academy of Sciences, Radzikowskiego 152, 31-342 Kraków, Poland*
[b] *Department of Chemistry, Jagiellonian University, Gronostajowa 2, 30-387 Kraków, Poland*

Doi: 10.12693/APhysPolA.145.114 *e-mail: dominik.czernia@ifj.edu.pl

Molecular magnetism aims to design materials with unique properties at the molecular level, focusing on the systematic synthesis of new chemical compounds. In this paper, we propose an alternative route to engineer molecular magnetic materials through plasma irradiation. Our research indicates that the long-range magnetic order temperature in the three-dimensional $\{[Mn^{II}(H_2O)_2]_2[Nb^{IV}(CN)_8]\cdot 4H_2O\}_n$ molecular ferrimagnet increases by 20 K after plasma treatment. The core structure of the compound does not reveal significant changes after plasma processing, as confirmed by the X-ray powder diffraction analysis. The observed results are attributed to the release of crystallized water molecules. The described procedure can serve as a viable approach to altering the magnetic properties of the molecular systems.

topics: molecular magnetism, plasma treatment, octacyanidometalates

1. Introduction

Molecular magnetic materials have emerged at the confluence of chemistry, physics, and materials science, holding promise for a wide range of applications from spintronics or qubits designs [1] to magnetic refrigeration [2] or optically active sensors and switches [3, 4]. The pursuit of molecular magnets stems from the desire to engineer materials at the molecular level, enabling precise control over their magnetic behavior, usually done by selecting proper synthesis components and procedures. The alternative post-synthesis approaches to exploit the potential of molecular magnetic materials include incorporating them into thin films [5] or influencing their properties with ion irradiation [6].

Plasma modification provides another way to manipulate magnetism through surface modification [7, 8] or by introducing specific chemical changes and structural alterations. This can lead to changes in the ferromagnetic interactions [9], magnetic hysteresis loops [10], and blocking temperature [11]. Plasma treatment has been applied in the functionalization [12], polymerization [13], and surface activation and grafting of polymers [14], which share similarities with molecular magnets regarding chemical bonding and composition. Notably, there have been no reports on the effect of plasma irradiation on molecular magnetic materials.

Here, we present the first case of combining plasma modification technique with molecular magnetism in the octacyanidometalate $\{[Mn^{II}(H_2O)_2]_2[Nb^{IV}(CN)_8]\cdot 4H_2O\}_n$ ferrimagnet, representing the well-studied isostructural family of compounds [15–21]. This coordination polymer comprises a three-dimensional network with channels occupied by water molecules coordinated with Mn^{II} and crystallized ones. It is a soft magnet with the long-range magnetic order (LRMO) transition of critical temperature $T_C = 49$ K. This report demonstrates that it is possible to obtain another magnetic phase with a 20 K higher T_C using air-based plasma with little interference in the structure of the chemical compound, i.e., in the original three-dimensional network of magnetic ions linked through cyanide ligands, as observed in the X-ray powder diffraction patterns. This may indicate the loss of water molecules that alter the distance between Mn^{II} and Nb^{IV} and modify antiferromagnetic exchange interactions.

2. Materials and methods

2.1. Sample preparation

The studied $\{[Mn^{II}(H_2O)_2]_2[Nb^{IV}(CN)_8]\cdot 4H_2O\}_n$ coordination polymer (hereafter denoted as $NbMn_2$) was synthesized using $MnCl_2\cdot 4H_2O$ and $K_4[Nb(CN)_8]\cdot 2H_2O$ as per previously published procedures [15]. This led to the formation of dark red crystalline specimens. The powder was ground manually in a mortar to decrease the crystallite size and scattered on a 1×1 cm^2 strip of Scotch tape,

forming a thin sample layer with a mass of about 0.2 mg, guaranteeing a high surface-to-volume ratio for further processing.

The samples were exposed to an air plasma generated by the Harrick plasma cleaner in high-power mode (18 W) for 2 min (denoted as $NbMn_2$-2), 10 min ($NbMn_2$-10), and 15 min ($NbMn_2$-15). The color of $NbMn_2$-10 and $NbMn_2$-15 turned dark brown. Subsequently, an extra layer of Scotch tape was placed on the taped powder samples, which were then folded and encapsulated inside a gelatin capsule with the high vacuum Apiezon M grease for protection against atmospheric air. The infrared thermometer recorded a temperature inside the plasma cleaner not exceeding 75°C.

2.2. Characterization methods

X-ray powder diffraction (XRPD) patterns were obtained by the PANalytical X'Pert Pro instrument with a copper X-ray tube source (Cu $K_{\alpha 1}$, 1.541 Å) in the θ–2θ geometry operating at 40 kV and 30 mA. Data were recorded at room temperature between 5–45° of 2θ. Background correction was applied, and the Scotch tape influence and the anode's characteristic X-ray $K_{\alpha 2}$ were removed.

The magnetic properties were measured using the Quantum Design SQUID MPMS-XL magnetometer. The isothermal magnetization $M(\mu_0 H)$ was obtained with an applied magnetic field of $\mu_0 H = [0, 7]$ T. Static magnetic susceptibility measurements were carried out while cooling in the temperature range of $T = 2.0$–300 K in the applied field of $\mu_0 H_{dc} = 500$ G. The temperature-independent diamagnetic contribution to susceptibility from the sample and its protection was subtracted by fitting the experimental data to the high-temperature range of measured magnetic susceptibility.

3. Results and discussion

3.1. X-ray powder diffraction (XRPD)

Detailed information on the $NbMn_2$ crystallographic structure can be found in the reference article [16]. $NbMn_2$ has a three-dimensional network and crystalizes in the tetragonal space group $I4/m$ with $a = b = 12.080(2)$ Å and $c = 13.375(4)$ Å. The structure consists of alternately linked Nb^{IV} and two Mn^{II} ions through the cyanide ligands (CN). The Nb^{IV} ion is coordinated by eight carbon atoms from CN^-, forming an approximately square antiprismatic coordination. Meanwhile, Mn^{II} is coordinated by two H_2O and four CN^- (by nitrogen) molecules, resulting in a slightly distorted octahedron (Fig. 1). The shortest distance between the Nb^{IV} and Mn^{II} ions is either 5.539 Å or 5.482 Å. Moreover, the network contains four crystallized water molecules.

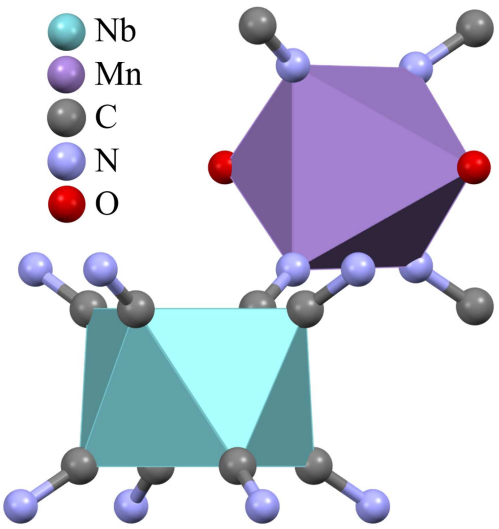

Fig. 1. Representation of Nb^{IV} approximately square antiprism (light blue) and Mn^{II} distorted octahedron (violet) coordinations. The hydrogen atoms are omitted. The complete crystal structure can be found in the reference article [16].

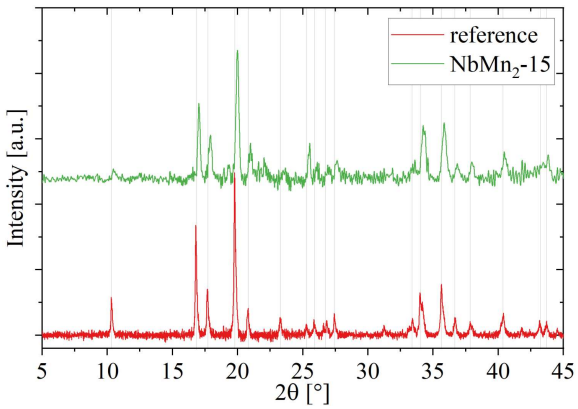

Fig. 2. X-ray powder diffraction patterns for the samples on Scotch tape before (red line; bottom) and after 15 min of plasma treatment, $NbMn_2$-15 (green line; top), measured in the 2θ range of 5–45°. Gray lines indicate the maxima for the reference sample.

X-ray powder diffraction patterns acquired for the reference and $NbMn_2$-15 reveal the presence of the same peaks in analog positions (Fig. 2). Thus, no significant structural variations in $NbMn_2$ occurred throughout the plasma treatment. However, the peaks of the $NbMn_2$-15 are slightly broader and shifted towards higher 2θ, by 0.17° on average. The peak shift indicates crystal lattice shrinkage with the reduction of interplanar spacing by up to 0.029 Å for the (110) index according to Bragg's law. The greater half-widths may result from increased microstrains in the crystal lattice or crystallite size reduction.

3.2. Magnetic properties

The magnetic properties of $NbMn_2$ have been investigated in previous studies [16], revealing LRMO below $T_C = 49$ K and the absence of hysteresis loop down to $T = 2.0$ K. The magnetization saturation reaches $9\mu_B$/mol, which corresponds to the anticipated value for the antiparallel configuration of Nb^{IV} ($S = 1/2$; $g = 2.0$) and Mn^{II} ($S = 5/2$; $g = 2.0$) ions within the $NbMn_2$ unit. The mean-field approximation predicts the antiferromagnetic superexchange coupling constant of $J_{NbMn} = -15.44(7)$ K between Nb^{IV} and Mn^{II} ions, as well as an antiferromagnetic interaction within the Mn sublattice that is at least an order of magnitude smaller [15].

The isothermal magnetization field dependence for studied samples measured at $T = 2.0$ K from $\mu_0 H = 0$ to 7 T is shown in Fig. 3. The magnetization curves all overlap above approximately $\mu_0 H = 2$ T at the expected level for isotropic ions of $9\mu_B$/mol. However, the magnetization saturates slightly slower for $NbMn_2$-10 and visibly slower for $NbMn_2$-15, which indicates a weak modification of the magnetization process caused by incorporating plasma-induced defects leading to the pinning of domain walls.

More prominent changes can be seen in the magnetic susceptibility χ measured in $\mu_0 H = 500$ G from 300 to 2 K, as illustrated in Fig. 4. The results are presented in the form of χT product showing the maximum at $T_{max} \approx 40$ K for the reference, $NbMn_2$-2, and $NbMn_2$-10. For the $NbMn_2$-15, it was $T_{max} \approx 56$ K. The gradual shift in T_{max} can be observed in χT for $NbMn_2$-10 as an obvious two-peak susceptibility composition, indicating the emergence of a second magnetic phase with higher T_C.

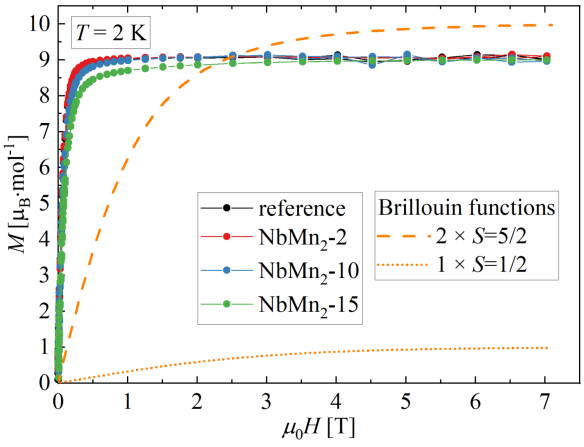

Fig. 3. The isothermal magnetization measured at $T = 2.0$ K in the applied magnetic fields $\mu_0 H = 0$–7 T of the $NbMn_2$ samples. The orange lines represent the Brillouin functions corresponding to two spins $S = 5/2$ (dashed) and one spin $S = 1/2$ (dotted), assuming $g = 2.0$ in both cases.

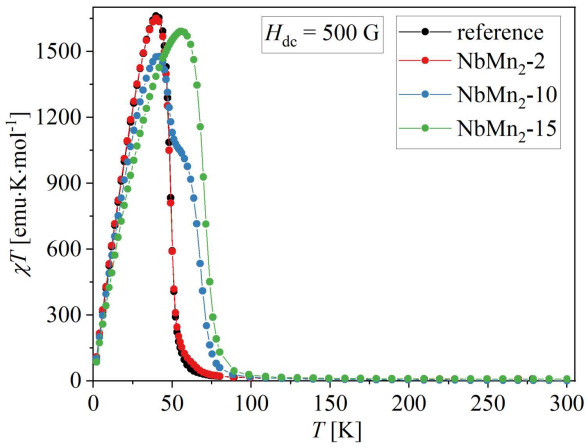

Fig. 4. Temperature dependence of the χT product for $NbMn_2$ measured in the magnetic field of $\mu_0 H_{dc} = 500$ G. Lines are a guide for the eye.

The T_C value was estimated from the minima of the $\chi T(T)$ first derivative:

- 49 K each for the reference and $NbMn_2$-2;
- (two minima) 48 K and 67.5 K for $NbMn_2$-10;
- 69.5 K for $NbMn_2$-15.

The observed outcomes can be explained by the water molecules that escape from the three-dimensional network channels as a consequence of plasma–lattice interaction, similar to the desorption studies of other Nb/Mn-based octacyanidometalates [22–25]. Removing water molecules leads to the crystal lattice shrinkage, as seen in XRPD, thus decreasing the Mn^{II}–Nb^{IV} distance and enhancing exchange coupling interactions.

4. Conclusions

Our study presents the first example of applying plasma modification to molecular magnetic materials to tailor their selected properties. We investigated the impact of plasma treatment on the three-dimensional $NbMn_2$ molecular ferrimagnet. A second magnetic phase emerges after plasma treatment with a critical temperature T_C increased by 20.5 K from its initial value of $T_C = 49$ K, reaching $T_C = 69.5$ K. In contrast, the magnetization process $T = 2.0$ K undergoes only slight modification. The measurements of XRPD indicate only subtle modifications of the crystal structure. Additionally, the process of creating this new phase is gradual and can be regulated through plasma irradiation time.

Further studies are needed to explore the nature of the modification in magnetic properties. High temperature and ultraviolet light generated in plasma, as well as desorption of crystallized and coordinated water, are potential factors contributing to the observed results. In particular, combining the

dynamic vapor sorption (DVS) technique with magnetometry will allow assessing whether the desorption of water molecules induces similar changes in magnetic properties as after plasma treatment. On the other hand, applying the mean-field approximation model [15] may give insights into the nature of magnetic interactions before and after plasma processing, explaining the mechanism behind the modification of the critical temperature.

Acknowledgments

This work was supported by the Polish Minister of Education and Science (G. No. DI2017 006047).

References

[1] E. Coronado, *Nat. Rev. Mater.* **5**, 87 (2020).

[2] P. Konieczny, W. Sas, D. Czernia, A. Pacanowska, M. Fitta, R. Pełka, *Dalt. Trans.* **51**, 12762 (2022).

[3] M. Magott, D. Pinkowicz, *Chem. Commun.* **57**, 9926 (2021).

[4] K. Rogacz, M. Brzozowska, S. Baś, K. Kurpiewska, D. Pinkowicz, *Inorg. Chem.* **61**, 16295 (2022).

[5] A. Pacanowska, M. Fitta, M. Kozieł, B. Nowicka, *Adv. Mater. Interfaces* **10**, 2201834 (2023).

[6] D. Czernia, P. Konieczny, E. Juszyńska-Gałązka, M. Perzanowski, J. Lekki, A.B. González Guillén, W. Łasocha, *Sci. Rep.* **13**, 14032 (2023).

[7] M. Krupinski, A. Zarzycki, Y. Zabila, M. Marszałek, *Materials* **13**, 3246 (2020).

[8] M. Krupinski, D. Mitin, A. Zarzycki, A. Szkudlarek, M. Giersig, M. Albrecht, M. Marszałek, *Nanotechnology* **28**, 085302 (2017).

[9] B. Wang, D. Zhang, H. Wang, H. Zhao, R. Liu, Q. Li, S. Zhou, J. Du, Q. Xu, *AIP Adv.* **10**, 015243 (2020).

[10] D. Li, L.M. Xu, S.W. Li, X. Zhou, *Chinese J. Chem. Phys.* **30**, 457 (2017).

[11] H.J. Kim, H. Choi, *J. Magn. Magn. Mater.* **484**, 14 (2019).

[12] R. Laurano, M. Boffito, A. Torchio, C. Cassino, V. Chiono, G. Ciardelli, *Polymers.* **11**, 2109 (2019).

[13] L. Wang, Y. Zhu, H. Liu, J. Gong, W. Wang, S. Guo, Y. Yu, H. Peng, Y. Liao, *ACS Appl. Mater. Interfaces.* **11**, 35270 (2019).

[14] F. Khelifa, S. Ershov, Y. Habibi, R. Snyders, P. Dubois, *Chem. Rev.* **116**, 3975 (2016).

[15] P. Konieczny, R. Pełka, T. Wasiutyński, M. Oszajca, B. Sieklucka, D. Pinkowicz, *Dalt. Trans.* **47**, 11438 (2018).

[16] J.M. Herrera, P. Franz, R. Podgajny et al., *Comptes Rendus Chim.* **11**, 1192 (2008).

[17] S. Willemin, J. Larionova, R. Clérac, B. Donnadieu, B. Henner, X.F. Le Goff, C. Guérin, *Eur. J. Inorg. Chem.* **2003**, 1866 (2003).

[18] M. Fitta, R. Pełka, W. Sas, D. Pinkowicz, B. Sieklucka, *RSC Adv.* **8**, 14640 (2018).

[19] D. Pinkowicz, R. Pełka, O. Drath, W. Nitek, M. Bałanda, A.M. Majcher, G. Poneti, B. Sieklucka, *Inorg. Chem.* **49**, 7565 (2010).

[20] M. Fitta, R. Pełka, P. Konieczny, M. Bałanda, *Crystals* **9**, 9 (2019).

[21] M. Fitta, M. Bałanda, M. Mihalik, R. Pełka, D. Pinkowicz, B. Sieklucka, M. Zentkova, *J. Phys. Condens. Matter.* **24**, 506002 (2012).

[22] D. Pinkowicz, R. Podgajny, M. Bałanda, M. Makarewicz, B. Gaweł, W. Łasocha, B. Sieklucka, *Inorg. Chem.* **47**, 9745 (2008).

[23] M. Fitta, R. Pełka, M. Gajewski, M. Mihalik, M. Zentkova, D. Pinkowicz, B. Sieklucka, M. Bałanda, *J. Magn. Magn. Mater.* **396**, 1 (2015).

[24] D. Pinkowicz, R. Podgajny, B. Gaweł, W. Nitek, W. Łasocha, M. Oszajca, M. Czapla, M. Makarewicz, M. Bałanda, B. Sieklucka, *Angew. Chemie Int. Ed.* **50**, 3973 (2011).

[25] M. Fitta, R. Pełka, M. Bałanda, M. Czapla, M. Mihalik, D. Pinkowicz, B. Sieklucka, T. Wasiutyński, M. Zentkova, *Eur. J. Inorg. Chem.* **2012**, 3830 (2012).

Proceedings of the Zakopane School of Physics 2023 International Symposium, Zakopane, Poland, May 23–27, 2023

Update on MAC End-Station at ELI Beamlines Facility

E. Klimešová[a,*], A.H. Roos[a], Z. Hoque[a], N. Smijesh[a], R.J. Squibb[b], H. Coudert-Alteirac[b], R. Feifel[b], J. Andreasson[a] and M. Krikunova[a,c]

[a] *ELI Beamlines facility, The Extreme Light Infrastructure ERIC, Za Radnicí 835, 252 41 Dolní Břežany, Czech Republic*
[b] *Attohallen Facility, University of Gothenburg, Department of Physics, Origovgen 6B, SE-412 58 Gothenburg, Sweden*
[c] *Technical University of Applied Sciences, Hochschulring 1, 15745 Wildau, Germany*

Doi: 10.12693/APhysPolA.145.118 *e-mail: eva.klimesova@eli-beams.eu

The MAC end-station at the ELI Beamlines facility is a multipurpose user's station for atomic, molecular, and optical sciences and coherent diffractive imaging. The technical design of the station, the available instruments, and an overview of the whole beamline have been published in *Eur. Phys. J. Spec. Top.* **230**, 4183 (2021). Here, we address ongoing upgrades of the MAC end-station that will provide users with advanced capabilities for beam manipulation and electron/ion detection. The upgrades include (i) the installation of a beam preparation chamber in front of the MAC chamber, (ii) a magnetic bottle electron spectrometer with high collection and detection efficiency and high energy resolution, and (iii) an event-driven TPX3CAM detector for velocity map imaging spectrometer, which provides both spatial and temporal information for each pixel. We present results from the first commissioning measurements with these instruments, confirming their performance for state-of-the-art experiments in atomic, molecular, and optical sciences.

topics: atomic and molecular sciences, lasers, electron and ion spectroscopy

1. Introduction

High harmonic generation (HHG) is a well-established technique to produce coherent extreme ultraviolet (XUV) radiation with excellent properties, such as high temporal and spatial coherence, femtosecond pulse duration, high intensity, synchronization with other laser beams, and the possibility to select a single harmonic by a monochromator [1–4]. The applications of femtosecond high harmonics include time-resolved studies of chemical processes [5–7], tracking and controlling ultrafast electron dynamics in atoms [8, 9], probing chiral molecules in the gas phase [10], or investigations of transient phenomena in nanoscale quantum systems [11–15].

The HHG beamline at ELI Beamlines facility near Prague, Czech Republic [4, 14], is primarily driven by an in-house L1 laser (central wavelength 830 nm, pulse duration 15 fs, energy per pulse up to 100 mJ, repetition rate 1 kHz [16]) and provides XUV pulses in the photon energy range of 20–100 eV for user experiments in different research areas. We address the user end-station MAC at the HHG beamline — a multipurpose station for atomic, molecular, and optical sciences (AMO) and coherent diffractive imaging (CDI) [17]. At MAC, the HHG beam synchronized with an auxiliary laser beam is used to unveil ultrafast electron and ion dynamics in low-density targets, such as atoms [9, 18], molecules, helium nanodroplets [14, 15], or nanoparticles [19]. Moreover, CDI studies on solid targets are possible at MAC [20]. The technical design of the MAC station, available beams, sample delivery systems, and diagnostics have been described in detail in [17].

To advance experiments at the MAC end-station and provide the user community with additional capabilities, several upgrades are currently underway. First, a new beam preparation chamber (so-called B4MAC) will be installed to offer more complex options for the manipulation and focusing of the beams. A magnetic bottle electron spectrometer (MBES), currently being commissioned, will provide high collection and detection efficiency of ions and electrons, high energy resolution, and an option for coincidence electron–ion detection. Finally, the current velocity map imaging (VMI) spectrometer has been upgraded with a TPX3CAM detector to enable fast and efficient spatial and temporal signal acquisition. In this contribution, we describe these upgrades, show the results of the first measurements, and discuss the user-access policies at the ELI Beamlines facility.

2. MAC end-station upgrades

An overview of the MAC end-station with different diagnostics instruments is shown in Fig. 1. The large rectangular chamber on the left is the B4MAC chamber for focusing and manipulation of multiple beams. The diagnostic instruments on MAC are MBES, VMI, and XUV spectrometers. Apparatuses for sample delivery (molecular beam or cluster source) are not shown; they are normally installed in a horizontal orientation. The setup is modular and can be adjusted for a specific user experiment.

2.1. Beam preparation chamber B4MAC

For time-resolved experiments at the MAC end-station, an XUV beam is overlapped with a synchronized auxiliary beam in MAC. The auxiliary beam can be the fundamental with a wavelength of around 800 nm or its second or third harmonic. In the current setup, XUV beam forward-focusing with an ellipsoidal mirror [9] and XUV beam back-focusing with a spherical mirror [14] have both been implemented. Pump–probe experiments have been performed with the forward-focusing setup. CDI has been performed inside the MAC chamber.

To offer more options and more space for beam manipulation and focusing, a B4MAC beam preparation chamber with a decoupled optical breadboard will be installed (Fig. 2). Focusing geometries possible with B4MAC include:

1. XUV forward-focusing with ellipsoidal mirror, typically after the beam passes the monochromator. XUV focal spot size is around 35×50 μm full width at half maximum. Auxiliary beam(s) can be coupled collinearly or at a small angle with the XUV beam.
2. XUV back-focusing with off-axis parabola; focal spot size of a few micrometers. This geometry is foreseen to be utilized mainly for CDI on solid targets in the B4MAC chamber, providing enough space for CDI setup with diagnostics.
3. Two XUV beam experiments (anticipated in the future).
4. XUV back-focusing with a spherical mirror in MAC (not shown in Fig. 2). Focal spot size can be as small as ~ 1 μm. In this case, the multilayer spherical mirror is placed inside the MAC chamber. Different coatings can be used depending on the users' needs.

Moreover, thanks to many useful ports on the B4MAC chamber and a large optical breadboard decoupled from the vacuum system, custom user-specific geometries can be implemented there.

2.2. Magnetic bottle electron spectrometer

To offer high electron energy resolution and high collection efficiency, an MBES for the MAC end-station is now being commissioned. It has been developed and commissioned in collaboration with the group of Raimund Feifel, University of Gothenburg, Sweden, and is based on the design presented in [21]. The main components of the MBES are a strong permanent magnet placed close to the interaction region, followed by a flight tube and a microchannel plate (MCP) detector (Fig. 3). The permanent magnet creates a strong magnetic field that collects basically all electrons emitted in the 4π solid angle.

The electron flight tube is surrounded by a solenoid to guide electrons on their way to the MCP detector. The length of the flight tube of 2 m ensures a high spectral resolution. An optional electrostatic lens assembly can be attached to the flight tube for high-resolution ion detection. The MCP detector (Hamamatsu, model F9892-31) has an open area ratio of more than 90%, leading to a large detection efficiency.

An example photoelectron spectrum from the commissioning experiments in Gothenburg is shown in Fig. 4. In this measurement, atomic Xe was ionized by a laser with a photon energy of 4.8 eV (4th harmonic of 1030 nm laser), 160 fs pulse duration, and a repetition rate of 3 kHz. The two photoelectron lines originate in 3-photon ionization of the Xe atom from its $5p_{1/2}$ and $5p_{3/2}$ states, respectively. The measured spacing between the lines corresponds to the spin–orbit splitting of the Xe $5p$ shell. From the full width at half maximum of the $5p_{3/2}$ line, one can infer a spectral resolution of about $E/\Delta E = 60$ in this photoelectron energy range.

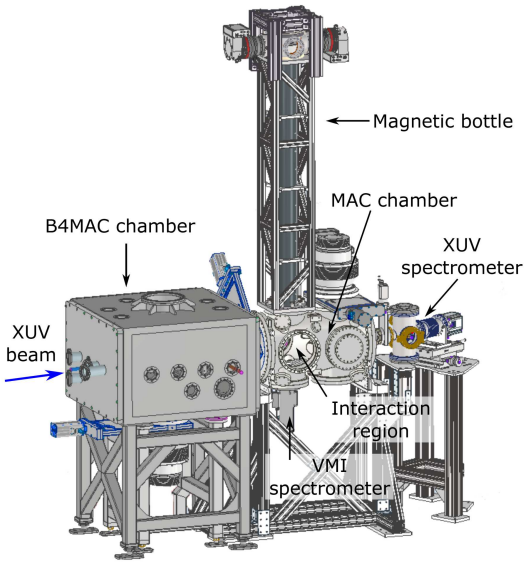

Fig. 1. Schematic view of the MAC end-station with different diagnostics instruments. Sample delivery systems are not shown.

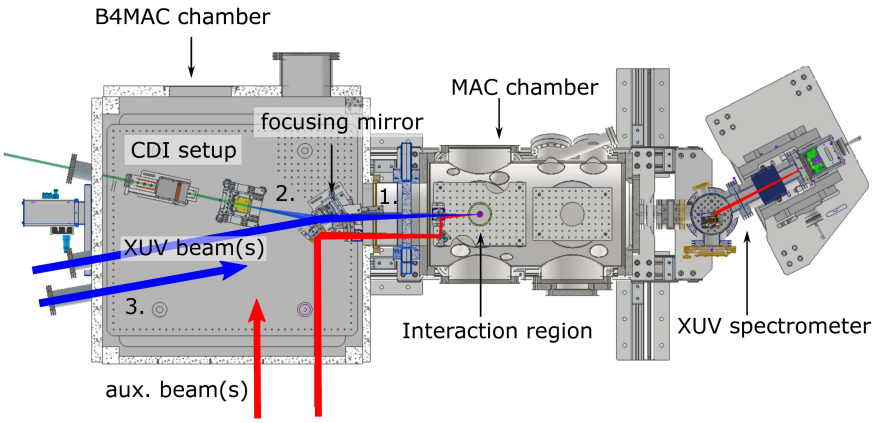

Fig. 2. Schematics of the B4MAC and MAC chambers with the XUV and auxiliary beams. For a description of different geometries (1–3), see the text.

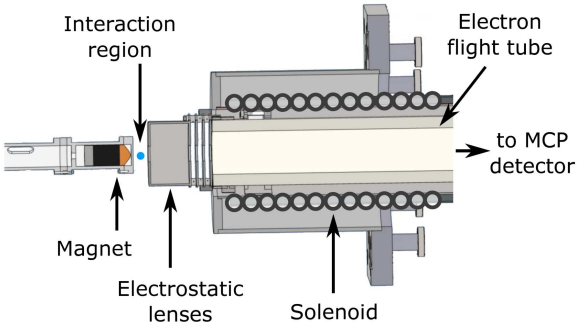

Fig. 3. A schematic drawing of the magnetic bottle electron spectrometer in the electron-only configuration. Electrons are confined by the combined magnetic field of the permanent magnet and the solenoid and fly through the flight tube to the MCP detector.

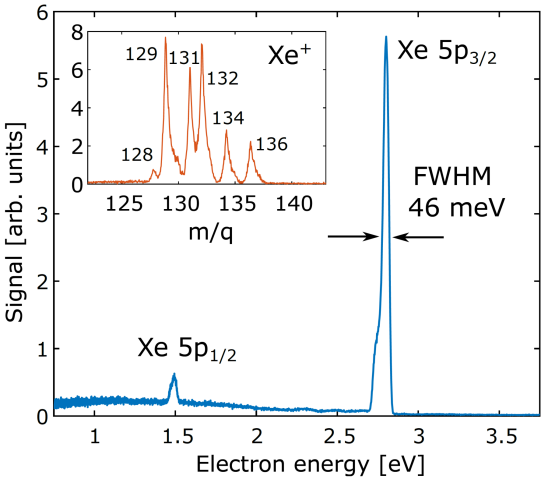

Fig. 4. Photoelectron spectrum measured with magnetic bottle electron spectrometer. Xe atoms were ionized with an intense laser (photon energy 4.8 eV, repetition rate 3 kHz, pulse duration 160 fs). Photoelectrons created by 3-photon ionization of Xe $5p_{1/2}$ and $5p_{3/2}$ states are indicated. Inset shows Xe^+ ion mass spectrum detected in coincidence with electrons. Individual Xe isotopes are indicated.

MBES can be operated in two primary configurations, namely electron detection only, or electron–ion coincidence. In the latter setup, electrodes for ions and an ion detector are added to the instrument [22]. Pulsed voltages are used to extract ions after the electrons leave the interaction region (i.e., around 100 ns after ionization). Xe ions detected in coincidence with electrons are shown in the inset of Fig. 4. Six Xe isotopes are resolved. The seventh Xe isotope with a mass of 130 amu with an abundance of 4% is in the tail of 129 amu isotope. The MBES will be installed on the MAC chamber in a vertical orientation and will provide an efficient tool for electron spectroscopy and simultaneous electron and ion detection.

2.3. VMI spectrometer with TPX3CAM

The VMI spectrometer at the MAC end-station (Eppink and Parker design [23], manufactured by Photek) has been originally equipped with a CMOS camera (IDS, 166 frames per second). While providing high collection efficiency and good energy and angular resolution, the data acquisition speed is limited by the camera readout, and gating is needed to detect specific ion species. An upgrade of the VMI consists of replacing the CMOS camera with an event-driven TPX3CAM detector (Amsterdam Scientific Instruments) [24, 25]. TPX3CAM is based on Timepix3 chip technology, where each hybrid pixel of the detector records both the intensity (related to time-over-threshold (ToT)) and time-of-arrival (ToA) of each event.

Employing TPX3CAM, one can simultaneously detect the time-of-flight spectrum (mass spectrum) and a velocity map image of each ion species. Thus, images of all ion species can be

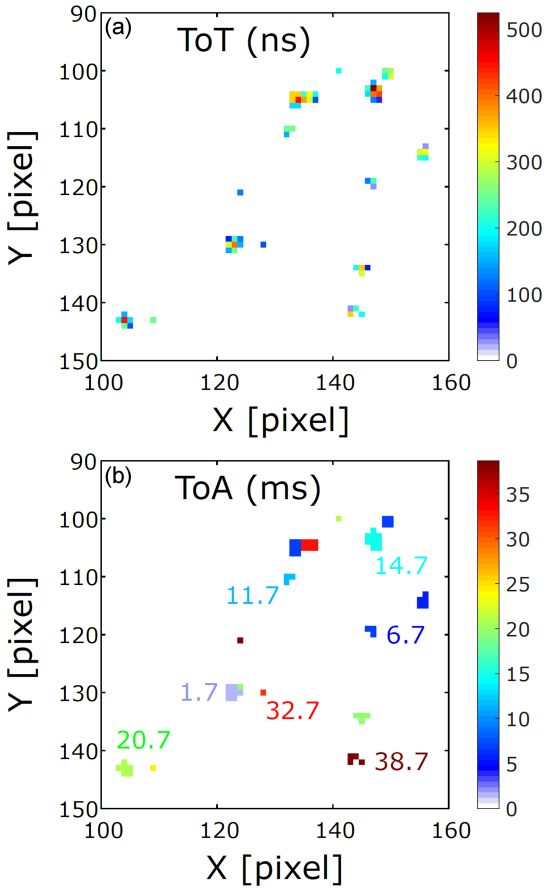

Fig. 5. Example of TPX3CAM pixel data. Electrons emitted from background gas in the MAC chamber ionized with an intense NIR beam at a 1 kHz repetition rate were detected. (a) Zoom on a ~ 40 ms measurement displaying the ToT of each pixel. (b) Same image as in (a) but showing ToA. Times of arrivals of several hits are indicated next to them.

recorded simultaneously, allowing for coincidence or covariance analysis to give complete information on the fragmentation pathways of the system under study [26, 27]. The ToA time bin of 1.56 ns is sufficiently small to resolve ion time-of-flight well, but becomes limiting for 3D electron detection.

An example measurement with TPX3CAM is shown in Fig. 5. Background gas in the MAC chamber was ionized by an intense near-infrared (NIR) laser beam at a 1 kHz repetition rate, and electrons were detected by the VMI spectrometer with TPX3CAM. TPX3CAM readout is event-based, so only hits arriving at the detector are registered, resulting in efficient data storage. For each event, both the ToT (proportional to the intensity, Fig. 5a) and ToA (Fig. 5b) are registered. One can see that the arrivals of different hits are spaced by 1 ms, corresponding to electrons created by different laser shots at the 1 kHz repetition rate. This measurement confirms the operation of TPX3CAM with the VMI spectrometer, detecting both spatial and temporal information and offering fast and efficient data acquisition.

3. User access

The MAC end-station is a part of the ELI Beamlines facility [28], operated within the Extreme Light Infrastructure ERIC [29]. The ELI Beamlines facility is a user center providing access to high-power, high-repetition-rate laser systems and secondary sources. Access to the ELI Beamlines facility is free, competitive, and open to the international user community. Proposals are evaluated by international peer-review panels composed of independent peer reviewers. To find more information and apply for beamtime, visit the ELI ERIC user portal [29].

4. Conclusions

The MAC end-station is a multipurpose, modular instrument for a wide user community in the field of AMO sciences and CDI. It is operational and open for user access. Several experiments at MAC have already revealed intricate fast processes in atoms [9, 18], molecules, helium nanodroplets [14, 15], and nanoparticles [19]. We have presented ongoing upgrades of the MAC end-station, i.e., a B4MAC chamber for complex beam manipulation, an MBES for efficient and well-resolved electron detection, and a TPX3CAM on VMI spectrometer for simultaneous time and position data acquisition. The presented results demonstrate the functionality of these instruments, offering state-of-the-art technology for complex investigations.

Acknowledgments

The authors thank the staff of the ELI Beamlines Facility, a European user facility operated by the Extreme Light Infrastructure ERIC, for their support and assistance. This work was supported by the project "Advanced research using high-intensity laser produced photons and particles" (ADONIS) (CZ.02.1.01/0.0/0.0/16 019/0000789) and "Structural dynamics of biomolecular systems" (ELIBIO) (CZ.02.1.01/0.0/0.0/15 003/0000447), both from the European Regional Development Fund and the Ministry of Education, Youth and Sports. This publication is also based upon the work of COST Action CA21101 "Confined molecular systems: From a new generation of materials to the stars" (COSY) supported by COST (European Cooperation in Science and Technology). The work relating to MBES development and commissioning has been financially supported by the Swedish Research Council (VR), the Olle Engkvist Foundation, and the Knut and Alice Wallenberg Foundation, Sweden.

References

[1] F. Calegari, G. Sansone, S. Stagira, C. Vozzi, M. Nisoli, *J. Phys. B At. Mol. Opt. Phys.* **49**, 062001 (2016).

[2] L. Young, K. Ueda, M. Gühr et al., *J. Phys. B At. Mol. Opt. Phys.* **51**, 032003 (2018).

[3] M. Reduzzi, P. Carpeggiani, S. Kühn et al., *J. Electron Spectrosc. Relat. Phenom.* **204**, 257 (2015).

[4] O. Hort, M. Albrecht, V.E. Nefedova et al., *Opt. Express* **27**, 8871 (2019).

[5] A.D. Smith, E.M. Warne, D. Bellshaw et al., *Phys. Rev. Lett.* **120**, 183003 2018).

[6] A. von Conta, A. Tehlar, A. Schletter, Y. Arasaki, K. Takatsuka, H.J. Wörner, *Nat. Commun.* **9**, 3162 (2018).

[7] M.S. Schuurman, V. Blanchet, *Phys. Chem. Chem. Phys.* **24**, 20012 (2022).

[8] H. Geiseler, H. Rottke, N. Zhavoronkov, W. Sandner, *Phys. Rev. Lett.* **108**, 123601 (2012).

[9] A.H. Roos, Z. Hoque, E. Klimešová et al. *New J. Phys.* **25**, 013038 (2023).

[10] V. Svoboda, N. Bhargava Ram, D. Baykusheva, D. Zindel, M.D.J. Waters, B. Spenger, M. Ochsner, H. Herburger, J. Stohner, H.J. Wörner *Sci. Adv.* **8**, eabq2811 (2022).

[11] M. Mudrich, F. Stienkemeier, *Int. Rev. Phys. Chem.* **33**, 301 (2014).

[12] M.P. Ziemkiewicz, D.M. Neumark, O. Gessner, *Int. Rev. Phys. Chem.* **34**, 239 (2015).

[13] B. Schütte, M. Arbeiter, A. Mermillod-Blondin, M.J.J. Vrakking, A. Rouzée, T. Fennel, *Phys. Rev. Lett.* **116**, 033001 (2016).

[14] L. Jurkovičová, L.B. Ltaief, A.H. Roos et al., *Commun. Phys.* **7**, 26 (2024).

[15] C. Medina, A.Ø. Lægdsmand, L.B. Ltaief et al., *New J. Phys.* **25**, 053030 (2023).

[16] R. Antipenkov, E. Erdman, J. Novák et al., in: *Optica Advanced Photonics Congress 2022*, Optica Publishing Group, 2022, p. AW2A.4.

[17] E. Klimešová, O. Kulyk, Z. Hoque et al., *Eur. Phys. J. Spec. Top.* **230**, 4183 (2021).

[18] E. Klimešová, O. Kulyk, Y. Gu, L. Dittrich, G. Korn, J. Hajdu, M. Krikunva, J. Andreasson, *Sci. Rep.* **9**, 8851 (2019).

[19] E. Klimešová, O. Kulyk, L. Dittrich, J. Andreasson, M. Krikunova, *Phys. Rev. A* **104**, L061101 (2021).

[20] J. Nejdl, U. Chaulagain, O. Hort et al., *Proc. SPIE* **11886**, 1188608 (2021).

[21] J.H.D. Eland, O. Vieuxmaire, T. Kinugawa, P. Lablanquie, R.I. Hall, F. Penent, *Phys. Rev. Lett.* **90**, 053003 (2003).

[22] J.H.D. Eland, R. Feifel, *Chem. Phys.* **327**, 85 (2006).

[23] A.T.J.B. Eppink, D.H. Parker, *Rev. Sci. Instrum.* **68**, 3477 (1997).

[24] A. Zhao, M. van Beuzekom, B. Bouwens et al., *Rev. Sci. Instrum.* **88**, 113104 (2017).

[25] H. Bromberger, Ch. Passow, D. Pennicard et al., *J. Phys. B At. Mol. Opt. Phys.* **55**, 144001 (2022).

[26] J. Lee, H. Köckert, D. Heathcote, D. Popat, R. Chapman, G. Karras, P. Majchrzak, E. Springate, C. Vallance, *Commun. Chem.* **3**, 72 (2020).

[27] C. Schouder, A.S. Chatterley, M. Johny, F. Hübschmann, A.F. Al-Refaie, F. Calvo, J. Küpper, H. Stapelfeldt, *J. Phys. B At. Mol. Opt. Phys.* **54**, 184001 (2021).

[28] ELI Beamlines Facility website.

[29] Extreme Light Infrastructure ERIC website.

Proceedings of the Zakopane School of Physics 2023 International Symposium, Zakopane, Poland, May 23–27, 2023

Nuclear Fragmentation Cross-Section Measurements with the FOOT Experiment

G. Ubaldi[a,b,*]

[a] *University of Bologna, Department of Physics and Astrophysics, via Irnerio 46, 40126 Bologna, Italy*
[b] *Istituto Nazionale di Fisica Nucleare (INFN) — Section of Bologna, Viale Carlo Berti Pichat 6/2, 40127 Bologna, Italy*

Doi: 10.12693/APhysPolA.145.123 *e-mail: gubaldi@bo.infn.it

The main goals of the FragmentatiOn Of Target experiment are the measurements of double-differential fragmentation cross-sections of light particles ($Z < 10$) in the energy range between 100–800 MeV/u, which is of interest for hadron therapy and space radioprotection applications. The results will fill the gap in experimental data in this range, which is important for improving the treatment planning systems in particle therapy and for enhancing the reliability of risk-assessment models for space radioprotection. Two different setups were designed for this scope, and data have already been taken in several campaigns. In this paper, an overview of the apparatus is described, focusing on the preliminary results of cross-section measurements obtained with a ^{16}O beam at the GSI facility.

topics: FOOT (FragmentatiOn Of Target), nuclear fragmentations, cross sections measurements

1. Introduction

Particle therapy is a medical treatment based on the use of charged particle beams (usually protons and carbon ions) to treat deep-seated tumors in patients. According to how they interact with matter, the dose release is low and almost constant in the entrance channel and increases sharply near the end of the path where the tumor is situated, sparing the surrounding healthy tissues and organs. This represents the main advantage in comparison with conventional *radiotherapy*, and due to its effectiveness, *particle therapy* is becoming an important technique with an increasing number of treatment centers all around the world.

However, at the energy of clinical treatment (100–400 MeV/u), the incoming beam produces nuclear interactions while crossing the patient, generating fragments that change the biological dose. Specifically, short-range target fragments increase the local dose in the entrance channel, while projectile fragments have a range long enough to go beyond the tumor region. As a consequence, the energy deposition outside the tumor is higher than expected, causing collateral damage. Nuclear fragmentation cross-section measurements are then fundamental for a deep knowledge of these processes, which have to be taken into account when preparing particle therapy treatment plans.

Nuclear fragmentation has to be inspected even in the context of space radioprotection. The main sources of radiation in space are cosmic rays originating from astrophysical environments inside and outside the galaxy and particles generated by local outbursts on the Sun's surface. They are mainly protons and ^{4}He ions with a large energy spread, having a maximum of around 100–800 MeV/u, which can interact with astronauts and equipment. Long-term human missions in deep space are planned in the coming years by several space agencies, including ESA and NASA. It is then fundamental to preserve the astronauts' health and to prevent electronic damage from exposure to cosmic radiation, and in this scenario, the design and optimization of the spacecraft shielding require detailed knowledge of fragmentation processes.

At present, there is a lack of experimental data about nuclear fragmentation for light fragments (Z<10) in the energy range of 100–800 MeV/u, i.e., typical energies used in particle therapy [1] and relevant for space radioprotection [2]. To fill this data gap, the FOOT (FragmentatiOn Of Target) experiment [3] has been conceived with the main aim of measuring differential nuclear cross-sections of both target and projectile fragments in an extensive set of measurement campaigns using several beams, such as H, He, C, and O.

2. The FOOT experiment

The main aim of the FOOT experiment is to measure the double-differential cross-section in angle and energy of fragmentation reactions with

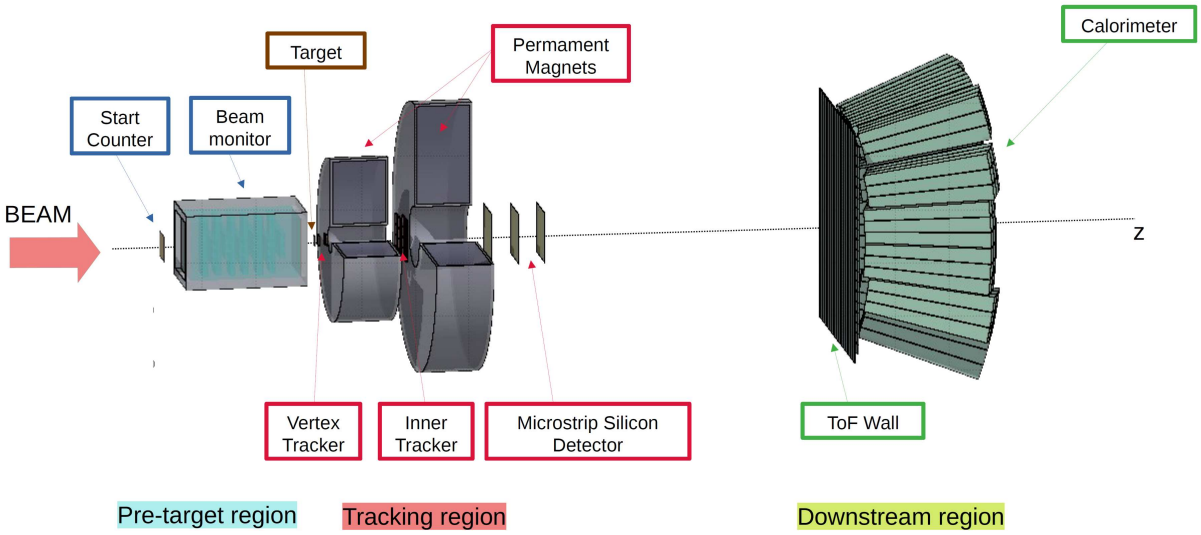

Fig. 1. Schematic representation of the FOOT electronic setup, organized in three main regions.

a resolution of 5% in both direct and inverse kinematics. It is a fixed target experiment in which beams of ions (such as ^{4}He, ^{12}C, ^{16}O) are shot against a target containing H, C, or O to simulate what happens during the beam–human interaction.

An important requirement of the FOOT experiment is its portability, which allows for performing data taking in experimental rooms in research centers scattered in different places. For this reason, the sizes and weights of detectors are important criteria to consider in the experimental design.

In order to obtain cross-section measurements, particle identification with accurate precision is required and can be obtained through the measurements of the kinematic characteristics of the particles. To reach this goal, the experiment consists of two setups with complementary purposes: one based on electronic detectors and one based on nuclear emulsions.

The FOOT electronic setup (ES) is optimized for particle identification of fragments with $Z \geq 3$ and an angular acceptance of $\pm 10^{\circ}$ with respect to the beam axis. A schematic representation is shown in Fig. 1. The ES is made of several subdetectors designed for charge and isotopic reconstruction of the fragments, organized into three main sections. The upstream region is suited to retrieve the features of the primary beam before impinging on the target. The *start counter* is a thin squared foil of plastic scintillator with an active surface of 5×5 cm^2 coupled with silicon photomultipliers (SiPMs) for light collection. It provides the trigger signal for the acquisition and start time for the time-of-flight (ToF) measurement of the particle, with a time resolution of the order of 50 ps. The *beam monitor* is a drift chamber filled with an 80/20% gas mixture of Ar/CO_2, made of 12 wire layers with three cells each, with a transversal shape of 16×10 mm^2. The aim is to measure the direction and the interaction point of the incoming beam and to discard pre-target fragmentation, with a spatial resolution of 100 μm.

After the target, there is the magnetic spectrometer made of silicon detectors interleaved by permanent magnets for track reconstruction. The *vertex detector* is a pixel silicon detector placed behind the target to reconstruct the origin point of the fragment. It consists of four layers of MIMOSA-28 sensors, each made of a matrix of 928×960 pixels of 20.7 μm pitch and 50 μm of thickness. The overall spatial resolution is of the order of 5 μm. In order to provide the tracking of the fragments among the magnets, the *inner tracker* is placed, made of two layers of 16 MIMOSA-28 sensors each. The third tracking station is given by the *microstrip detector* consisting of 3 planes of two perpendicular single-sided silicon detectors, each with an active area of 9.6×9.3 cm^2. The spatial resolution is about 40 μm. The two magnets with a diameter of 5 cm and 10.6 cm, respectively, are designed in Halbach configuration, generating a magnetic field B of a mean value of 1 T. They bend the trajectory of the charged fragments produced in the target to enable momentum measurement.

The last part of the electronic setup is the downstream region, at least 1 m away from the target, for identification of the fragments. In particular, the ToF *wall detector* is composed of two orthogonal layers of 20 plastic scintillator bars each, with an active area of 40×40 cm^2. Every bar is 0.3 cm thick and coupled at each edge to 4 SiPM, allowing the measurement of the energy loss $\mathrm{d}E/\mathrm{d}x$ needed for the charge reconstruction, the final time information for the ToF measurement, and the hit position for the track reconstruction. The time resolution is of the order of 100 ps, and the energy loss one is better than 5%, while the position precision is better than 8 mm. The calorimeter is the last detector

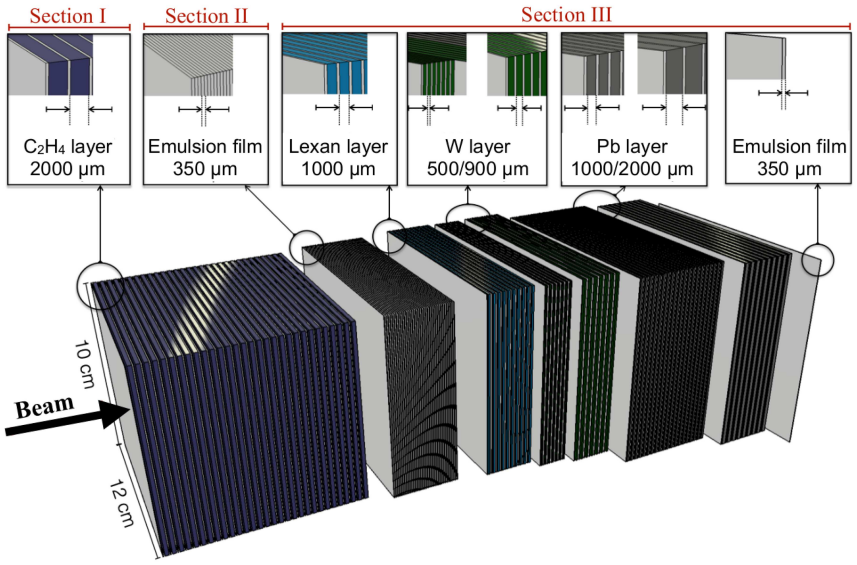

Fig. 2. Schematic representation of the FOOT emulsion cloud chamber, settled in three main sections.

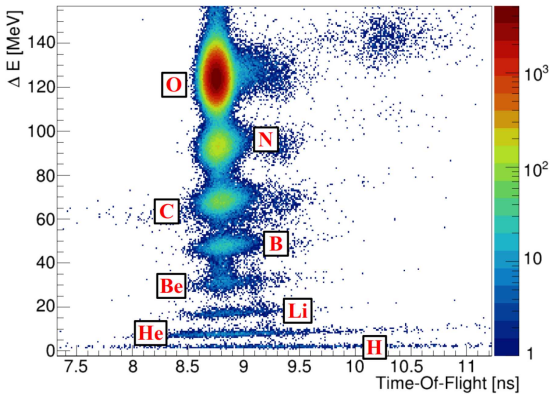

Fig. 3. Charge identification of fragments generated by a 400 MeV/u ^{16}O beam impinging on a 5 mm C target at GSI in 2021 as a relation between energy loss and ToF in the ToF-wall detector.

of the setup with the aim of measuring the kinetic energy of the fragment. It is made of 320 $Bi_4Ge_3O_{12}$ (BGO) crystals with a length of 24 cm and front and back sizes of 2×2 cm^2 and 3×3 cm^2, respectively. Every crystal is coupled to a matrix of 25 SiPM for light detection.

According to how the electronic setup is settled, the particle identification can be obtained by a two-by-two combination of detector measurements. This redundancy lets us reach the desired resolution and keep systematic uncertainties as low as possible, using the best combination method for the specific measurement.

The *emulsion setup* is focused on the reconstruction of light fragments ($Z \leq 3$) and is made of two components: the upstream region, made of the same *start counter* and *beam monitor detectors* of the electronic setup with the same purposes, and an emulsion cloud chamber (ECC), which is reported in Fig. 2. It is organized in three main regions.

The first part is made of nuclear emulsion films with dimension of 10×12 cm^2 interleaved with layers of target material where fragmentation reactions occur. From there, it is possible to retrieve the origin point of the fragment generated by the interaction between the beam and the target. The length of this section is chosen in such a way as to have the partial (almost 20%) absorption of primary particles, letting only the nuclear fragments reach the following sections. Moreover, it is made in such a way as to reconstruct the energy of the primary at the moment of the fragmentation.

The second section is made of nuclear emulsion layers with a depth of 350 μm, whose aim is charge identification of fragments. In order to increase the capability to distinguish particles with different charges during offline processing, a thermal treatment is applied to the layers in order to increase the dynamic range of the emulsion detector.

The third and last section of the *emulsion setup* is made of emulsion films interleaved with high-density materials such as lexan (1000 μm thick), tungsten (500 μm), and lead (1000 μm). From particle range and multiple Coulomb scattering of the fragments with the layers, it is in fact possible to achieve momentum measurements. By putting together the measurements of the several regions, a complete track reconstruction can be achieved.

3. Preliminary results

Up to now, both setups have been used in different experimental campaigns, employing beams of ^{16}O, ^{12}C, and ^{4}He against targets of C and C_2H_4.

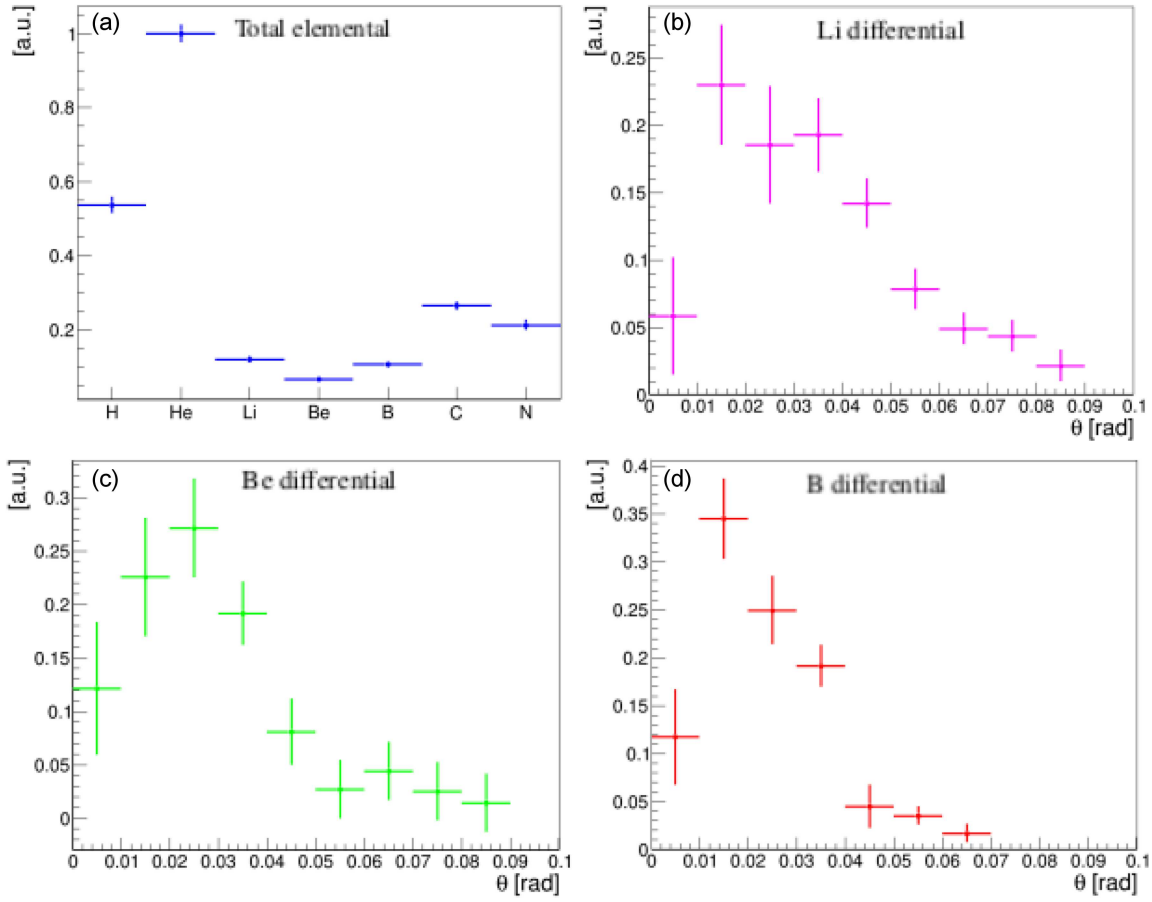

Fig. 4. Total (a) and differential (b–d) cross-section distributions for a 400 MeV/u ^{16}O beam impinging on a C target at GSI in 2021 obtained with the FOOT electronic setup. The shape of the distribution (a) is normalized to the most frequent charge, while the distributions (b–d) are normalized to unit.

From the perspective of the future data takings, the overall ECC detector is completely operational, while the ES is partially under construction, with the finalization foreseen by the end of 2023. In the following, the preliminary results obtained with ^{16}O beams at GSI (Darmstadt, Germany) with both setups are shown.

The results of the ES concern data acquired at the GSI facility in July 2021 on a beam of ^{16}O of 200 MeV/u and 400 eV/u of kinetic energy. The apparatus operated in a reduced setup, but adequate for a cross-section evaluation, and consisted of the full upstream region, part of the tracking system, the ToF-wall detector, and a part of the calorimeter. The charge reconstruction was achieved thanks to the high performance of the ΔE-ToF system composed of the *start counter* and the ToF-wall. In Fig. 3, the charge separation of fragments generated by a 400 MeV/u ^{16}O beam on a 5 mm C target is shown, considering the correlation between $\mathrm{d}E/\mathrm{d}x$ in the ToF-wall and ToF of the particle crossing all the detectors [4]. It is possible to infer that the system is able to measure the charge of the particles with a high resolution, discriminating even light fragments with $Z \leq 3$. In particular, the energy loss accuracy is of the order of 3–4%, while the ToF resolution decreases from 200 ps for lighter fragments to 45–50 ps for the ^{16}O particles.

Figure 4 shows the preliminary total and angular cross-section measurements [5] of 400 MeV/u ^{16}O beam impinging on a 5 mm C target. Since the contributions due to uncertainties and systematic are under investigation, the distributions are normalized in order to emphasize their shape, leaving the final cross-section values for a dedicated paper. What can be verified is that the most abundant generated fragments are the lightest ones, while the angular distribution varies strongly with the charge of the particle.

The ECC apparatus successfully performed a data-taking campaign at the GSI (Darmstadt, Germany) facility in 2019 and 2020 using a ^{16}O beam on C and C_2H_4 targets. Figure 5 reports the tangent of the angle with respect to the beam direction of fragments, separated according to their charge for a 400 MeV/u ^{16}O beam on a C_2H_4 target. The reported tracks are the ones well reconstructed in the second section of the apparatus, while the charge has been distinguished by employing the ionization

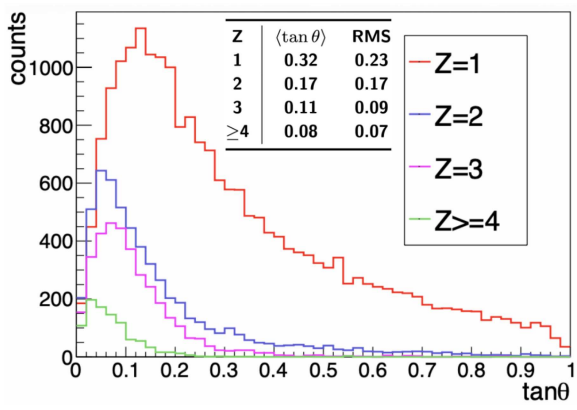

Fig. 5. Charge reconstruction of fragments generated by a 200 MeV/u 16O beam impinging on a 5 mm C_2H_4 target at GSI in 2019.

sensitivity of the second section of the apparatus (for $Z \leq 2$) and further analysis procedures [6]. In particular, the sensitivity of the apparatus is not suited for heavier fragments (for $Z \geq 4$), whose discrimination is not the purpose of this detector. What can be noticed is that the angular distribution becomes wider for lighter particles.

4. Conclusions

The main aim of the FOOT experiment is the measurement of double-differential fragmentation cross-sections in order to overcome the lack of experimental data on light fragments ($Z \leq 10$) in the energy range between 100–800 MeV/u, which is important for the applications in *particle therapy* and space radioprotection. To reach this goal, two different setups were designed, and very promising preliminary results were obtained for each. In both cases, good charge identification performances were found, and cross-section measurements were achieved. The final values will be published in a dedicated paper once all the effects have been investigated.

New data taking will be carried out in the future campaigns foreseen for 2023 and 2024, when the experimental setups will be totally assembled. In particular, the magnets and *calorimeter* of ES will be finalized by the end of 2023.

In conclusion, the reported results lay the foundation structure for data analysis that will be applied also to further data takings, when the experimental setups are completed and enhanced for new measurements.

References

[1] M. Durante, H. Paganetti, *Rep. Prog. Phys.* **79**, 096702 (2016).

[2] M. Durante, F.A. Cucinotta, *Rev. Mod. Phys.* **83**, 1245 (2011).

[3] G. Battistoni M. Toppi,V. Patera, FOOT Collaboration, *Front. Phys.* **8**, 568242 (2020).

[4] A.C. Kraan, G. Battistoni, N. Belcari et al., *Open Physics* **1001**, 167615 (2021).

[5] M. Toppi, A. Sarti, A. Alexandrov et al., *Front. Phys.* **10**, 979229 (2022).

[6] G. Galati, A. Alexandrov, B. Alpat et al., *Open Phys.* **19**, 383 (2021).

Proceedings of the Zakopane School of Physics 2023 International Symposium, Zakopane, Poland, May 23–27, 2023

Magnetoelastic Effect in Perovskite Orthochromite $HoCrO_3$

K. Komędera[a,b] and N.K. Chogondahalli Muniraju[c,*]

[a] *Mössbauer Spectroscopy Laboratory, Institute of Technology, University of the National Education Commission, Podchorążych 2, 30-084 Kraków, Poland*
[b] *Faculty of Physics and Applied Computer Science, AGH University of Krakow, al. Mickiewicza 30, 30-059 Kraków, Poland*
[c] *The Henryk Niewodniczanski Institute of Nuclear Physics, Polish Academy of Sciences, Radzikowskiego 152, 31-342, Kraków, Poland*

Doi: 10.12693/APhysPolA.145.128 *e-mail: cmnkumar@ifj.edu.pl

It is well established that many material properties, such as multiferroicity, magnetoresistance, or magnetoelectricity, emerge from strong interactions of spins and lattice (phonons). An in-depth understanding of spin–phonon coupling is key to understanding these properties. We demonstrate strong spin–phonon coupling in $HoCrO_3$ using powder X-ray diffraction measurements. Our investigations confirm magnetoelastic effects below antiferromagnetic phase transition, $T_N \approx 142$ K. The lattice parameters and unit cell volume decrease normally with temperature up to $\sim T_N$, but decrease anomalously below T_N. By fitting the background thermal expansion for a non-magnetic lattice using the Debye–Grüneisen equation, we determined the lattice strain ΔV_M due to the magnetoelastic effects as a function of temperature. We have also established that the lattice strain due to the magnetoelastic effect in $HoCrO_3$ couples with the square of the ordered magnetic moment of the Cr^{3+} ion.

topics: perovskite, multiferroic, magnetostriction, X-ray diffraction

1. Introduction

The interaction between spin and lattice degrees of freedom is a subject of significant interest in condensed matter research, particularly in relation to electronic materials such as colossal magnetoresistive and multiferroic materials. One of the main manifestations of this coupling is the spontaneous exchange striction linked to magnetic ordering at low temperatures. In non-magnetic materials, the volume of the lattice unit cell varies smoothly with temperature and does not show any anomalous changes at low temperatures. However, in materials with magnetic ions ordering at low temperatures, atomic positions may change at the transition temperature. This leads to lattice strain, and as a consequence, one can expect modifications in the unit cell parameters, unit cell volume, and sometimes lattice symmetry. To determine these anomalous changes effectively, high-resolution diffraction measurements are required, preferably in an extended temperature range above and below the magnetic ordering temperature. This enables a precise determination of phonon-related lattice contraction, which can be subtracted from experimental data to determine excessive changes in lattice parameters due to magnetic ordering.

Perovskite chromites $RCrO_3$ (R = rare-earth or yttrium) have been reconsidered in recent years as possible multiferroic materials in which multiple ferroic orders, such as ferroelectricity and antiferromagnetism, coexist [1–3]. These perovskites are isostructural with rare-earth orthoferrites $RFeO_3$ and crystallize in an orthorhombically distorted perovskite structure with four formula units per unit cell [4]. Orthochromites are paramagnetic at room temperature and magnetically ordered at low temperatures [5–7]. In the case of orthochromite $HoCrO_3$, upon cooling from room temperature, the Cr magnetic sublattice is ordered at $T_N \approx 142$ K, whereas cooperatively induced magnetic ordering of the Ho sublattice was observed at much lower temperatures, $T < 50$ K [8]. Based on a systematic rare-earth site doping study, it was concluded that $HoCrO_3$ shows a strong correlation between crystal structure and magnetism [9]. From our earlier neutron powder diffraction (NPD) studies, we were able to point out the anomalous change in the unit cell volume below T_N [8] in this compound, but the temperature evolution of the anomalous changes was not clearly determined around T_N. This was due to a limited number of NPD data sets as a function of temperature around T_N. Furthermore, the previous report lacked the high-temperature data required

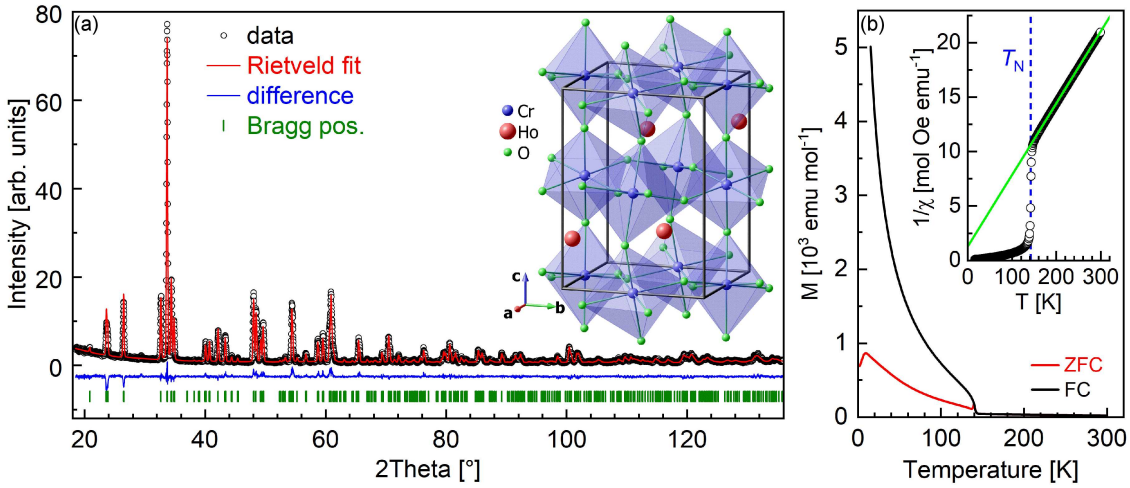

Fig. 1. (a) Powder X-ray diffraction pattern collected at 298 K along with Rietveld refinement results. Circles are the experimentally measured intensities, and the solid line (red) is the curve obtained by Rietveld fitting. Vertical bars (green) mark the positions of expected Bragg reflections. The blue horizontal curve at the bottom is a difference between the measured and calculated patterns. The inset shows a clinographic view of a lattice unit cell along with distorted Cr–O octahedra. (b) The zero-field-cooled (ZFC) and field-cooled (FC) magnetization measured under 500 Oe applied field shows a bifurcation around 142 K, indicating the magnetic transition. The inset shows the Curie–Weiss fit to inverse susceptibility, which unambiguously shows the deviation of the experimental curve below 142 K indicated by the vertical dashed line.

TABLE I

Structural parameters for $HoCrO_3$ obtained from the Rietveld refinement of powder XRD data collected at 298 K.

Atom	Site	Occ.	x	y	z
Ho	4c	1	−0.0178	0.0651	0.25
Cr	4b	1	0.5	0	0
O(1)	4c	1	0.097	0.473	0.25
O(2)	8d	1	0.695	0.297	0.0478

for a better evaluation of structural changes around and below the magnetic phase transition. The current study, which includes much denser data sets around T_N, as well as high-temperature data (up to 998 K), has enabled us to determine the spin-lattice coupling in these compounds more precisely.

2. Experimental details

A polycrystalline sample of $HoCrO_3$ was synthesized by a conventional solid-state chemical reaction of Ho_2O_3 and Cr_2O_3 in a stoichiometric ratio. The precursors were mixed using an agate ball mill and heat-treated at 1100°C for 48 h in the presence of atmospheric air. Further details of the synthesis can be found in [10]. The phase purity of the synthesized powder sample was then confirmed by powder X-ray diffraction (PXRD) measured on a Panalytical Empyrean powder diffractometer with a Cu K_α radiation source. Measurements were done using Bragg–Brentano geometry on finely powdered samples. After confirming the phase purity, several PXRD patterns were collected in a wide temperature range of 9–998 K. The diffraction patterns were analyzed by the Rietveld method using the software Mag2Pol [11]. The magnetization of the polycrystalline $HoCrO_3$ sample was measured by a Quantum Design superconducting quantum interference device magnetometer in the temperature range from 2 to 300 K under the magnetic field 500 Oe.

3. Results and discussion

The Rietveld refinement results of the PXRD data at 298 K are presented in Fig. 1a. Inset in Fig. 1a shows a clinographic view of a refined crystal structure using the orthorhombic space group *Pbnm*. This orthorhombically distorted perovskite structure contains four formula units of $HoCrO_3$ per unit cell. The refined lattice and structural parameters at 298 K are displayed in Table I. The field-cooled (FC) and zero field-cooled (ZFC) direct current (DC) magnetization curves measured with an applied magnetic field of 500 Oe presented in Fig. 1b show a bifurcation around ∼ 142 K. It is attributed to the magnetic ordering of the Cr^{3+} sublattice [7, 8, 12]. The thermal evolution of reciprocal susceptibility calculated from the FC magnetization curve is presented as inset in Fig. 1b. The inverse susceptibility follows the Curie–Weiss law above T_N, and there is a marked deviation below T_N, as shown in the inset of Fig. 1b. From the Curie–Weiss fit of the magnetic susceptibility, the effective moment is found to be $11.01 \pm 0.02\ \mu_B$, which is very similar to

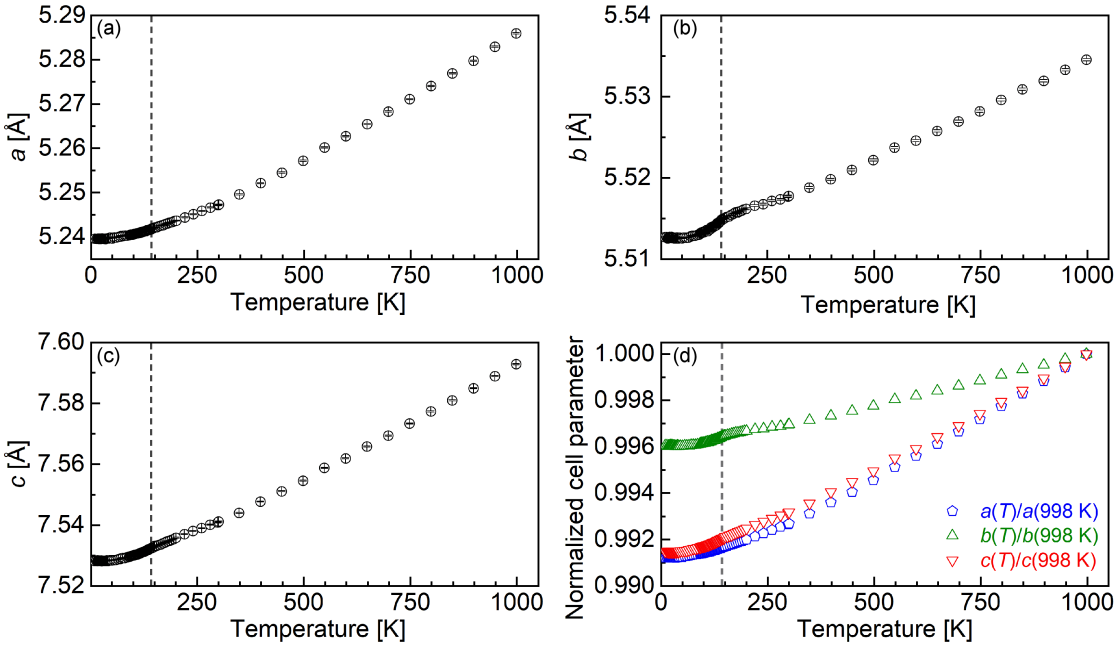

Fig. 2. Panels (a), (b), and (c) show the temperature evolution of lattice parameters a, b, and c, respectively. The Néel temperature $T_{\mathrm{N}} = 142$ K is indicated by vertical dashed lines. Panel (d) shows the lattice parameters normalized to the value obtained at 980 K.

the value from the earlier report [8]. By considering the theoretical values 3.87 μ_{B} for Cr^{3+} (for the spin only $S = 3/2$) and 10.63 μ_{B} for Ho^{3+} ($J = 8$) and assuming that the total effective magnetic moment is given by $\mu_{\mathrm{total}} = [\mu^2_{\mathrm{eff}}(Cr^{3+}) + \mu^2_{\mathrm{eff}}(Ho^{3+})]^{1/2}$, we expect a total magnetic moment of 11.31 μ_{B}. Thus, the experimental effective magnetic moment is very close to the expected value.

To determine the structural changes and to elucidate their relation to magnetic order, diffraction data was collected in the temperature range 9–998 K. Refinements of the diffraction patterns in the whole temperature range indicated no structural transition, and the structure remained orthorhombic $Pbnm$. Figure 2a–c shows the variations of lattice parameters a, b, and c. The variations of lattice parameters with temperature do not show discontinuous changes, but all three lattice parameters show an anomalous change below $\sim T_{\mathrm{N}}$, indicated by a vertical dashed line in the figure. It is worth noting that from the normalized values of temperature evolution of the lattice parameters presented in Fig. 2d, the reduction in the lattice parameter b as a function of temperature is much smaller compared to the reductions in a and c. This indicates that b is relatively stiff compared to the other two crystallographic axes. The anomalies observed in lattice parameters affect the unit cell volume of $HoCrO_3$. As shown in Fig. 3, the unit cell volume also shows anomalous change below T_{N}. In order to elucidate the excessive change in the volume of the unit cell due to magnetoelastic effects, it is necessary to determine expected changes in the volume of the lattice cell in the absence of a magnetic phase transition. One way to determine the background temperature variation of lattice parameters and unit cell volume is to extrapolate the temperature variation of these parameters in the paramagnetic phase down to low temperatures by fitting them with a polynomial function [13]. This method works approximately in some cases, but in general, it involves some uncertainty. Alternatively, one can use the Grüneisen approximation for the zero-pressure equation of state, in which the effects of thermal expansion are considered to be equivalent to elastic strain [14, 15]. Thus, the temperature dependence of the volume can be described by

$$V(T) = \frac{\gamma}{B} U(T) + V_0, \tag{1}$$

where γ is a Grüneisen parameter, B is the bulk modulus, and V_0 is the unit cell volume at $T = 0$ K in the absence of magnetoelastic effect. The internal energy, $U(T)$, can be obtained via a Debye approximation for the heat capacity, i.e.,

$$U(T) = 9Nk_{\mathrm{B}}T \left(\frac{T}{\theta_{\mathrm{D}}}\right)^3 \int_0^{\theta_{\mathrm{D}}} \mathrm{d}x \, \frac{x^3}{\mathrm{e}^x - 1}, \tag{2}$$

where N is the number of atoms in the unit cell, k_{B} is Boltzmann's constant, θ_{D} is the Debye temperature, and $x = \hbar\omega/(k_{\mathrm{B}}T)$. The experimental unit cell volume was fitted to (1) along with (2) in the paramagnetic temperature range $150 < T < 998$ K. The fitting parameters V_0, θ_{D}, and $9Nk_{\mathrm{B}}\frac{\gamma}{B}$ were determined through a least-squares fitting procedure. The determined parameters are presented in Table II. The resulting fit that describes the evolution of the unit cell volume in the absence of

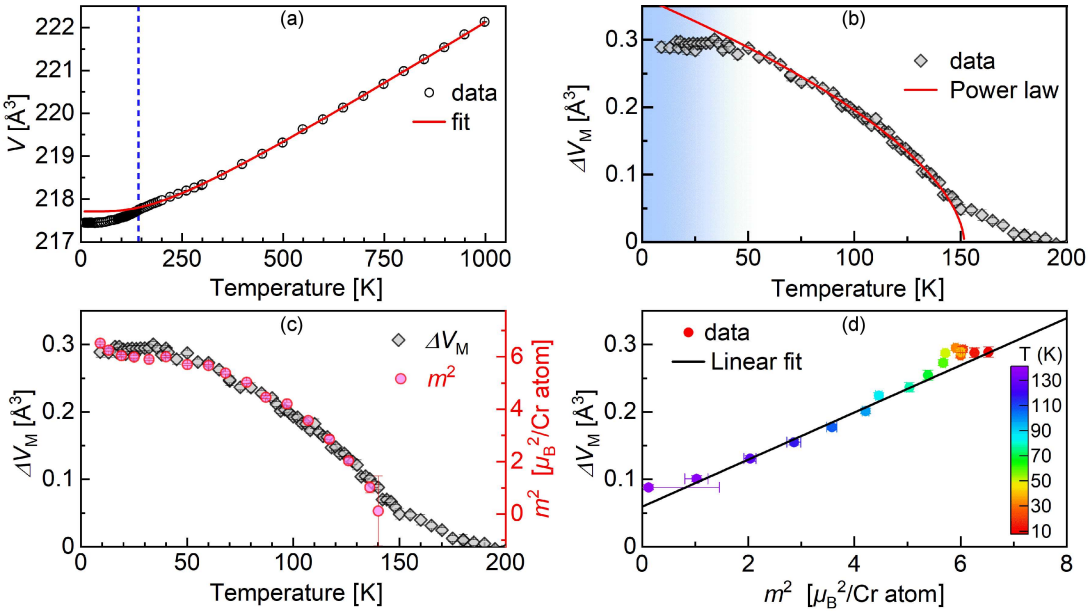

Fig. 3. (a) Temperature evolution of the unit cell volume obtained from diffraction measurements (circles) and fit using the Grüneisen approximation presented in (1) (line). (b) Temperature evolution of excessive change in the unit cell volume ΔV_{M} fitted to a power-law. The changes in ΔV_{M} saturates below 50 K, where Ho^{3+} ordering becomes dominant. (c) Temperature evolution of excessive change in the unit cell volume ΔV_{M} (left scale) and square of the ordered Cr^{3+} magnetic moments (m^2) (right scale). (d) The excessive change in the unit cell volume plotted against m^2 at several temperatures. The inset color bar indicates the temperature range of experimental data points.

magnetic ordering is shown as a solid line in Fig. 3a. A clear deviation between the fit and experimental data was observed slightly above $T_{\mathrm{N}} = 142$ K. It can be inferred that this is an indication of strong magnetostriction or magnetoelastic effects in this system. The volume change due to magnetoelastic effects is expected to be proportional to the square of the ordered magnetic moment [16]. The excessive change in the unit cell volume due to magnetoelastic effects, ΔV_{M}, presented in Fig. 3b, was revealed by taking the difference between the experimental unit cell volume and the fit to Grüneisen approximation. The results ΔV_{M} follow a power-law given by the expression $\Delta V_{\mathrm{M}}(T) = \Delta V_{\mathrm{M}}(0)\ (T_{\mathrm{N}} - T/T_{\mathrm{N}})^{\beta}$. Here, $\Delta V_{\mathrm{M}}(T)$ is the temperature evolution of ΔV_{M}; $\Delta V_{\mathrm{M}}(0)$ is ΔV_{M} at 0 K; T_{N} and β are the Néel temperature and the critical exponent, respectively. From the fit shown as a continuous curve in Fig. 3b, we obtained $T_{\mathrm{N}} = 151 \pm 3$ K and the critical exponent $\beta = 0.57 \pm 0.07$. The thus obtained T_{N} is in agreement with magnetic data. A small deviation of power-law fit can be observed below 50 K, which coincides with the temperature at which magnetic ordering of the rare-earth Ho^{3+} sub-lattice is observed [8]. In Fig. 3c, we present ΔV_{M} along with the square of the ordered magnetic moment of the Cr^{3+} ion, obtained by neutron diffraction experiments [8]. It is immediately clear from Fig. 3c that excessive changes in the unit cell volume follow the ordered magnetic moments of the Cr^{3+} ion. In Fig. 3d, ΔV_{M} is plotted against a square of the Cr^{3+} ordered magnetic moments at several temperatures, showing a linear relation. This unambiguously confirms that the anomalous change in lattice parameters and unit cell volume in $HoCrO_3$ is due to spontaneous magnetostriction or magnetoelastic effects.

TABLE II

The results of least-squares fitting using Grüneisen approximation (see (1)).

V_0 [Å^3]	θ_{D} [K]	$9Nk_{\mathrm{B}}\frac{\gamma}{B}$ [Å^3/K]
217.75(1)	732(11)	0.0178(1)

4. Conclusions

We have investigated spontaneous magnetoelastic effects or magnetostriction in $HoCrO_3$ by means of powder X-ray diffraction in an extended temperature range. The results of our investigation show that all lattice parameters and unit cell volume exhibit an anomalous change below $T_{\mathrm{N}} = 142$ K. By subtracting the background thermal expansion for a non-magnetic lattice, we determined the lattice strain ΔV_{M} due to magnetoelastic effects as a function of temperature below T_{N}. We also show that the lattice strain due to spontaneous magnetostriction in $HoCrO_3$ couples with the square of the ordered magnetic moment of the Cr^{3+} ion.

Acknowledgments

The work was supported by the National Science Centre, Poland, Grant No. OPUS: 2021/41/B/ST3/03454; the Polish National Agency for Academic Exchange under "Polish Returns 2019" Programme No. PPN/PPO/2019/1/00014 and the subsidy of the Ministry of Science and Higher Education of Poland. We acknowledge the support from the "Excellence Initiative-Research University" program for AGH University of Krakow.

References

[1] J.R. Sahu, C.R. Serrao, N. Ray, U.V. Waghmare, C.N.R. Rao, *J. Mater. Chem.* **17**, 42 (2007).

[2] B. Rajeswaran, D.I. Khomskii, A.K. Zvezdin, C.N.R. Rao, A. Sundaresan, *Phys. Rev. B* **86**, 214409 (2012).

[3] K.R.S. Preethi Meher, A. Wahl, A. Maignan, C. Martin, O.I. Lebedev, *Phys. Rev. B* **89**, 144401 (2014).

[4] S. Geller, E.A. Wood, *Acta Crystallogr.* **9**, 563 (1956).

[5] E. Bertaut, J. Mareschal, G. De Vries, R. Aleonard, R. Pauthenet, J. Rebouillat, V. Zarubicka, *IEEE Trans. Magn.* **2**, 453 (1966).

[6] E.F. Bertaut, J. Mareschal, *Solid State Commun.* **5**, 93 (1967).

[7] P. Pataud, J. Sivardiere, *J. Phys.* **31**, 803 (1970).

[8] N.K. Chogondahalli Muniraju, Ph.D. Thesis, Forschungszentrum Juelich GmbH and RWTH Aachen University, 2012.

[9] S. Yin, M.S. Seehra, C.J. Guild, S.L. Suib, N. Poudel, B. Lorenz, M. Jain, *Phys. Rev. B* **95**, 184421 (2017).

[10] C.M.N. Kumar, Y. Xiao, H.S. Nair, J. Voigt, B. Schmitz, T. Chatterji, N.H. Jalarvo, Th. Bruckel, *J. Phys. Condens. Matter* **28**, 476001 (2016).

[11] N. Qureshi, *J. Appl. Crystallogr.* **52**, 175 (2019).

[12] R.M. Hornreich, B.M. Wanklyn, I. Yaeger, *Inter. J. Magn.* **2**, 77 (1972).

[13] T. Chatterji, B. Ouladdiaf, D. Bhattacharya, *J. Phys. Condens. Matter* **21**, 306001 (2009).

[14] F. Sayetat, P. Fertey, M. Kessler, *J. Appl. Crystallogr.* **31**, 121 (1998).

[15] D.C. Wallace, *Thermodynamics of crystals*, Dover Publications, New York 1998.

[16] A.V. Andreev, *Handbook of Magnetic Materials*, Vol. 8, Elsevier, Amsterdam 1995.

Proceedings of the Zakopane School of Physics 2023 International Symposium, Zakopane, Poland, May 23–27, 2023

Prussian Blue Analogues Cubes in the Organic Polymer Electrospun Fibres

A. Pacanowska[a], N.K. Chogondahalli Muniraju[a], W. Sas[a,b], M. Perzanowski[a], M. Mitura-Nowak[a] and M. Fitta[a]

[a] *Institute of Nuclear Physics Polish Academy of Sciences, Radzikowskiego 152, 31-342 Kraków, Poland*
[b] *Institute of Physics, Bijenička 46, 10000 Zagreb, Croatia*

Doi: 10.12693/APhysPolA.145.133 *e-mail: magdalena.fitta@ifj.edu.pl

This report presents the preparation and characterization of a new composite containing Prussian blue analogues nanoparticles and poly(N-vinyl-2-pyrrolidone) (PVP). Nanoparticles of nickel hexacyanoferrate (NiHCFe) and nickel hexacyanochromate (NiHCCr) were synthesized by the citrate-assisted co-precipitation method. Basic characterization revealed uniform cubic particles with an average size of 238 nm (NiHCFe) and 80 nm (NiHCCr). In the next step, these nanocubes were incorporated into composite fibres using electrospinning technique. The resulting fibres exhibited distinctive colours, and scanning electron microscope imaging showed differences in fibre morphology between NiHCFe/PVP and NiHCCr/PVP composites. The obtained results indicate the successful synthesis and characterization of Prussian blue analogue nanoparticles, as well as their integration into composite fibres, opening up possibilities for diverse applications.

topics: molecular magnetism, Prussian blue analogues, nanoparticles, electrospun fibres

1. Introduction

Prussian blue analogues (PBAs) are examples of compounds showing unique properties, e.g., room temperature ferromagnetism, compensation point, or zero thermal expansion [1–4]. Moreover, PBAs are examples of mixed-valence compounds due to the metal-to-metal charge transfer mediated by the cyano ligand and possess structural flexibility due to the stretching and vibrational modes of the cyano-bridging ligand [5]. These features play important roles in the various magnetic functionalities, such as reversible photomagnetism, humidity-sensitive magnetism, or high ionic conductivity [6, 7]. The attributes described above make these materials useful in practical applications, including gas storage, catalysis, batteries, and energy separation. Prussian blue (PB) and PBAs are also the subjects of increasing interest because of the possibility of producing molecule-based magnets in reduced dimensionality, i.e., in thin films and nanoparticles [8]. Easy synthesis route, controllable shape and size, biocompatibility, biodegradability, and low production cost make the PB/PBA nanoparticles suitable material for biomedical applications such as targeted drug delivery systems or cancer treatment [9,10]. Moreover, the nanoparticles of PB/PBA are potential candidates for molecular sensors [11] or energy storage devices [12].

However, using the application potential of coordination systems requires some fabrication methodology of robust devices that can be handled and integrated without compromising functionality. One of the approaches allowing the achievement of this objective is the incorporation of the molecular system into the polymer matrix. The polymer matrix allows the development of different shapes, such as beads, spongy foam, membranes, and fibres. In the literature, one can find several examples of composite materials based on PBAs and organic polymers, such as collagen [13] or polyacrylonitrile [14]. These nanocomposites have received much attention as materials for radioactive Cs removal due to their affinity for adsorbing Cs^+ or microwave absorption.

Here, we report the preparation and characterization of the electrospun composites based on PVP and nanoparticles (NPs) of Prussian blue analogues. In the first stage of our work, we focused on the synthesis of the cyanido-bridged nanoparticles with narrow size distribution. Subsequently, the obtained nanoparticles were loaded into the polymeric matrix by use of electrospinning method. This straightforward technique enables the creation of fibres with diameters spanning from nano- to micrometres [15]. Its key benefits include cost-effectiveness, the capability to manufacture materials with a substantial surface area-to-volume ratio, and its adaptability

to various materials. Additionally, electrospinning offers the potential for integrating magnetic nanoparticles into electrospun fibre mats, maintaining both magnetic functionality and mechanical properties.

2. Material preparation and characterization

2.1. Materials

The following chemicals were purchased from Sigma-Aldrich without further purification: nickel(II) nitrate hexahydrate, trisodium citrate tetrahydrate, potassium hexacyanoferrate(III), potassium hexacyanochromate(III), poly(N-vinyl-2-pyrrolidone) (PVP) M_w = 360 000 Da, and methanol.

2.2. Synthesis of PBA-NP NiHCM, M = [Fe, Cr]

In the following study, the literature protocol [16] for producing PBA nanoparticles in the presence of citrate anion was modified and used to produce two types of PBA NPs, i.e., nickel hexacyanoferrate (NiHCFe) and nickel hexacyanochromate (NiHCCr).

Nanoparticles of NiHCFe. In the first flask, 1.2 mmol of nickel(II) nitrate hexahydrate and 1.8 mmol of trisodium citrate tetrahydrate were dissolved in 40 ml of water. In the second flask, 0.8 mmol of potassium hexacyanoferrate(III) was dissolved in 40 ml of H_2O. After mixing both solutions, the mixture was left on magnetic stirring for 48 h at room temperature (20°C). The final product was separated from the supernatant by centrifugation at 9000 rpm for 15 min at a temperature of 10°C. The cleaning for the final product was as follows: a three-step washing procedure with distilled water and centrifugation at 9000 rpm for 15 min and at 10°C. The resulting orange solid was dried in a vacuum oven at 40°C for 20 h.

Nanoparticles of NiHCCr. The above synthetic protocol was repeated by substituting the source of cyanometallate for potassium hexacyanochromate(III). The precipitated material was washed with distilled water three times by centrifugation. The resulting light blue solid was dried in a vacuum oven at 40°C for 20 h.

2.3. Preparation of electrospun fibres

Composite fibres of NiHCM-PVP. The polymeric solution for electrospinning was prepared by introducing 43.00 mg of NiHCM (M = Fe, Cr) into 3 ml of MeOH. To ensure homogenous dispersion, the mixture was sonicated for 2 min without pulsation using an ultrasonic homogenizer. Then, ∼ 0.350 g of the PVP 360 powder was introduced to suspension to give a solution of 12 wt% PVP/MeOH+NiHCM and immediately put on the gyromixer for 3 h for the complete dissolution of polymer and to obtain a homogenous solution for electrospinning.

The polymer solution was inserted into the plastic syringe, from which it was electrospun with the homemade electrospinning equipment. During the process, the following conditions were applied: a voltage of 11 kV, room temperature (∼ 20°C), relative humidity in the range of 46–52%, and constant flow rate of 1.5ml/h. The fibre mats were collected on a metallic plate collector randomly, with a distance between the tip and the collector equal to 10.5 cm.

2.4. Physical methods

Microstructure and composition analysis of films was performed using a TESCAN VEGA3 scanning electron microscope equipped with an X-ray energy dispersive spectrometer EDAX Bruker. For imaging under the electron microscope, small amounts of the freshly prepared NiHCFe and NiHCCr nanoparticles were dispersed by sonication in MeOH in order to obtain highly diluted solutions. The material was then transferred into the freshly cleaned Si (100) wafer by drop-casting and put aside for the solvent to evaporate. In the case of composite materials, they were directly electrospun onto the Si (100) wafers in small amounts to minimize the charging effects during imaging. The size of the particles and the diameters of the fibres were measured with the use of ImageJ software. The average sizes were calculated based on the lognormal distribution.

Powder X-ray diffraction (PXRD) data of nanoparticles and composites were collected on a PANalytical X'Pert PRO diffractometer equipped with a Cu K_α radiation source. The measurements were done using the Bragg–Brentano geometry. The diffraction patterns were indexed to determine the space group, and the lattice parameters were determined by doing a full-pattern Le Bail fit using the Mag2Pol software [17]. The indexing tool in Mag2Pol uses instrument geometry and the observed peak positions in a powder pattern and is based on the successive dichotomy method [18].

Raman measurements were performed using a confocal micro-Raman spectrometer (Nicolet Almega XR) equipped with a 532 nm laser. For powdered NiHCFe/NiHCCr, the measurement was performed with 1% of laser power to minimize the burning of the samples. NiHCM/PVP composites were directly electrospun onto the Si (100) wafers in small amounts, similar to preparation for scanning electron microscope (SEM) imaging. The measurements of composites were performed with 10% of laser power.

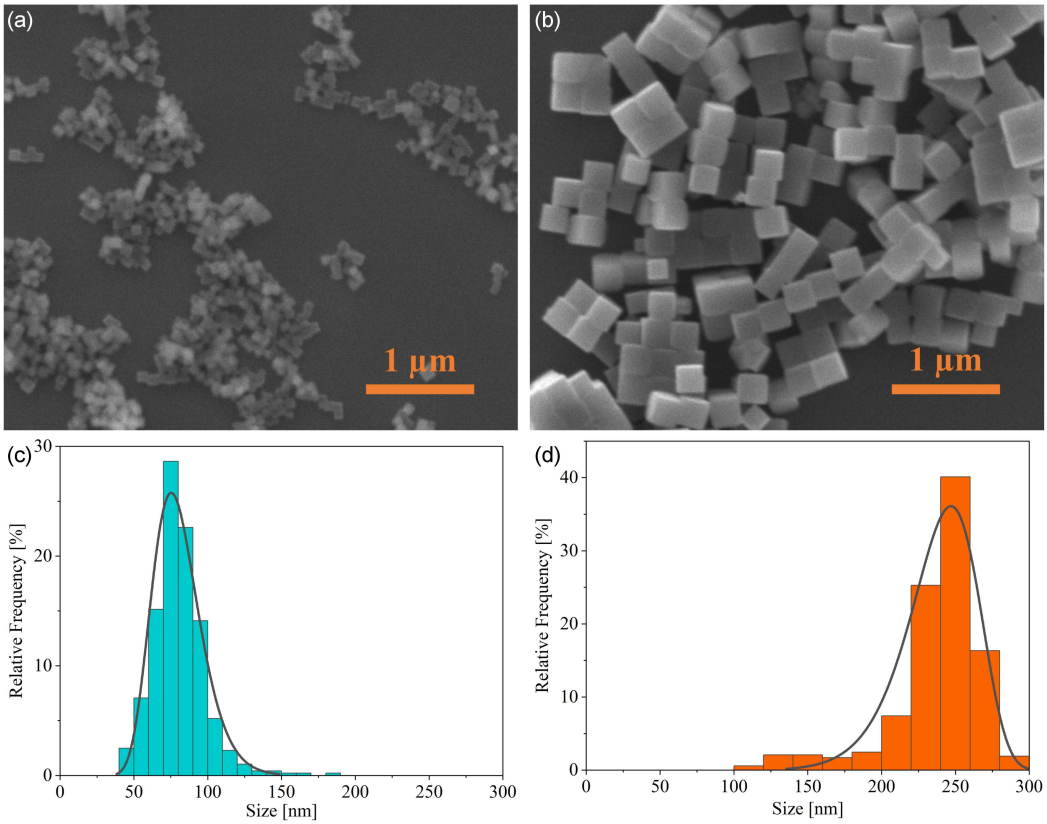

Fig. 1. (a, c) SEM image of NiHCCr NP, with lognormal distribution curve; (b, d) SEM image of NiHCFe NP, with Weibull distribution curve.

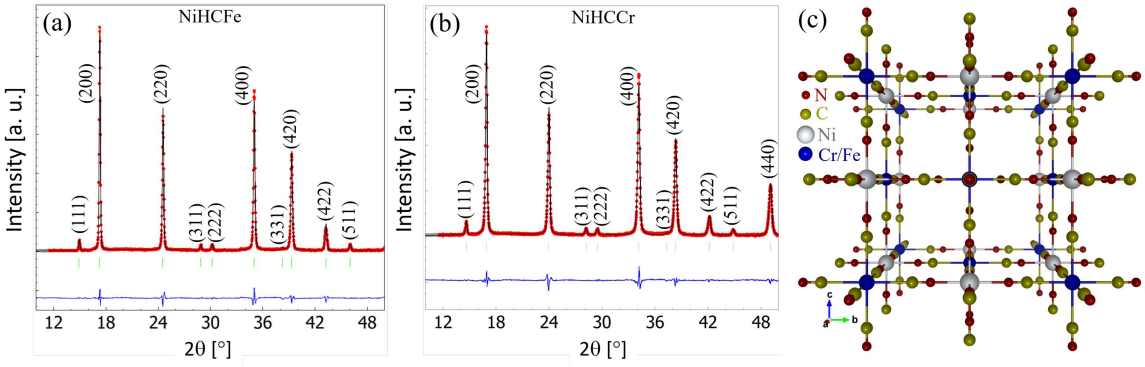

Fig. 2. X-ray diffraction data of (a) NiHCFe and (b) NiHCCr. The red circles are the experimental data, and the black curve is the profile calculated using the Le Bail method. Vertical bars indicate the expected Bragg positions, which are indexed and shown above. (c) A perspective view of NiHC(Fe/Cr) framework structure in a cubic Fm-3m space group.

3. Results and discussion

PBA nanoparticles obtained in the synthetic protocol utilizing trisodium citrate salts as a size-tuning agent resulted in uniform, cubic-shaped particles presented in Fig. 1a and b. The size dispersion of cube diameter (Fig. 1c and d) showed that, despite the same synthetic protocol, the average diameter of the NiHCFe cubes (238 ± 37 nm) was three times bigger than for NiHCCr (80 ± 17 nm).

All the observed peaks of PXRD patterns of both samples were indexed with the cubic space group Fm-3m. No discernible impurity peaks were found in either compound. From the full-pattern Le Bail fit, the cubic unit cell parameter for NiHCFe and NiHCCr is found to be 10.2294(4) Å and 10.5016(6) Å, respectively. The Le Bail fit results of NiHCFe and NiHCCr are presented in Fig. 2a and b, respectively. Figure 2c shows a perspective view of the cubic lattice of the NiHC(Fe/Cr) framework.

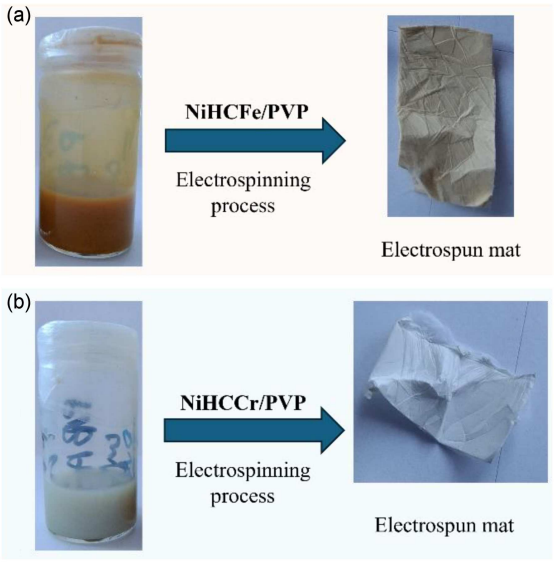

Fig. 3. Photographs of the polymer solutions prepared for the electrospinning process and the obtained electrospun mats.

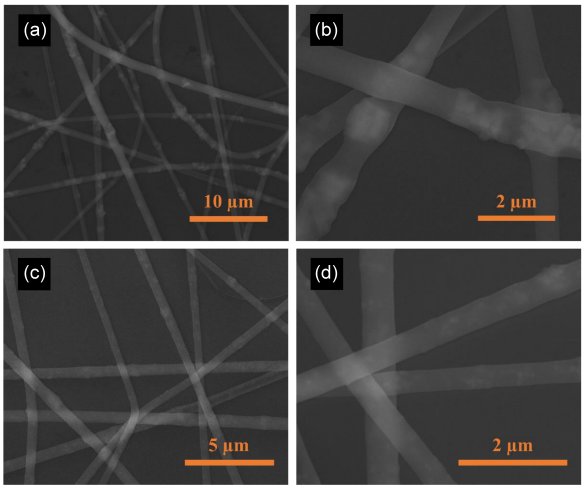

Fig. 4. The SEM pictures of the electrospun PVP nanofibres doped by NiHCFe (a, b) and NiHCCr (c, d) particles.

In the preparation of composite materials containing PBA nanocubes in the form of electrospun fibres, it was necessary to carefully choose the polymer matrix as well as the solvent for the electrospinning solution. In this manner, poly(N-vinyl-2-pyrrolidone) (PVP) was chosen with the average molecular weight M_n = 360 kDa. It was selected due to its chemical stability and non-toxicity, as well as its widely used application as a stabilizing and capping agent in the synthesis of PB-type nanoparticles [19]. Methanol, in which PVP fully dissolves, was used as a solvent. In the first step of preparation of the solution for electrospinning, it was necessary to ensure a homogenous suspension of NiHCM nanocubes. For this reason, the mixture of freshly synthesized and dried PBA nanocubes was

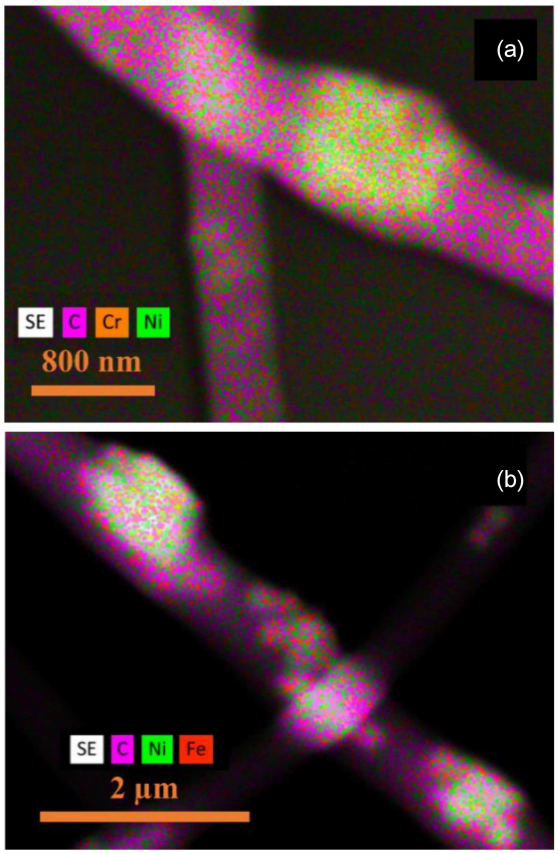

Fig. 5. Elemental mapping of PVP nanofibres loaded with 12 wt.% NiHCCr (a) and NiHCFe (b) nanoparticles by EDS.

redispersed in an appropriate amount of methanol with the use of an ultrasonic homogenizer. After the procedure, the formation of aggregates in the suspension was not observed. Introducing adequate amounts of PVP 360 to form a 12 wt% polymer solution and allowing for the full dissolution of the polymer resulted in a solution ready for the electrospinning process (Fig. 3).

The electrospinning process of as-prepared PVP-based solutions with the initial concentration of NiHCM in composites equal to 12 wt% resulted in materials of two distinctive colours following the starting solutions — light orange and white, respectively for NiHCFe and NiHCCr (Fig. 3). The observation of freshly deposited electrospun fibres on a silicon wafer under SEM imaging presented in Fig. 4 showed differences in both materials due to the different dimensions of NiHCFe and NiHCCr nanocubes. For the NiHCFe/PVP material, the diameter of the PVP fibres was equal to 0.69 ± 0.15 μm, whereas the diameter of the thickened fragments resulting from nanocubes incorporation was equal to 0.97 ± 0.18 μm. In the case of the NiHCCr/PVP composites, the average PVP diameter is slightly diminished to 0.56 ± 0.12 μm, and the areas of the nanocubes aggregation resulted in the fibres thickening up

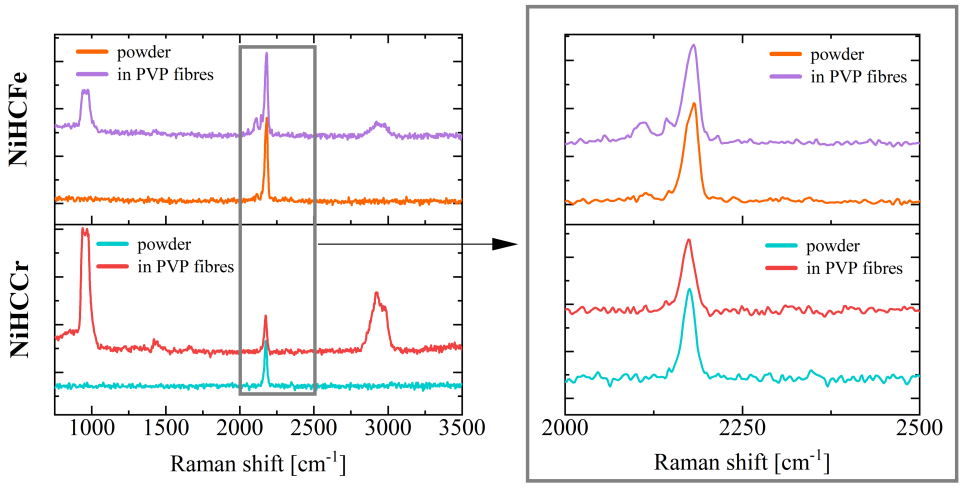

Fig. 6. Raman spectra of composite fibres of NiHCM-PVP and NiHCM bulk sample. On the right: enlargement of Raman spectra in the ν(CN) region.

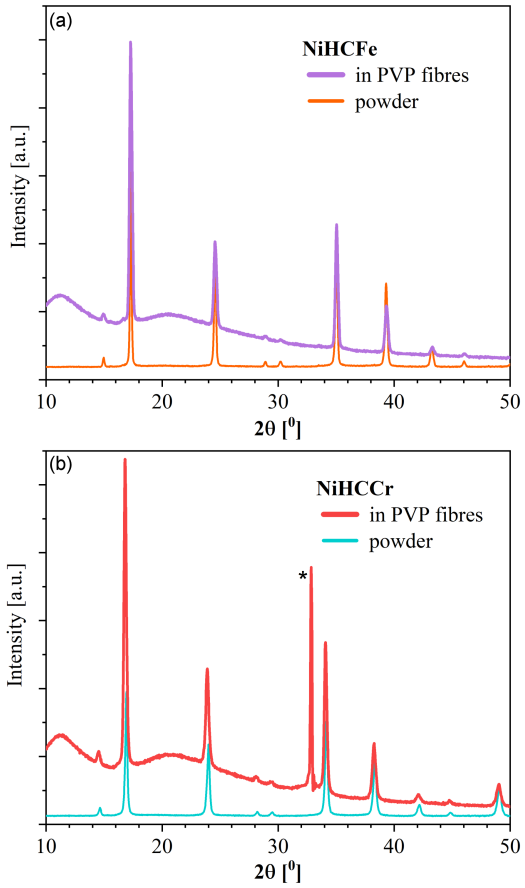

Fig. 7. The XRD pattern measured for composite fibres of NiHCM-PVP and NiHCM bulk sample.

to 0.70 ± 0.14 μm. The broadening effect of the PVP fibre diameters is up to 40% and 25%, respectively, for the NiHCFe/PVP and NiHCCr/PVP composites. Energy dispersive X-ray spectroscopy (EDS) mapping of the thickened fragments of the fibres presented in Fig. 5 confirmed that they originate from the incorporated nanocubes. Moreover, the incorporation of the cubical particles does not disrupt the structure of the fibre, as their dimensions are much smaller than fibre diameters. For both types of materials, the distribution of the nanocubes along the fibres is not perfectly homogenous, however, the diminished size of NiHCCr allows for noticeably better fibre morphology, which may have repercussions on the mechanical properties of the composite materials.

Raman spectroscopy was employed to investigate the composition of obtained materials. As depicted in Fig. 6, the Raman spectra of NiHCCr exhibited one prominent peak concentrated at 2175 cm^{-1}, corresponding to the CN vibrations of Cr^{III}–C≡ N–Ni^{II}. On the other hand, the Raman spectra obtained for NiHCFe exhibited one predominant peak at 2180 cm^{-1} originating from the CN vibration in Fe^{III}–C≡ N–Ni^{II} and two additional bands centred at 2145 cm^{-1} and 2110 cm^{-1}. The presence of these weaker bands reveals a partial reduction of Fe and indicates the appearance of Fe^{2+} in the samples. The appearance of the band corresponding to the CN vibrations in the Raman spectra registered for composite material confirms the effective incorporation of PBA nanoparticles into electrospun fibres.

Figure 7 shows the comparison of the X-ray diffraction (XRD) patterns of PVP and composites. XRD pattern of PVP confirms the amorphous nature of this polymer, where two distinct diffraction peaks were identified within the 10–15 and 15–24 ranges. These peaks might be associated with the two chain length and orientation, giving rise to the existence of two distinct amorphous phases of PVP. This observation aligns with existing literature [20, 21]. The XRD pattern of NiHCFe/PVP and NiHCCr/PVP composites exhibits peaks from both components, suggesting a successful blending of the two materials. The good quality of the

obtained data also suggests a relatively high loading of the PBA-type nanocubes into the PVP fibres, observed in the distinctive colours of the electrospun mats (Fig. 3). The additional peak in the XRD pattern of NiHCCr/PVP marked by a star comes from the silicon background.

4. Conclusions

Two types of Prussian blue analogue (PBA) nanoparticles, namely nickel hexacyanoferrate (NiHCFe) and nickel hexacyanochromate (NiHCCr), were synthesized by the citrate-assisted co-precipitation method. The SEM images showed uniform and cubic-shaped particles for both types of nanoparticles. The electrospun fibres exhibited distinctive colours based on the type of PBA nanoparticles used. The mats were characterized using a scanning electron microscope (SEM), X-ray energy dispersive spectrometer (EDS), powder X-ray diffraction (PXRD), and Raman spectroscopy. The fibre morphology reveals differences between NiHCFe/PVP and NiHCCr/PVP composites, namely the incorporation of NiHCFe into PVP fibres brings about an increase in fibre diameter. EDS mapping confirmed the incorporation of nanocubes in the fibres without disrupting their structure. These results suggest the successful synthesis and characterization of PBA nanoparticles and their incorporation into composite fibres, paving the way for potential applications in various fields.

References

[1] L. Catala, T. Mallah, *Coord. Chem Rev.* **346**, 32 (2017).

[2] S. Ferlay, T. Mallah, R. Ouahès, P. Veillet, M. Verdaguer, *Nature* **378**, 701 (1995).

[3] W.R. Entley, G.S. Girolami, *Science* **268**, 397 (1979).

[4] S. Margadonna, K. Prassides, A.N. Fitch, *J. Am. Chem. Soc.* **126**, 15390 (2004).

[5] K.R. Dunbar, R.A. Heintz, *Chemistry of Transition Metal Cyanide Compounds: Modern Perspectives*, 1996, p. 283.

[6] J. Milon, M.-C. Daniel, A. Kaiba, P. Guionneau, S. Brandès, J.-P. Sutter, *J. Am. Chem. Soc.* **129**, 13872 (2007).

[7] S.S. Kaye, J.R. Long, *J. Am. Chem. Soc.* **127**, 6506 (2005).

[8] O. Sato, T. Iyoda, A. Fujishima, K. Hashimoto, *Science* **271**, 49 (1996).

[9] S. Mukherjee, R. Kotcherlakota, S. Haque, S. Das, S. Nuthi, D. Bhattacharya, K. Madhusudana, S. Chakravarty, R. Sistla, C.R. Patra, *ACS Biomater. Sci. Eng.* **6**, 690 (2020).

[10] C.R. Patra, *Nanomedicine* **11**, 569 (2016).

[11] R. Koncki, *Crit. Rev. Anal. Chem.* **32**, 79 (2002).

[12] B. Wang, Y. Han, X. Wang, N. Bahlawane, H. Pan, M. Yan, Y. Jiang, *IScience* **3**, 110 (2018).

[13] L. Peng, L. Guo, J. Li, W. Zhang, B. Shi, X. Liao, *Sep. Purif. Technol.* **307**, 122858 (2023).

[14] F. Chen, S. Zhang, R. Guo, B. Ma, Y. Xiong, H. Luo, Y. Cheng, X. Wang, R. Gong, *Compos. B Eng.* **224**, 109161 (2021).

[15] J. Xue, T. Wu, Y. Dai, Y. Xia, *Chem. Rev.* **119**, 5298 (2019).

[16] S. Keßler, G. González-Rubio, E.R. Reinalter, M. Kovermann, H. Cölfen, *Chem. Commun.* **56**, 14439 (2020).

[17] N. Qureshi, *J. Appl. Crystallogr.* **52**, 175 (2019).

[18] A. Boultif, D. Louër, *J. Appl. Crystallogr.* **37**, 724 (2004).

[19] T. Uemura, S. Kitagawa, *J. Am. Chem. Soc.* **125**, 7814 (2003).

[20] M.A. Ahmed, R.M. Khafagy, S.T. Bishay, N.M. Saleh, *J. Alloys Compd.* **578**, 121 (2013).

[21] M.T. Razzak, Zainuddin, Erizal, S.P. Dewi, H. Lely, E. Taty, Sukirno, *Radiat. Phys. Chem.* **55**, 153 (1999).

Proceedings of the Zakopane School of Physics 2023 International Symposium, Zakopane, Poland, May 23–27, 2023

Controlling the Magnetic Properties of Fe-Based Composite Nanoparticles

O. Polit, M.S. Shakeri, Z. Swiatkowska-Warkocka*

Institute of Nuclear Physics Polish Academy of Sciences, Radzikowskiego 152, 31-342 Kraków, Poland

Doi: 10.12693/APhysPolA.145.139 *e-mail: zaneta.swiatkowska@ifj.edu.pl

We present Fe_xO_y composite particles prepared by pulsed laser irradiation of α-Fe_2O_3 nanoparticles dispersed in ethyl acetate and irradiated using a laser beam in the ultraviolet range with a wavelength of 355 nm. The sizes of particles and composition were controlled by tuning the laser parameters, such as laser fluence and irradiation time. We showed the evolution of the composition through X-ray diffraction measurements. Reactive bond molecular dynamics simulation results show bond breaking/formation during the synthesizing process. We examined the magnetic properties of the particles and showed that coercivity can be changed by the composition of particles and by increasing or decreasing particle size. The choice of systems built of iron and iron oxides made it possible to introduce the exchange bias effect into a range of magnetic properties of synthesized particles.

topics: composite particles, laser synthesis, molecular dynamics, magnetic properties

1. Introduction

Iron-based particles have unique magnetic, optical, electrical, and catalytic characteristics, making them suitable for a wide range of applications, including environmental remediation, catalysis, sensors, and diagnosis of diseases and therapy [1–3].

The physical properties of various iron oxide (Fe_xO_y) compounds can be extremely different, e.g., magnetite (Fe_3O_4) and magnemite (γ-Fe_2O_3) have been commonly used in biomedicine because their saturation magnetization is the highest [4]. The bandgap of hematite (α-Fe_2O_3) is from 2.0 to 2.2 eV, making it useful in applications that involve visible light absorption [5, 6]. Magnetite has unique electric and magnetic properties because its intrinsic crystal structure allows electrons to be transferred between Fe^{2+} and Fe^{3+} in the octahedral sites [7]. Fe_3O_4, γ-Fe_2O_3, and α-Fe_2O_3, including those in the form of the oxidized zerovalent iron core–shell structure, are widely used in heterogeneous catalysis processes and have been used as attractive alternatives for the treatment of wastewaters and soils contaminated with organic compounds [8–10]. The combination of these elements in one particle can result in a material with new or enhanced properties and broader applications. It is well known that the magnetic properties of iron-oxide particles depend on the particles' size, shape, and composition [11]. As the size reduces, below a certain value, the iron-oxide particles change from ferrimagnet/ferromagnet to superparamagnet [12]. Moreover, not only the chemical phase composition of composite particles, but also structural organization (e.g., random clusters of one phase in the other or core–shell structure) influence the magnetic properties [13].

The ability to control magnetic properties, such as saturation magnetization, remanent magnetization, and coercivity of these hybrids is important not only for the fundamental understanding of magnetism in these important materials, but also for their applications.

In the last decades, laser processing has become an important route for producing nanoparticles. The pulsed laser ablation method (PLA) uses a focused laser beam that can provide high energy density on small areas on target, leading to rapid growth of explosive nanoparticles [14–19]. Using an unfocused laser beam of moderate fluence to irradiate nanoparticles dispersed in a liquid medium results in a slightly different phenomenon. The irradiated material melts and subsequently merges to form submicrometer-sized spherical particles. The latter technique, referred to as pulsed laser irradiation in liquids (PLIL), proved to be a comprehensive and promising method for the synthesis of colloidal submicrometer spheres with outstanding properties [20–31]. So far, it has been shown to be an effective approach for the synthesis and control of a variety of composite particles with various morphology (core–shell, alloy) and compositions, which are not only metals or oxides, but also non-equilibrium bimetallic alloys (AuFe, AuCo, and AuNi). The size, morphology, and composition of obtained particles can be tuned in a controllable

manner by experimental parameters, such as wavelength, laser fluence, irradiation time, solvent, and molar ratio of irradiated materials [20]. This paper complements earlier reports on the irradiation of α-Fe_2O_3 nanoparticles dispersed in ethyl acetate [21] by investigating the effects of irradiation using a laser beam in the ultraviolet range with a wavelength of 355 nm (3rd harmonics). By changing the laser fluence and irradiation time, α-Fe_2O_3 is reduced to Fe_3O_4, FeO, and Fe. We show that by varying the laser parameters (laser fluence and/or irradiation time), we can control the phase composition of obtained particles, and thus, we can control the coercivity of obtained particles.

2. Materials and methods

2.1. Nanoparticles synthesis

Typically, raw nanoparticles of α-Fe_2O_3 (Sigma-Aldrich, average size $<$ 50 nm, 0.5 mM) were dispersed in ethyl acetate (5 ml). The resulting suspension was ultrasound-mixed and transferred to a sealed cell equipped with a quartz window. Then, the mixture was irradiated with an unfocused pulsed laser beam generated by Nd:YAG laser operating in the third harmonic mode at 355 nm wavelength and with a 30 Hz repetition rate. First, with fixed irradiation time (1 h), energy densities were changed in the range of 33–166 mJ/pulse cm^2. Then, with a fixed energy of 166 mJ/pulse cm^2, the time was varied in the 15–180 min range. During irradiation, an ultrasonic stirring was maintained to prevent sedimentation and gravitational settling of the suspension. Samples prepared by irradiation in laser fluence 166 mJ/pulse cm^2 were dried and heated in the air at 600°C for 1 h.

2.2. Characterization

The morphology of the obtained particles was observed by a field emission scanning electron microscope (FE-SEM; Hitachi S4800). The average particle size was determined by measuring the diameters of 200 particles from each SEM image. The crystal structure of particles was determined with an X-ray diffractometer (XRD; Rigaku Ultima IV) using standard θ–2θ geometry. The detection was performed using the Cu K_α (λ = 1.54 Å) radiation at operating current and voltage of 30 mA and 40 kV, respectively. All diffraction patterns were collected with a step size of 0.05° in the 2θ range from 20 to 80°. A highly sensitive superconducting quantum interference device (SQUID; Quantum Design, MPMS) magnetometer was employed to measure the magnetic properties of nanocomposite particles. Hysteresis measurements were recorded for dried samples of nanoparticles in a gelatin capsule. Hysteresis loops were obtained by using a maximum applied field up to 50 kOe at 5 K and 300 K. The exchange bias properties of samples were investigated by measuring field-cooled (FC) hysteresis loops in the temperature range of 5–300 K. In the FC procedure, the sample was cooled down from the initial temperature of 300 K to the measuring temperature T, under an applied field of 50 kOe. Once T was reached, the field was set to 50 kOe, and the measurement of the loop started. FullProf software was used for peak fitting and to evaluate the lattice constants of the material and quantitative phase analysis [32].

2.3. Modeling and simulation procedure

Using the ReaxFF module of the Amsterdam Modeling Suite (AMS) software package [33], molecular dynamics simulations (MD) were conducted using a reactive bond force field (RBFF) with Fe/C/H/O parameters [34]. A three-dimensional system with a parallelogram-shaped simulation box is constructed with periodic boundary conditions in all directions. There were four atomic layers in the Fe_2O_3 slab, each containing 200 iron and 300 oxygen atoms, arranged in a (111) direction. The slab was placed in the center of a 50 Å high box that held 180 solvent molecules (density 0.45 g/mL). The density is kept at less than half of the actual (real) density to avoid any errors in the molecular modeling. The canonical ensemble (NVT) and the Nosé–Hoover thermostat are used for MD simulation, with a damping constant of 100 fs. Prior to the RBFF simulations, the initial geometric configuration was optimized through energy minimization using the conjugate gradient algorithm. Then, the system was NVT-equilibrated at 298 K for 5 ps. Once the system has reached equilibrium, an RBFF-MD simulation is performed on it. In order to overcome the computational constraints, high temperatures are commonly employed in RBFF-MD simulations to accelerate reactions [35–37]. ReaxFF MD has been shown to work well for high-temperature simulations with a time step of 0.25 fs [35]. Every 100 frames (25 fs), the dynamic trajectory and binding data are captured. To identify the molecules that form during the simulation, a cut-off value of 0.3 is selected for the bond order in the species analysis. To cover all reactions, including those involving very short-lived species, a low cut-off value is useful. For the simulation box, three simulations were performed, and the average of these simulations was used for additional molecule formation/dissociation analysis. An AMS GPU was used to visualize the results of the simulation.

3. Results and discussion

In Fig. 1b–e, we can clearly see the increase in particle size from 30 to 650 nm with the increase in laser fluence from 66 to 166 mJ/pulse cm^2. On the

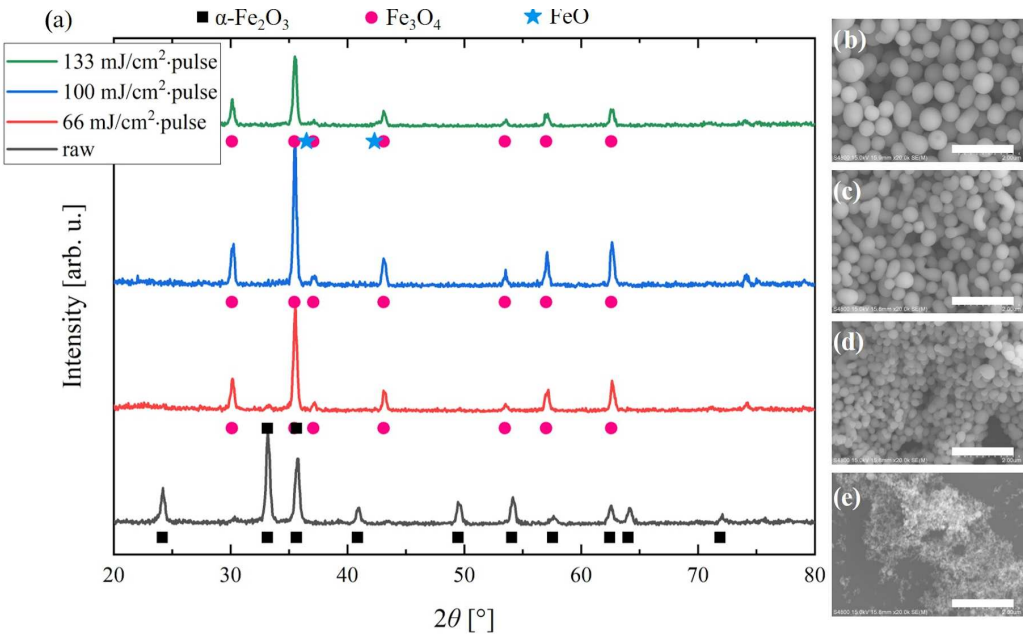

Fig. 1. (a) XRD results and (b–e) SEM images of raw α-Fe_2O_3 nanoparticles and particles obtained by pulsed laser irradiation (355 nm, 1 h) of α-Fe_2O_3 nanoparticles dispersed in ethyl acetate with various laser fluences: (b) 133 mJ/cm^{2}pulse, (c) 100 mJ/cm^{2}pulse, and (d) 66 mJ/cm^{2}pulse; (e) raw Fe2O3 nanoparticles. Scale bar on SEM images is 2 μm.

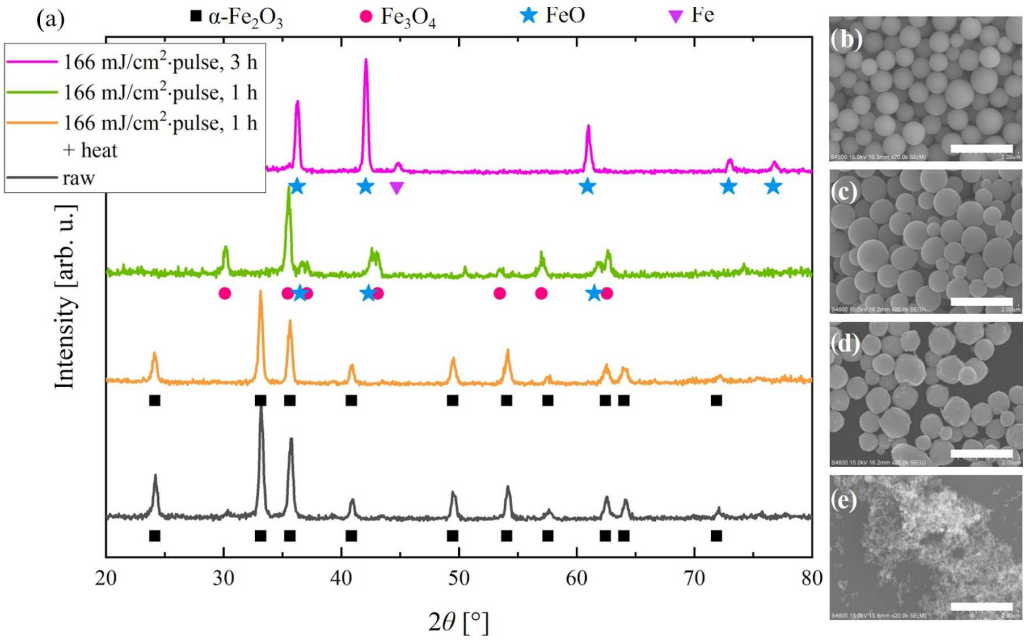

Fig. 2. (a) XRD results and (b–e) SEM images of raw α-Fe_2O_3 nanoparticles and particles obtained by pulsed laser irradiation (355 nm) of α-Fe_2O_3 nanoparticles dispersed in ethyl acetate with various irradiation times: (c) 1 h and (b) 3 h and, (d) after additional temperature treatment (600°C for 1 h) of particles from (c); (e) raw Fe_2O_3 nanoparticles. Scale bar on SEM images is 2 μm.

other hand, extending the exposure time to 3 h with a fixed energy fluence of 166 mJ/pulse cm^2 does not result in an increase in particle size (Fig. 2b–c). The structural transformation of hematite α-Fe_2O_3 to magnetite Fe_3O_4, wustite FeO, and iron Fe as a function of the laser irradiation parameters (fluence, time) has been observed by the XRD method (Figs. 1a, 2a). The raw nanoparticle diffractogram exhibits the diffraction peaks that correspond to crystal planes of hexagonal α-Fe_2O_3 (JCPDS card No. 80-2377) (R-3c). After irradiation with 66 mJ/pulse cm^2, the main phase of

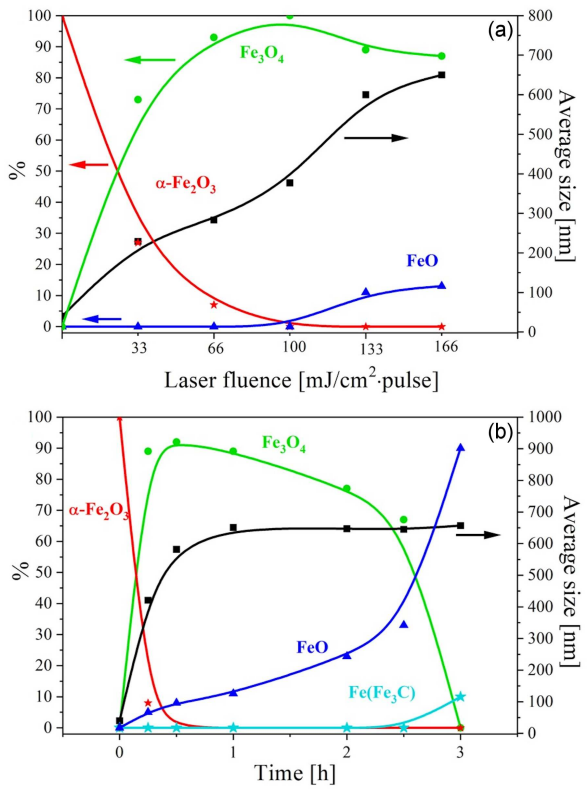

Fig. 3. (a) Dependence of particle size and phase changes on the laser fluence (1 h of irradiation). (b) Dependence of particle size and phase changes on irradiation time (166 mJ/pulse cm^2 fluence).

obtained particles is cubic Fe_3O_4 (JCPDS card No. 88-0315) (Fm-3m), but the diffraction peaks of α-Fe_2O_3 (33.2°, 35.6°) are also observed. The weight ratio of α-Fe_2O_3/Fe_3O_4, calculated from XRD data, is 7:93. As shown in Fig. 1a, the diffraction of particles irradiated with 100 mJ/pulse cm^2 peaks are indexed to the spinel structure, known for the Fe_3O_4 crystal, and no other peaks are detected, indicating that the product is pure phase Fe_3O_4.

A further increase in the laser fluence to 133 mJ/pulse cm^2 (Fig. 1a) and 166 mJ/pulse cm^2 (Fig. 2a) led to a complete reduction of hematite manifested by the disappearance of corresponding peaks, while the peaks of Fe_3O_4 at positions of 37.18°, 43.19°, and 62.56° are asymmetric. The careful analysis of the peak profiles indicated the presence of cubic FeO (JCPDS card No. 46–1312) (space group Fm-3m) phase. The amount of FeO phase in Fe_3O_4/FeO composites is 11% and 13% for 133 mJ/pulse cm^2 and 166 mJ/pulse cm^2, respectively. An increase in the irradiation time to 3 h results in a complete reduction of Fe_3O_4 to FeO and Fe (JCPDS card No. 85-1410), with a FeO/Fe weight ratio of 90:10. The XRD result shows that an hour of heating in air at a temperature of 600°C leads to complete oxidation of particles to α-Fe_2O_3 phase. As can be seen in Fig. 3, the size of particles increases gradually with an increase in laser fluence. For low laser fluence (up to 66 mJ/pulse cm^2), partial reduction of hematite to magnetite occurs. A further increase in laser fluence (100 mJ/pulse cm^2) leads to the complete reduction of hematite and the formation of magnetite. Then (for fluence 133 and 166 mJ/pulse cm^2), the transformation of magnetite into wustite is observed. To gain insight into the changes in the composition of nanoparticles during irradiation, we irradiated them with a laser fluence of 166 mJ/pulse cm^2 as a function of irradiation time. Compared to the irradiation of hematite with a wavelength of 532 nm (2nd harmonics) [21], higher energy was needed to obtain particles of similar sizes and composition, i.e., 180 mJ gave magnetite particles with a size of 600 nm, while in the case of the 3rd harmonic, 100 mJ was sufficient for the complete reduction of hematite to magnetite and obtaining particles with dimensions of 650 nm. Figure 3 shows changes in both particle size and composition for irradiation times ranging from 15 to 180 min. During the first hour, the size increases rapidly and then saturates at a diameter of approximately 600 nm. A similar trend was observed during NiO irradiation (532 nm, 10 Hz, 130 mJ/pulse cm^2) and reported in our previous work [28]. Here, half an hour is sufficient for a complete reduction of hematite, and further extension of the exposure time causes a gradual reduction of magnetite to FeO. Only after three hours does decomposition to Fe occur.

Phase diagrams calculated as the dependence of particle size on the required laser fluence J for Fe_2O_3 systems explain the differences in the results obtained at two different wavelengths. In the case of the 2nd harmonic, as shown in previous work [21], the laser fluence has a minimum value of 200 mJ/pulse cm^2 for particles with a diameter of about 200 nm. The calculations shown in Fig. 4 clearly show that in the case of the 3rd harmonic, the minimum laser fluence is 25 mJ/pulse cm^2. The calculations presented in Fig. 4 clearly show that a laser fluence of 33 mJ/pulse cm^2 is sufficient to decompose hematite particles up to 100 nm in size into magnetite, but not sufficient to melt these particles. It is known that nanoparticles form agglomerates and this fact influences the particle formation process. If agglomerates are larger than 100 nm, the energy needed to decompose hematite and melt the particles has to be higher.

A big role is played here by the interaction between the solvent and the solid phase, started by the absorption of ethyl acetate on the solid surface [22]. Figure 5a, b shows the top and three-dimensional side views of the simulation model. Based on the temperature and energy of the RBMD simulation, the interaction between the solvent and the solid phase is started by the absorption of a solvent molecule at the solid surface. The final products of the process, if the solvent has enough time to fully dissociate, are H_2O and CO_2, as expected. Smaller hydrocarbon species rise to a certain point

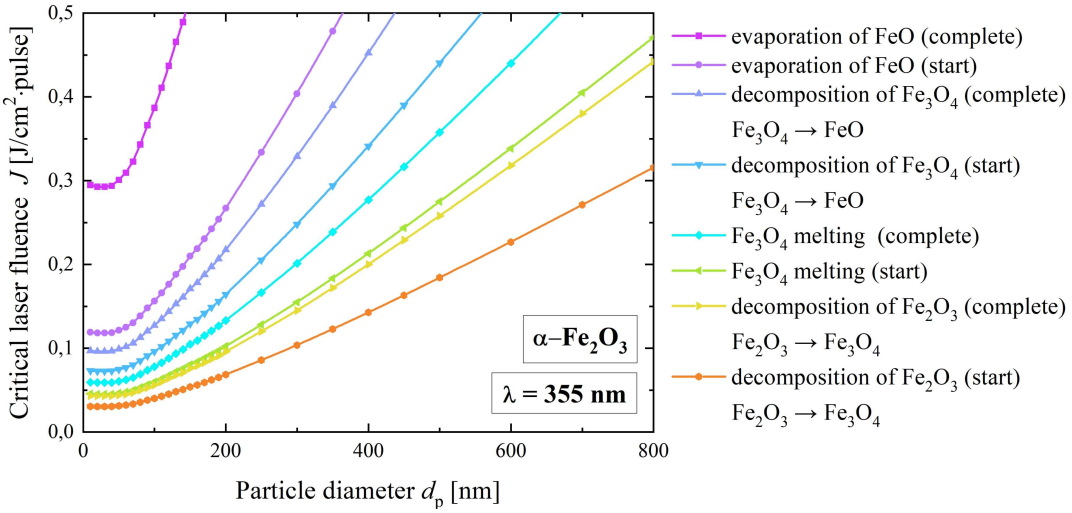

Fig. 4. Phase diagram calculated as particle size dependence of the required laser fluence for Fe_2O_3 systems to heat a particle to the decomposition, melting point, complete melting, boiling point, and complete evaporation using 355 nm laser. Detailed descriptions corresponding to line colors are provided in the chart legend.

in the reaction and then fall as the other species form; this process continues until the final products, i.e., carbon dioxide and water are obtained (Fig. 5d).

The breakdown of solvent is started by the absorption of the separated OH groups on the surface. After the remaining C_2H_5 decomposes to form C_2H_4, smaller hydrocarbons are produced (Fig. 5d). Time-dependent snapshots of the MB1 cross-section show the separation of iron atoms/clusters compounds into the solvent, whereas the solvent-dissociated molecules tend to remain on the slab's surface layers in an attempt to continue the separation process (Fig. 5e, f). The dissociated species diffuse into the Fe-oxide sphere, where the reduction reactions take place.

For magnetic measurements, we chose four samples, two with the same composition (α-Fe_2O_3) but different sizes, 30 and 650 nm (Fig. 6a, b), and two with submicrometer sizes but different compositions, α-Fe_2O_3/Fe_3O_4 and FeO/Fe (Fig. 6c, d). We measured the magnetic hysteresis loop at two temperatures, 5 K and 300 K. The loops at 5 K were measured after cooling the sample in the presence of an external magnetic field of 50 kOe. Figure 6a shows magnetic measurements for raw hematite α-Fe_2O_3 with an average size of around 30 nm. In both temperatures, the hysteresis exhibits a ferromagnetic type of behavior, and a coercive field at 5 K is visibly larger than at 300 K, which is to be expected in this kind of system [38, 39]. Figure 6b shows a hysteresis loop for composite particles obtained through irradiation of α-Fe_2O_3 nanoparticles dispersed in ethyl acetate and irradiated with a laser fluence of 166 mJ/pulse cm^2 for 3 h, after which the sample was heated to 600°C for 1 h. During irradiation, we created submicrometer particles with an average size of around 650 nm, composed of reduced

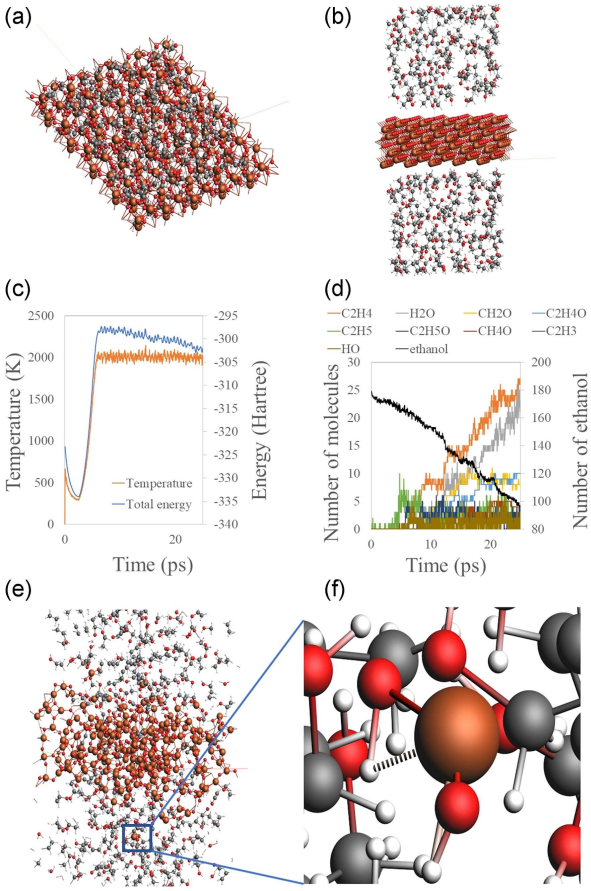

Fig. 5. Molecular dynamics simulations results: (a) front and (b) side views of molecular dynamics model, (c) temperature and energy changes vs time steps of simulation, (d) solvent dissociation and formation of smaller species, (e) snap-shot of simulation box after finishing the calculations, (f) iron atom bonding inside the solvent bath.

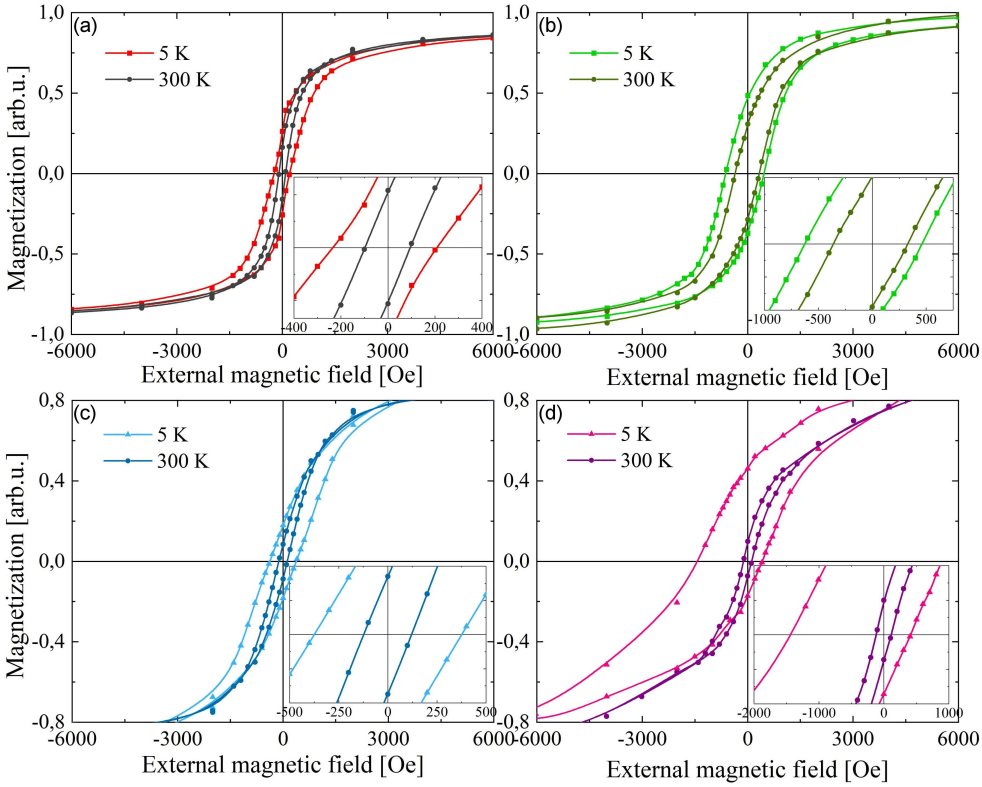

Fig. 6. Magnetic hysteresis loops measured at two temperatures of 5 K and 300 K for systems: (a) raw α-Fe_2O_3, (b) α-Fe_2O_3 irradiated with laser fluence of 166 mJ/pulse cm^2 and heated at 600°C for 1 h, (c) α-Fe_2O_3 irradiated with fluence of 66 mJ/pulse cm^2 for 1 h, (d) α-Fe_2O_3 irradiated with fluence of 166 mJ/pulse cm^2 for 3 h. Every chart contains an inset with a part of the hysteresis loop that was magnified around the center of the coordinate system to make characteristic points of hysteresis more visible.

iron oxides, i.e., FeO and Fe_3O_4. After heating these particles, almost the entire sample oxidized back to hematite, so we obtained the same component as raw material with a changed diameter of particles. The magnetic hysteresis loop for this sample shows the increased value of coercivity both for 5 K and 300 K. At 5 K, the coercive field is 215 Oe and 545 Oe for raw nanoparticles and irradiated particles, respectively. Near room temperature coercivity is also significantly increased, to 100 Oe for nanoparticles and 340 Oe for submicrometer particles. There are many studies in the literature on the magnetic properties of hematite, where significant differences in coercivity values are observed [40–43]. It has been shown that factors such as particle size, shape, morphology, dipolar and exchange interactions, defects, and microstructure of hematite particles have a huge impact on the coercivity value. The coercivity of nanoparticles in 300 K is similar to that reported by other researchers [40, 41]. The increase in coercivity for submicron particles, which can be explained by the assembly of the small and oriented particles into the superstructures, results in the change of the single domain to the multidomain, leading to higher remanent magnetization and coercivity [41, 42]. It has been reported that the crystallographic arrangement of grains and the boundaries between them contribute to high coercivity [43]. High coercivity may also result from magnetoelastic anisotropy caused by internal deformations in small particles and defects in large crystals [40].

Figure 6c shows results for the system obtained through irradiation of α-Fe_2O_3 with a laser fluence of 66 mJ/pulse cm^2 for 1 h, while Fig. 6d shows measurements for particles obtained by irradiation of α-Fe_2O_3 with a fluence of 166 mJ/pulse cm^2 for 3 h. From XRD measurements, we know that the first sample is composed of Fe_3O_4 with a small amount of α-Fe_2O_3, and the second sample is composed of FeO and Fe. At room temperature, coercivity in both cases is almost the same — 110 Oe and 120 Oe for samples with shorter and longer times of irradiation, respectively. However, there are clear differences at low temperatures. The sample composed of α-Fe_2O_3/Fe_3O_4 has a coercive field of 380 Oe, while the sample composed of FeO/Fe has a coercivity of 955 Oe and exhibits a shift of hysteresis loop along an axis of the external magnetic field, which is a characteristic feature of exchange bias effect. Exchange bias is a phenomenon associated with interfacial interactions between ferromagnetic and antiferromagnetic materials. The shift of the center of the hysteresis loop is called the exchange

bias field H_{EX}. In our system, the shift is equal to 475 Oe and is very well visible in Fig. 6d. This specific sample is composed of Fe, which is ferromagnetic at room temperature, and FeO, which is antiferromagnetic below 198 K. In 300 K, FeO is in a paramagnetic state, and we cannot observe the exchange bias effect (Fig. 6d; purple curve) for this system. However, if we cool down the sample to low temperatures in the presence of an external magnetic field, we can observe a shift of the hysteresis loop and enlargement of the coercive field (Fig. 6d; pink curve). This phenomenon is caused by the coupling of magnetic moments between ferromagnet and antiferromagnet below the Néel temperature of FeO [44, 45]. We also observed this effect in other samples containing FeO and ferro-/ferrimagnetic iron oxides, e.g., Fe_3O_4, and the strength of the effect depends on the quantity of antiferromagnetic to ferro-/ferrimagnetic material [25]. Therefore, we can see that by varying parameters of the synthesis of composite particles during irradiation in a liquid process, we can strongly influence the magnetic properties of composites and even introduce additional effects to the system.

4. Conclusions

In conclusion, the pulsed laser irradiation technique has been demonstrated to be a simple method for obtaining submicron iron oxide-based heterostructure particles. We have shown that by changing the laser parameters (laser fluence and exposure time), we can control not only the amount but also the degree of reduction of α-Fe_2O_3 to Fe_3O_4, FeO, and finally to Fe. We have shown that by changing the size and composition of particles, we can change their magnetic properties. We believe that our research will help synthesize materials with specific properties for dedicated applications.

References

[1] L. Mohammed, H.G. Gomaa, D. Ragab, J. Zhu, *Particuology* **30**, 1 (2017).

[2] A.M. Diez-Pascual, *Polymers* **11**, 1790 (2019).

[3] A. Suhasini, K.P.V. Kumar, T. Maiyalagan, *Sci. Eng. Compos. Mater.* **25**, 189 (2018).

[4] I. Fatimah, G. Fadillah, S.P. Yudha, *Arab. J. Chem.* **14**, 103301 (2021).

[5] A. Kay, I. Cesar, M. Gratzel, *J. Am Chem Soc.* **128**, 15714 (2006).

[6] C. Karunakaran, P. Anilkumarl, *J. Mol. Catal. A Chem.* **265**, 153 (2007).

[7] B.Y.Geng, J.Z. Ma, J.H. You, *Cryst. Growth Des.* **8**, 1443 (2008).

[8] M.C. Pereira, L.C.A. Oliveira, E. Murad, *Clay Miner.* **47**, 285 (2012).

[9] S.R.R. Pouran, A.A.A. Raman, W.M.A.W. Daud, *J. Clean. Prod.* **64**, 24 (2014).

[10] Y. Mu, F. Jia, Z. Ai, L. Zhang, *Environ. Sci. Nano* **4**, 27 (2017).

[11] C. Montferrand, L. Hu, I. Milosevic, V. Russier, D. Bonnin, L. Motte, A. Brioude, Y. Lalatonne, *Acta Biomater.* **9**, 6150 (2013).

[12] M. Busquets, A. Espargaró, R. Sabaté, J. Estelrich, *Nanomaterials* **5**, 2231 (2015).

[13] A.G. Kolhatkar, A.C. Jamison, D. Litvinov, R.C. Willson, T.R. Lee, *Int. J. Mol. Sci.* **14**, 15977 (2013).

[14] F. Mafune, J. Kohno, Y. Takeda, T. Kondow, H. Sawabe, *J. Phys. Chem. B* **104**, 9111 (2000).

[15] V. Amendola et al., *Nanoscale* **5**, 5611 (2013).

[16] J. Jakobi et al., *Nanotechnology* **22**, 145601 (2011).

[17] E. Gordon, A. Karabulin, V. Matyushenko, V. Sizov, I. Khodos, *Phys. Chem. Chem. Phys.* **16**, 25229 (2014).

[18] K.D. Malviya, K. Chattopadhyay, *J. Phys. Chem. C* **118**, 13228 (2014).

[19] V. Amendola, S. Scaramuzza, S. Agnoli, S. Polizzi, M. Meneghetti, *Nanoscale* **6**, 1423 (2014).

[20] Y. Ishikawa, T. Tsuji, S. Sakaki, N. Koshizaki, *Prog. Mater. Sci.* **131**, 101004 (2023).

[21] M.S. Shakeri, O. Polit, B. Grabowska-Polanowska, A. Pyatenko, K. Suchanek, M. Dulski, J. Gurgul, Z. Swiatkowska-Warkocka, *Sci. Rep.* **12**, 11950 (2022).

[22] M. Sadegh Shakeri, Z. Swiatkowska-Warkocka, O. Polit et al., *Adv. Funct. Mater* **33**, 2304359 (2023).

[23] H. Wang, L. Jia, L. Li, X.X. Li, Z. Swiatkowska-Warkocka, K. Kawaguchi, A. Pyatenko, N. Koshizaki, *J. Mater. Chem. A* **1**, 692 (2013).

[24] H. Wang, N. Koshizaki, L. Li, L. Jia, K. Kawaguchi, X. Li, A. Pyatenko, Z. Swiatkowska-Warkocka, Y. Bando, D. Golberg, *Adv. Mater.* **23**, 1865 (2011).

[25] Z. Swiatkowska-Warkocka, K. Kawaguchi, H.Q. Wang, Y. Katou, N. Koshizaki, *Nanoscale Res. Lett.* **6**, 226 (2011).

[26] H.Q. Wang, A. Pyatenko, K. Kawaguchi, X.Y. Li, Z. Swiatkowska-Warkocka, N. Koshizaki, *Angew. Chem., Int. Ed* **49**, 6361 (2010).

[27] H. Wang, K. Kawaguchi, A. Pyatenko, X. Li, Z. Swiatkowska-Warkocka, Y. Katou, N. Koshizaki, *Chem. Eur. J.* **18**, 163 (2012).

[28] Z. Swiatkowska-Warkocka, A. Pyatenko, Y. Shimizu, M. Perzanowski, A. Zarzycki, B.R. Jany, M. Marszalek, *Nanomaterials* **8**, 790 (2018).

[29] Z. Swiatkowska-Warkocka, A. Pyatenko, F. Krok, B.R. Jany, M. Marszalek, *Sci. Rep.* **5**, 09849 (2015).

[30] Z. Swiatkowska-Warkocka, A. Pyatenko, K. Koga, K. Kawaguchi, H. Wang, N. Koshizaki, *J. Phys. Chem. C* **121**, 8177 (2017).

[31] H. Fuse, N. Koshizaki, Y. Ishikawa, Z. Swiatkowska-Warkocka, *Nanomaterials* **9**, 198 (2019).

[32] Fullprof Software (accessed on 5 October 2023).

[33] R. Rüger, M. Franchini, T. Trnka, A. Yakovlev, E. van Lenthe, P. Philipsen, T. van Vuren, B. Klumpers, T. Soini, AMS 2022.1, SCM, Theoretical Chemistry, Vrije Universiteit, Amsterdam, The Netherlands.

[34] Ch. Zou, A. Van Duin, *JOM* **64**, 1426 (2012).

[35] K. Chenoweth, A.C.T. Van Duin, W.A. Goddard, *J. Phys. Chem. A* **112**, 1040 (2008).

[36] M. Feng, X.Z. Jiang, K.H. Luo, *Proc. Combust. Inst.* **37**, 5473 (2019).

[37] Q. Mao, A.C.T. Van Duin, K.H. Luo, *Carbon* **121**, 380 (2017).

[38] Ö. Özdemir , *Geophys. J. Int.* **141**, 351 (2000).

[39] I. Lyubutin, S. Lin, Y.V. Korzhetskiy, T.V. Dmitrieva, R.K. Chiang, *J. Appl. Phys.* **106**, 034311 (2009).

[40] M. Tadic, D. Trpkov, L. Kopanja, S. Vojnovic, M. Panjan, *J. Alloys Compd.* **792**, 599 (2019).

[41] J. Lian, X. Duan, J. Ma, P. Peng, T. Kim, W. Zheng, *ACS Nano* **3**, 3749 (2009).

[42] J. Ma, J. Lian, X. Duan, X. Liu, W. Zheng, *J. Phys. Chem. C* **114**, 10671 (2010).

[43] A.R. Goldman, E. Asenath-Smith, L.A. Estroff, *APL Mater.* **5**, 104901 (2017).

[44] M. Kiwi, *J. Magn. Magn. Mater.* **234**, 584 (2001).

[45] J. Nogués, I.K. Schuller, *J. Magn. Magn. Mater.* **192**, 203 (1999).

Proceedings of the Zakopane School of Physics 2023 International Symposium, Zakopane, Poland, May 23–27, 2023

Growth of the Nanostructured Titanium Oxide by Anodization of Ti/Cu/Ti System

J.C. Chojenka* and A. Zarzycki

Institute of Nuclear Physics, Polish Academy of Sciences, Radzikowskiego 152, 31-342, Krakow, Poland

Doi: 10.12693/APhysPolA.145.147 *e-mail: juliusz.chojenka@ifj.edu.pl

The study investigates the impact of the electrolyte composition and anodization conditions on titanium oxide microstructures, analyzing their influence on a trilayer titanium/copper/titanium system. The electrolytes used for anodization had different concentrations of ammonium fluoride and water. The quality and stability of the oxide growth were controlled by monitoring changes in the current density curves during anodization. In water-rich electrolytes, the titanium oxide layer exhibits improved structural quality but reduced layer conductivity, leading to electrical breakdown and destruction of the layer through rapid electrical discharge. Under equilibrium conditions between fluoride ions and water, scanning electron microscope images demonstrate nanoporous structures with inner pore diameters exhibiting a log-normal distribution, with median sizes ranging from 15 to 70 nm across voltage ranges. Linear correlations between the inner pore diameters and the applied voltage are observed, notably in certain electrolytes, indicating stable processes and high quality of the nanopatterned oxide.

topics: anodization, nanoporous titanium oxide, thin films, nanopatterning

1. Introduction

Nanostructured titanium oxide garners significant attention due to its potential applications in biomedical coatings [1], supercapacitors [2], solar cells [3], catalysis [4], templates for magnetic thin films [5], and spintronic devices [6,7]. This attention stems from the large surface-to-volume ratio in titanium oxide, its high surface activity accompanied by high sensitivity, and unique electronic structure.

Among the various methods for fabricating nanostructured metal oxides, one of the simplest and most effective is anodization — an electrochemical process enabling the creation of nanoporous or nanotubular oxides. Aluminum oxide stands as one of the extensively studied materials produced through this method. Anodized aluminum oxide (AAO) has been under study for several decades, leading to the optimization of obtaining highly ordered and tunable nanostructures in terms of diameter. This makes AAO a promising material as templates for the fabrication of functional materials with reduced dimensionality [8–12]. The successful development of an anodization-based process to generate nanotube arrays has extended from aluminum to other metallic or intermetallic materials, such as titanium oxide [13].

The anodization of the titanium may be described as a competition between the formation of oxide and the chemical dissolution of the oxide by fluoride ions [14]. For anodization to occur, the Ti film should be submerged in the conductive electrolyte. In the absence of F^- ions in the media, a thin layer of titanium oxide, called barrier layer, is formed on the surface, according to the equation

$$\mathrm{Ti} + 2\mathrm{H_2O} \rightarrow \mathrm{TiO_2} + 4\mathrm{H^+} + 4e^-. \tag{1}$$

The application of an electric field enhances this reaction by aiding the electrical transport of O^{2-} and Ti^{4+} ions through the growing oxide. However, the oxidation process is limited by the thickness of the oxide layer and slows down with its increase. As the oxide layer thickens, the ionic current decreases due to the formation of the $\mathrm{Ti(OH)}_x\mathrm{O}_y$ hydroxide layer at the oxide/electrolyte interface. This layer is non-soluble and its surface is typically loose and porous, slowly inhibiting the diffusion of O^{2-} and Ti^{4+} ions.

The presence of fluoride ions in the electrolyte alters the oxidation process by complexing with the transported titanium cations at the oxide/electrolyte interface, preventing the precipitation of $\mathrm{Ti(OH)}_x\mathrm{O}_y$, i.e.,

$$\mathrm{Ti^{4+}} + 6\mathrm{F^-} \rightarrow [\mathrm{TiF_6}]^{2-}. \tag{2}$$

Moreover, fluoride can react with titanium oxide and form water-soluble $[\mathrm{TiF_6}]^{2-}$ complexes, leading to the dissolution and breakdown of the barrier layer and an increase in electrical current in the initial stage of anodization. Under the electric field, the titanium oxide growth rate (1) and the dissolution rate (2) can achieve a balance, resulting in the steady growth of a porous or tubular titanium

TABLE I

Anodization parameters for different sample series.

Series	Concentration of NH_4F [wt%]	Concentration of H_2O [wt%]	Andoization voltage [V]
A	0.3	1.5	10,20,30,40,50
B	0.4	5	10,20,30,40,50
C	0.5	10	10,20,30,40,50

oxide layer. Eventually, the current can decrease due to various effects, such as reducing the diffusion of fluoride-containing species in and out of the pores/tubes [15].

Although the mechanism of titanium oxide growth during anodization is well-documented, the majority of research has been centered around work with titanium foil, which limits its application potential. The presence of a thick titanium foil underneath the oxide layer makes such a system unsuitable for use in microdevices. Additionally, the opacity of Ti metal diminishes its applicability for certain optical–electric devices, like dye-sensitized solar cells. Hence, there is a need for studies focusing on exploring methods to fabricate anodic TiO_2 films on alternative functional substrates.

It is of significant importance to investigate the effect of the anodization conditions, because they play a crucial role in determining the microstructure of anodic films and will eventually determine their performances in the devices. In this paper, we will discuss the influence of the electrolyte composition on the microstructure of titanium oxide fabricated through the anodization of a trilayer system consisting of titanium/copper/titanium deposited on a silicon wafer. To the best of the authors' knowledge, there are very few reports about comprehensive research on the influence of the anodization conditions on anodic TiO_2 fabricated from multilayers.

2. Methods

The fabrication process of anodized titanium oxide (ATO) from thin films was divided into multiple stages. Firstly, we cut the silicon (100) wafer into 17 mm length squares, followed by sonication in acetone, isopropanol and distilled water. Then, a bilayer of Ti (50 nm)/Cu (100 nm) was deposited by e-beam evaporation in vacuum of 10^{-5} mbar. Next, we placed a stencil mask at the center of the substrate to deposit 550 nm of Ti film in the shape of a 12 mm circle. This thick layer of titanium was used for the anodization process. The scheme depicting the sample fabrication process is shown in Fig. 1.

The anodization process was conducted in a homemade chamber with a platinum cathode and a titanium film as an anode. The distance between electrodes was set to 30 mm. Anodization was performed in potentiostatic mode using a Delta Electronica SM 300-10D power supply, and the current was measured with an Agilent 34401A multimeter. The electrolytes for anodization consisted of ammonium fluoride, distilled water, and glycol ethylene. The chemical concentration of reagents and the anodization voltage used during the preparation process are listed in Table I. For clarity, we used code names for the samples, distinguishing them by

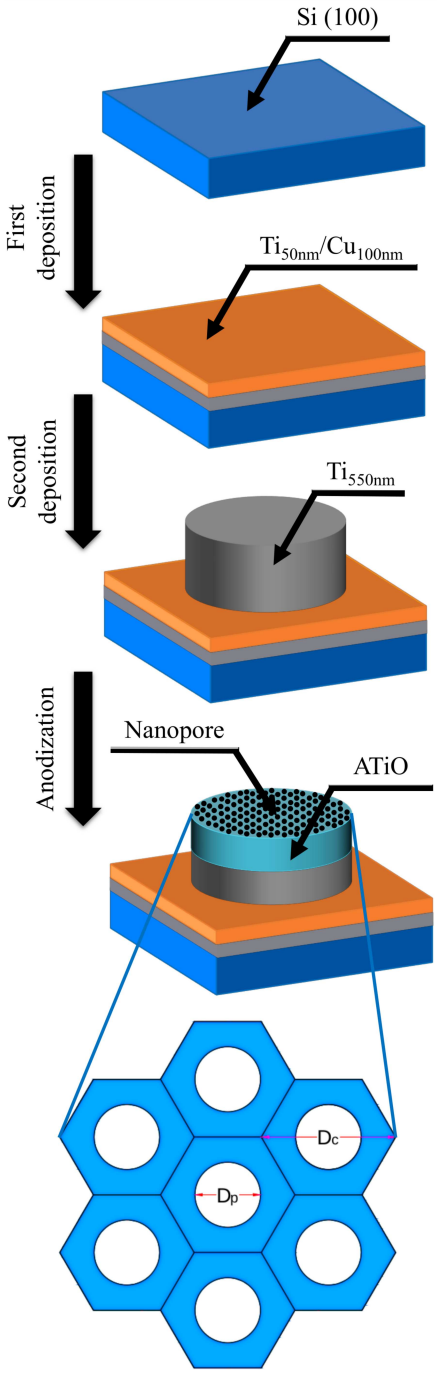

Fig. 1. The scheme of the sample fabrication process. The last picture shows schematic view of the anodized titanium oxide surface. Here, D_p is inner pore diameter and D_c is cell diameter.

series denotation and anodization voltage, for example, A10, A20, etc. Anodization time ranged from 15 to 40 min. The surface morphology was studied by scanning electron microscope (SEM) imaging (Vega Tescan 3), and the chemical composition of the samples was determined through energy-dispersive X-ray spectroscopy (EDS) measurements (Bruker EDS detector).

3. Results

To understand the factors influencing the oxide growth process, we can employ the empirical kinetics equation for the anodization growth rate (r_g), proposed by Cortes et al. [16],

$$r_g \propto AtF^2W^{-1}\exp(\alpha P)\,P + C\big(1-\exp(\beta t)\big)PW^{-1}, \quad (3)$$

where F, W, P, and t represent the fluoride concentration, water concentration, applied electrical potential, and time, respectively, and A, C, α, and β are numerical constants. The growth rate of nanostructured titanium oxide is directly proportional to the square of the fluoride concentration, which results in increased dissolution of the oxide [17], and accounts for the increase in electrolyte conductivity [18]. The presence of water has an inverse effect compared to fluoride, decreasing the growth rate of titanium oxide. This reduction occurs due to the decrease in conductivity caused by a lower density of defects in the synthesized oxide [19].

Progress of anodization is typically monitored by changes in the current density $j(t)$ curves. Figure 2 presents such $j(t)$ dependences for anodized titanium films. Monitoring the change in electrical current density during the anodization process serves as a means of assessing the quality and stability of oxide layer growth. A typical $j(t)$ curve for bulk titanium anodization consists of four parts: (i) barrier layer formation — characterized by a rapid decrease in current density, (ii) initiation of titanium oxide dissolution — marked by a minimum in current density, (iii) random etching of the titanium oxide surface to create nanopores — indicated by an increase in current density, and (iv) an equilibrium phase between the oxide growth and the dissolution, resulting in the stable formation of nanopores/nanotubes — evidenced by a constant current density or a linear decrease over extended anodization time.

During the initial few seconds of anodization, there is a rapid, exponential decrease in current density (Fig. 2), indicating stage (I) of the formation of an oxide barrier layer on the metallic surface of the anodized samples. Subsequently, the current densities for anodization of series A (Fig. 2a) and series B (Fig. 2b) exhibit primarily a linear dependence on the anodization time. This linear trend signifies a stable growth of the nanopatterned oxide layer, where the oxidation and dissolution processes reach equilibrium.

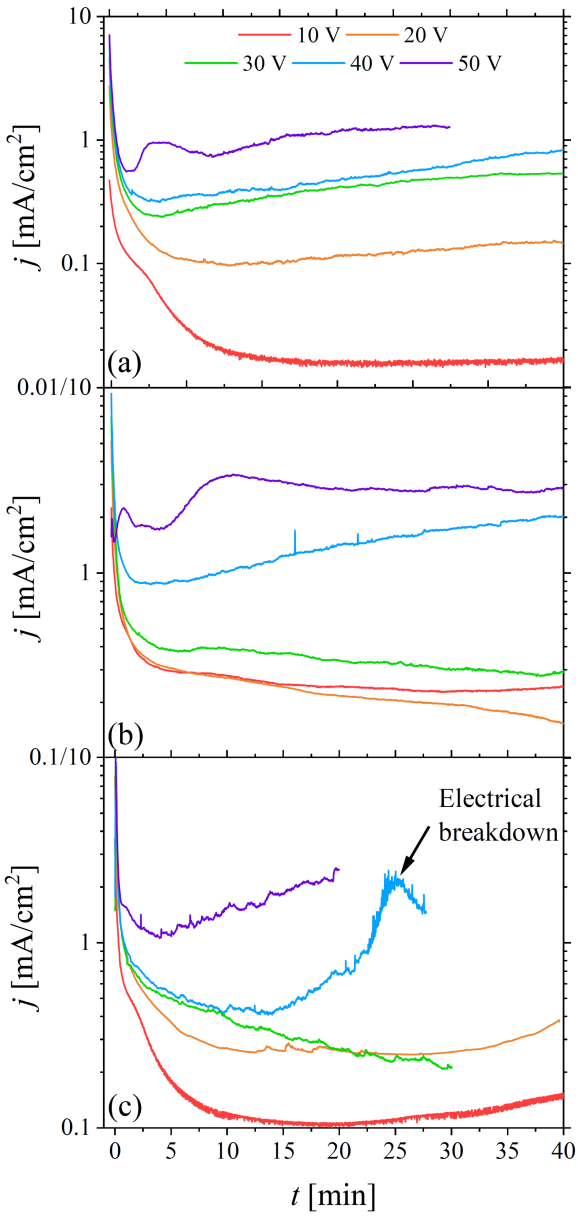

Fig. 2. Current density vs time during anodization process for different electrolytes compositions: (a) 0.3% NH_4F/1.5% H_2O/ethylene glycol, (b) 0.4% NH_4F/5% H_2O/ethylene glycol, (c) 0.5% NH_4F/10% H_2O/ethylene glycol and voltages 10–50 V. The current density is shown in the logarithmic scale.

A different scenario emerges for titanium films anodized in 0.5% NH_4F/10% H_2O/ethylene glycol of series C (Fig. 2c), where only small anodization voltages of 10 V and 20 V result in stable growth of titanium oxide. Higher anodization voltages exhibit irregularities in the current-density curves, indicating an uneven oxidation/dissolution process. This discrepancy becomes particularly evident at an anodization voltage of 40 V, where the rapid increase in current density suggests electrical breakdown throughout the titanium oxide layer.

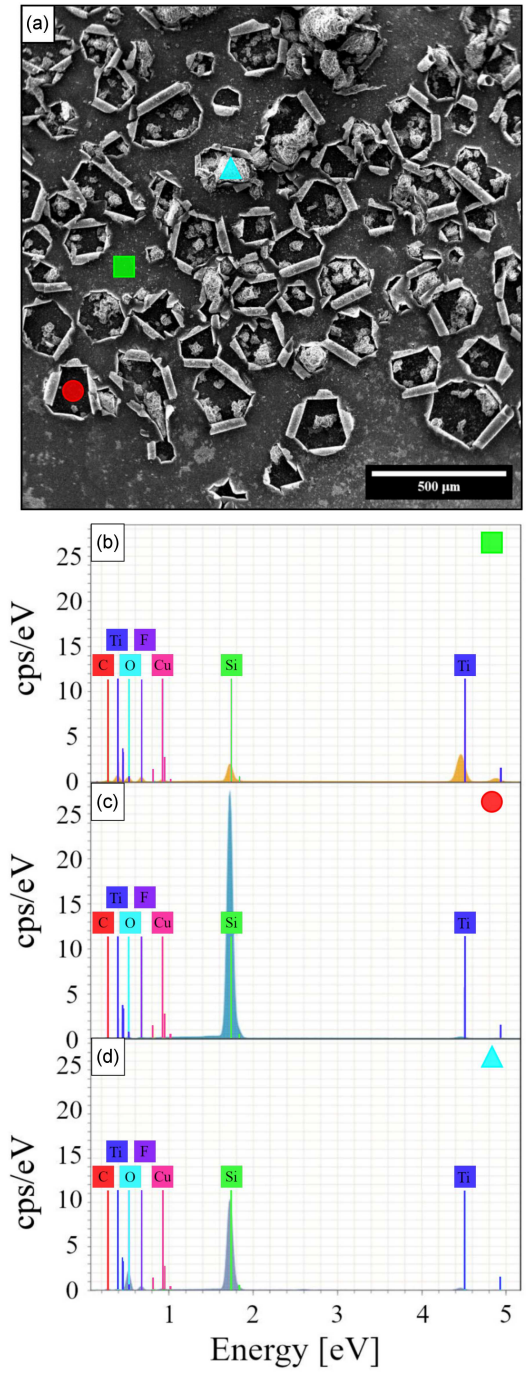

Fig. 3. SEM image of the electrical breakdown (a) for sample C40 and the EDS spectra for the different area on the sample: (b) green square, (c) red circle, (d) cyan triangle.

Electrical breakdown can cause partial exfoliation of the layer, resulting in the crater-like formation due to the electrical discharge from the layer to the substrate. Figure 3a displays the surface of an anodized titanium film (sample C40) after an electrical breakdown. The image reveals three discernible regions: a continuous layer (marked with a green square), a discharge crater (red circle), and irregular granules (cyan triangle).

TABLE II

Concentration of the elements from EDS.

Spot	C [%]	O [%]	F [%]	Si [%]	Ti [%]	Cu[%]
Green square	10.6	29.8	19.9	10.5	28.2	0.9
Red circle	15.0	3.0	0.6	80.4	1.0	0.0
Blue triangle	14.5	40.0	7.5	36.0	1.5	0.4

To assess the elemental composition of these tree regions, we present EDS analysis in Fig. 3b–d. The spectrum corresponding to the continuous layer marked by a green square exhibits the expected elemental composition of anodized titanium oxide, primarily composed of titanium, oxygen, and fluoride (Fig. 3b). The small silicon peak in this spectrum is attributed to the substrate. Conversely, the spectrum of the adjacent red circle region displays a strong silicon peak and a lack of signal from other elements, indicating complete exfoliation of the layer due to electrical breakdown and discharge (Fig. 3c). In the EDS analysis of the last region, marked by a cyan triangle (Fig. 3d), the combination of silicon and oxygen peaks with minor traces of fluoride suggests the formation of SiO_2 and/or SiOF. The quantitative EDS results are compiled in Table II.

Electrical breakdowns occur in samples from the C series, where anodization is conducted using a water-rich electrolyte. This process results in the growth of titanium oxide with a limited number of oxygen vacancies, thereby improving the structural quality of the layer. However, it also reduces the conductivity of the layer, where the titanium oxide layer behaves as a capacitor with opposite electrical charges at the top and bottom parts. An electrical current above a certain threshold potential will rapidly flow through the oxide layer, causing an electrical discharge and ultimately destroying the multilayer film. The exposed silicon substrate is susceptible to oxidation, enabling the formation of SiO_2 or SiOF granules.

The surface images of samples anodized using different electrolytes at an anodization voltage of 30 V, in equilibrium between the oxidation and dissolution processes, are depicted in Fig. 4a–c, along with histograms of the inner pore diameters shown in Fig. 4d–f, respectively. Anodization of our trilayer system in 0.3% NH_4F/1.5% H_2O/ethylene glycol (Fig. 4a) and 0.4% NH_4F/5% H_2O/ethylene glycol (Fig. 4b) results in the formation of a nanoporous structure with the same pores diameter. However, in the case of the sample anodized in 0.5% NH_4F/10% H_2O/ethylene glycol (Fig. 4c), alongside nanopores of a slightly bigger diameter, large granules are also visible, and they are most likely $Ti(OH)_xO_y$. The formation of hydroxyl granules on the titanium oxide surface is facilitated by the high water concentration in the electrolyte, while fluoride ions are insufficient to dissolve them efficiently.

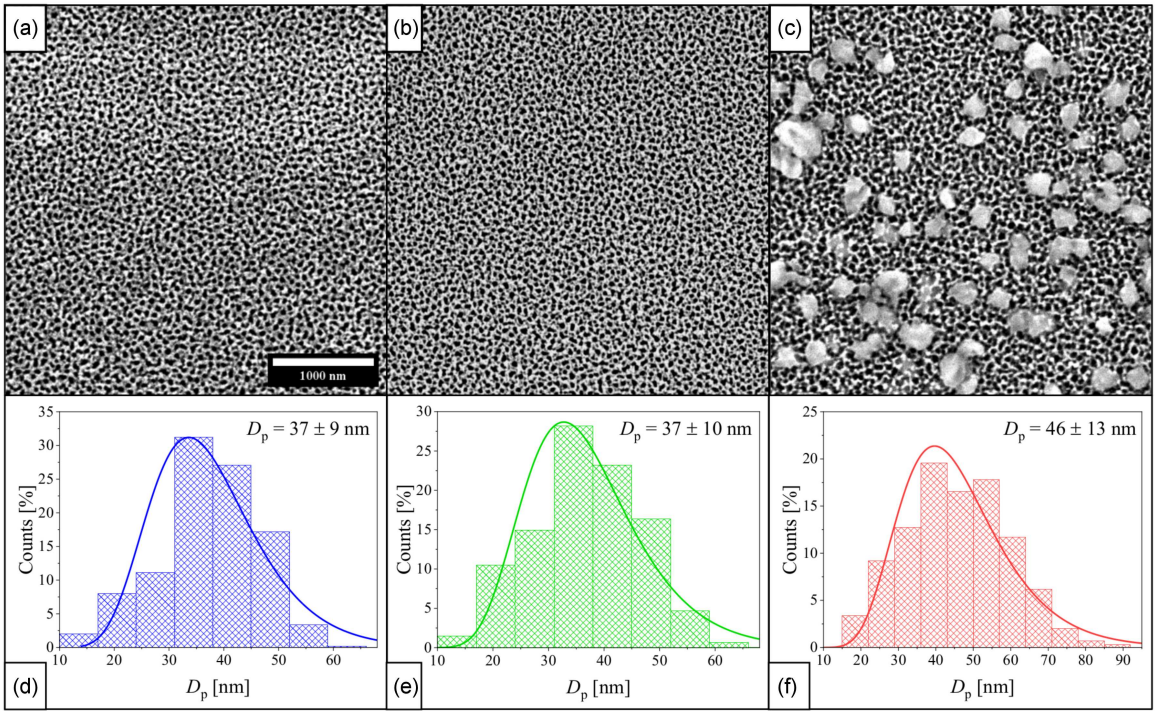

Fig. 4. SEM images for samples A30, B30, and C30 (a–c), together with histograms fitted with log-normal distributions of the inner pore diameter (d–f), respectively.

SEM analysis shows that the nanopores cover the surface homogeneously, but do not display short- or long-range spatial ordering. The arrangement of these nanopores is influenced for thin films by two key factors, i.e., the size of the titanium grains and the anodization time. An increase in anodization time contributes to a better spatial arrangement of nanopores. However, for thin layers, the anodization time must be reduced compared to bulk samples to prevent complete layer exfoliation after full oxidation. Furthermore, the average titanium grain size is smaller in thin film layers compared to bulk samples, which further limits the spatial order. Considering these two factors, the random distribution of nanopores across the titanium oxide is expected.

The histograms representing the inner pore diameters in Fig. 4d–e exhibit a log-normal distribution due to the nature of the measured values, which exclusively fall within positive real values. From our analysis of the inner pore diameters distribution, we determined the median pore diameter to be 37 nm for samples A30 and B30. The median is 46 nm in the case of the sample C30. However, considering the standard deviation, we can conclude that the pores diameter (D_p) remains independent of the electrolyte composition.

The intricate interplay between ion concentration and titanium at the metal/electrolyte interface significantly influences the growth mechanism of titanium oxide, particularly in terms of nanotube length and structural quality. The applied potential stands as the primary factor influencing the inner pore diameters [20]. Figure 5 presents the influence of anodization voltage on these inner pore diameters for the trilayer Ti/Cu/Ti system anodized in various electrolytes.

TABLE III

Fit parameters for the inner pore diameter as a function of anodization voltage.

Series	$y = ax + b$			
	a	Δa	b	Δb
A	0.48	0.29	18.35	10.79
B	1.14	0.14	5.30	3.95
C	0.53	0.21	23.71	6.90

We observed a linear increase in the inner pore diameters with increasing anodization voltage, where the nanopores are consistently present across the entire voltage range from 10 to 50 V. However, in series A (Fig. 5a) and C (Fig. 5c), the lowest voltage does not support the formation of nanopores in titanium oxide due to the imbalance between strong oxidation and insufficient dissolution of the formed oxide. Consequently, this imbalance results in nanopores with diameters of 0 nm being excluded from the fitting. The parameters obtained from the fittings are detailed in Table III.

The parameter 'a' stands for a factor describing the ratio of the increase in nanopore diameter to the voltage escalation. The parameter 'b' estimates the

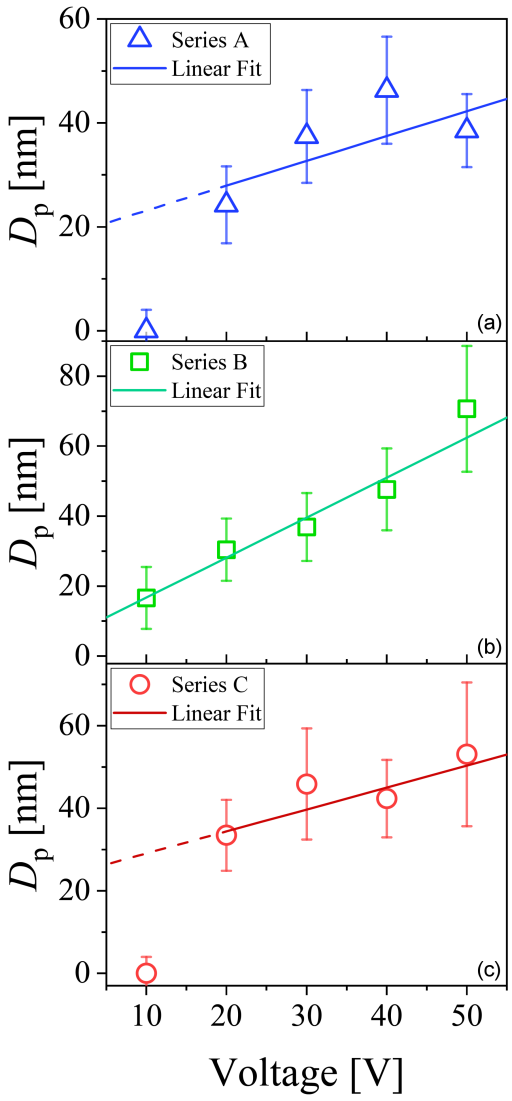

Fig. 5. The inner pore diameters vs anodization voltage for different electrolytes compositions (a) 0.3% NH_4 F/1.5% H_2O/ethylene glycol, (b) 0.4% NH_4F/5% H_2O/ethylene glycol, (c) 0.5% NH_4F/10% H_2O/ethylene glycol.

interpolated nanopores size at zero voltage. However, nanopores start forming above a certain voltage threshold. For series A and C, this threshold exceeds 10 V, whereas for series B, it falls below 10 V.

In Table III we see that the nanopores size increase at a rate of approximately 0.5–1.0 nm per volt. The linear increase in the nanopore diameters may be an indicator of a stable process, and deviations from it suggest an imbalance between oxidation and dissolution parts of the anodization process. This divergence is notably evident in the series C (Fig. 5c), where the nanopores diameters appear relatively constant in relation to voltage. Non-linear characteristics indicate a process that may be challenging to control, resulting in difficulties achieving high-quality samples with the desired nanopattern.

The most consistent linear fit across the entire range from 10 to 50 V is observed in series B (Fig. 5b), suggesting that anodization of the trilayer Ti/Cu/Ti performed in 0.4% NH_4F/5% H_2O/ethylene glycol yields the most predictable results with the highest oxide quality.

4. Conclusions

We examined the influence of the electrolyte composition and the applied voltage on the anodization process of the Ti/Cu/Ti trilayer. Our studies confirm the feasibility of fabricating nanopatterned titanium oxides with adjustable pore sizes from thin film anodization. The porous titanium oxide growth is significantly influenced by the ion concentration, especially from the abundance of water carrying the risk of electrical breakdown. Analysis of SEM images revealed that such breakdown events result in defoliation of the metallic trilayer in certain parts of the sample in the form of craters and the formation of granules of oxidized silicon species through the afterward anodization.

In electrolytes with moderate water ion concentrations, the anodization process yields porous titanium oxide with pore sizes linearly correlated to the applied voltage. The inner pore diameters follow a log-normal distribution, with median values ranging from 15 to 70 nm across voltages ranging from 10 to 50 V, respectively.

Acknowledgments

The support from the NCN grant 2015/19/D/ST3/01843 is gratefully acknowledged.

References

[1] A. Bartkowiak, A. Zarzycki, S. Kac, M. Perzanowski, M. Marszalek, *Materials* **13**, 5290 (2020).

[2] K. Siuzdak, R. Bogdanowicz, M. Sawczak, M. Sobaszek, *Nanoscale* **7**, 551 (2015).

[3] L. Wang, Y. Wang, Y. Yang, X. Wen, H. Xiang, Y. Lia, *RSC Adv.* **5**, 41120 (2015).

[4] J.E. Yoo, M. Altomare, M. Mokhtar, A. Alshehri, S.A. Al-Thabaiti, A. Mazare, P. Schmuki, *Phys. Status Solidi (a)* **213**, 2733 (2016).

[5] J. Chojenka, A. Zarzycki, M. Perzanowski, M. Krupiński, T. Fodor, K. Vad, M. Marszałek,*Materials* **16**, 289 (2023).

[6] A. Zarzycki, J. Chojenka, M. Perzanowski, M. Marszalek, *Materials* **14**, 2390 (2021).

[7] J. Chojenka, A. Zarzycki, M. Perzanowski, T. Fodor, K. Mróz, V. Takáts, K. Vad, M. Krupinski, M. Marszalek, *J. Phys. Chem. C*, **128**, 375 (2024).

[8] A. Maximenko, M. Marszałek, J. Chojenka, J. Fedotova, B.R. Jany, F. Krok, J. Morgiel, A. Zarzycki, Y. Zabila, *J. Magn. Magn. Mater.* **477**, 182 (2019).

[9] T.N. Anh Nguyen, J. Fedotova, J. Kasiuk, V. Bayev, O. Kupreeva, S. Lazarouk, D.H. Manh, D.L. Vu, S. Chung, J. Åkerman, V. Altynov, A. Maximenko, *Appl. Surf. Sci.* **427B**, 649 (2018).

[10] S. Xu, Y. Lei, *ChemPlusChem* **83**, 741 (2018).

[11] Q. Xu, G. Meng, F. Han, *Prog. Mater. Sci.* **95**, 243 (2018).

[12] M. Krupinski, M. Perzanowski, A. Maximenko, Y. Zabila, M. Marszałek, *Nanotechnology* **28**, 194003 (2017).

[13] K. Lee, A. Mazare, P. Schmuki, *Chem. Rev.* **114**, 9385 (2014).

[14] G.K. Mor, O.K. Varghese, M. Paulose, N. Mukherjee, C.A.J. Grimes, *Mater. Res.* **18**, 2588 (2003).

[15] G.K. Mor, O.K. Varghese, M. Paulose, K. Shankar, C.A. Grimes, *Sol. Energy Mater. Sol. Cells* **90**, 2011 (2006).

[16] F.J.Q. Cortes, P.J. Arias-Monje, J. Phillips, H. Zea, *Mater. Design* **96**, 80 (2016).

[17] Z.B. Xie, D.J. Blackwood, *Electrochim. Acta* **56**, 905 (2010).

[18] K. Lee, J. Kim, H. Kim, Y. Lee, Y. Tak, *J. Korean Phys. Soc.* **54**, 1027 (2009).

[19] K.S. Raja, T. Gandhi, M. Misra, *Electrochem. Commun.* **9**, 1069 (2007).

[20] H. Sopha, L. Hromadko, K. Nechvilova, J.M. Macak, *J. Electroanal. Chem.* **759**, 122 (2015).

Subscription terms/Warunki prenumeraty — 2024

Acta Physica Polonica is issued as two separate journals, namely *A* and *B*, in Warszawa and Kraków, respectively. Each of the periodicals is published in the indicated scope and sold by its respective Publisher (see details below). A subscription order should be submitted to the relevant Publisher.

◇ The subscription price of *Acta Physica Polonica A* (*APPA*) is **450 EUR** (surface mail delivery, priority mail on demand with extra **90 EUR** postage rate).

The Publisher of *Acta Physica Polonica A*:

The Director of Institute of Physics
Polish Academy of Sciences
al. Lotników 32/46
02-668 Warsaw, Poland
e-mail: appol@ifpan.edu.pl

bank account BGK S.A. Warszawa:
PL 35 1130 1017 0013 4373 9820 0027
(int. bank code SWIFT: GOSKPLPW)

The archival *APPA* issues (if still available) can be purchased at the Editorial Board of *APPA*.

◇ Cena prenumeraty rocznej *Acta Physica Polonica A* wynosi **2100 PLN** (netto).

Prenumeratę przyjmuje Wydawca:

Dyrektor Instytutu Fizyki
Polskiej Akademii Nauk
al. Lotników 32/46
02-668 Warszawa, Polska
e-mail: appol@ifpan.edu.pl

konto bankowe BGK S.A. Warszawa:
89 1130 1017 0013 4373 9820 0025

◇ The subscription price of *Acta Physica Polonica B* can be obtained by contacting its Publisher:

Institute of Physics
Jagiellonian University
Łojasiewicza 11
30-348 Kraków, Poland
e-mail: acta.phys.pol.b@uj.edu.pl

ACTA PHYSICA POLONICA A
Volume 145 — Number 2

Proceedings of the Zakopane School of Physics 2023 International Symposium
Zakopane, Poland, May 23–27, 2023